Computational and Experimental Study of Flow-Induced Vibration of a Plate/Beam Structure to Improve Performance of Wind Vibration Energy Harvester

A thesis submitted in fulfilment of the requirement for the award of the degree of

DOCTOR OF PHILOSOPHY

IN

MECHANICAL ENGINEERING

Submitted by

ANKIT AGARWAL

Roll No. 901708018

Under the supervision of

Dr. ASHISH PUROHIT

Assistant Professor, MED

Department of Mechanical Engineering

Thapar Institute of Engineering & Technology, Patiala-147004, India

(Deemed to be University)

July, 2023

In the memory of dear elder sister

Anshika Di….

CONTENTS

CERTIFICATE

I, Ankit Agarwal, Roll No. 901708018, hereby declared that the work being presented in this thesis entitled "**Computational and Experimental Study of Flow-Induced Vibration of a Plate/Beam Structure to Improve Performance of Wind Vibration Energy Harvester**" submitted to the Department of Mechanical Engineering at Thapar Institute of Engineering and Technology, Patiala, India, is an authenticated record of my research work for the award of the degree "Doctor of Philosophy" under the supervision of Dr. Ashish Purohit, Assistant Professor, Mechanical Engineering Department, TIET, Patiala, India. This report has not been submitted to any other institute for the award of any other degree.

Ankit Agarwal

Place: Patiala

Ankit Agarwal

Dated: 09/08/2023

Roll No. 901708018

This is to certify that the above declaration made by the student is correct to the best of my knowledge.

Verified By:

Ashish

Dr. Ashish Purohit
(Supervisor)
Assistant Professor
Department of Mechanical Engineering
Thapar Institute of Engineering and Technology
Patiala-147001, Punjab, India

ACKNOWLEDGMENT

I dedicate my Ph.D. thesis work at the Thapar Institute of Engineering and Technology Patiala, Punjab, India, to my beloved parents. The undertaking of this Ph.D. has been a truly life-changing experience for me, and I would not have been able to complete it without the assistance and guidance of many people.

First and foremost, I wish to express my sincere a deep sense of gratitude to **Dr. Ashish Purohit**, my supervisor, for his constant support and guidance at all stages of my Ph.D. The work would not have been possible without his valuable input, advice, and support. I am thankful for his positive suggestions and meticulous guidance that helped me to improve my talent for writing scientific research papers and carrying out new research. His patience and motivation encourage me to achieve my goal.

I am grateful to my Ph.D. committee, which includes **Dr. Tarun Kumar Bera** (Chairman, Board of Studies), **Dr. Neeraj Grover**, **Dr. Rajendra Kumar**, TIET, Mechanical Engineering Department, and **Dr. Prem Pal Bansal**, Professor and Head, Civil Engineering Department, for keeping track of my progress and giving helpful suggestion to improve the work. I am also thankful to **Dr. Tarun Nanda** and **Dr. Gagandeep Bhardwaj**, our Ph.D. coordinators for their approachability and keeping me informed with all the relevant communication throughout E-mails. I also extend my thanks to the entire staff (Teaching/Non-teaching) of the Mechanical Engineering Department for their constant support and cooperation.

I am gratefully admitting the financial support provided by the DST-SERB, New Delhi, India (Project No. ECR/2017/001369). I am thankful to my elder brother Anshu Agarwal and elder sisters Anshika Agarwal and Laxmi Goyal for their love and great support for me. I am grateful to my friends Jaskaran, Param, Rupali, Prakhar, and Ashutosh, who have always motivated me. Finally, my sincere gratitude goes to my parents, **Sri Mahendra Agarwal** and **Smt**. **Geeta Agarwal**. They dedicated their time, efforts, and resources to training me physically, mentally, and intellectually to become a person of importance and value to society which enabled me to complete this work.

Aside from the individuals mentioned above, I would like to thank "**Almighty God**," who has granted me countless blessings, knowledge, and opportunity to pursue and complete this research so that I have been finally able to accomplish the thesis.

Ankit Agarwal

Abstract

Wireless microelectromechanical systems (MEMS) are widely used in engineering applications and provide a solution to gather data from remote locations that are not easily accessible. However, traditional power sources like batteries or cables are not always suitable for powering these systems. As a result, the demand of small-scale self-powering systems has increased extensively. Various non-traditional sources of energy have been explored to satisfy the need and researchers have found that the wind-induced flutter in plane structures has great potential to utilize for small scale power generation. However, such developments are still in the laboratory testing stage, as the flutter is a high-velocity phenomenon, compare to that exists at the normal ambient conditions. Despite this, wind-induced flutter has the potential to provide an abundant source of energy for MEMS systems, and further research is warrented to develop and optimize this technology for practical applications.

This study explores the unrevealed behavior of flutter of a flag-like structure under the influence of an additional wake field generated by an upstream obstruction. The objective of this research is to enhance the performance of a flutter-based energy harvester under practical ambient flow conditions. A comprehensive experimental investigation is conducted in a wind tunnel setting, and selected numerical simulations are utilized to comprehend the involved flow dynamics. A basic model of a flexible plane structure is considered for the study and its response against the flow under different flow regimes is investigated.

Two dimensional numerical simulations including two-way coupling of fluid and structure at low Reynolds number environment are carried out. The primary purpose of the simulations is to understand the effect of additional wake on the modal vibration of a cantilevered structure. The vibration modes are further used to estimate corresponding energy harnessing by correlating induced strain with the piezoelectric transduction mechanism. Additional wake is

introduced using four different geometries placed upstream: a square, an equilateral triangle, a cylinder, and a D-shape. The results indicate that, for a given flow velocity, different shapes induce different bending mode shapes in the structure. A comparison of energy harnessing with respect to different geometries highlights that the D-shape object yields a higher performance.

Several wind tunnel experiments are performed on a laminated plane sheet test geometry under different flow conditions. First, a benchmark study of the flutter of the plane sheet is performed, followed by an investigation of the role of an additional wake from an upstream body. A high-speed camera is used to visualize the mode shape of the structure through sequential image processing. The output is analyzed by a frequency spectrum calculated from the time history of the recorded vibration signal. It is found that the critical velocity significantly decreased due to the flow field generated by the upstream bluff body, ranging from 48% to 59%. Regarding different shapes of the body, the D-shape geometry caused the highest reduction in the critical velocity, at 58.19% compared to the benchmark study. To harvest energy, piezoelectric material (MFC) was used, and an output ranging from 0.20 mW to 0.23 mW was observed across an optimum load resistance in different cases. In terms of a nondimensional ratio (ε) of output to input power, a notable increase up to 14 times compared to the benchmark case is recorded from both the aspects of influence on the critical velocity of flutter and energy harnessing under additional wake flow field. The experimental study qualitatively confirmed the conjecture made through the numerical study. The work proposes a proof of concept applicable to all kinds of structures that undergo plane flutter and is beneficial to improve energy harvesting efficiency irrespective of the mode of transduction.

LIST OF FIGURES

LIST OF TABLES

LIST OF ABBREVIATIONS

CFD	Computational Fluid Dynamics
COV	Coefficient of Variance
DOF	Degree of Freedom
EIE	Extraneous Induced Excitation
FEA	Finite Element Analysis
FFT	Fast Fourier Transformation
FIV	Flow-Induced Vibration
FSI	Fluid Structure Interaction
IIE	Instability Induced Excitation
LCO	Limit Cycle Oscillation
MEMS	Micro-Electromechanically Systems
MFC	Micro Fibre Composite
MIE	Movement Induced Excitation
PVDF	Poly-Vinylidene Fluoride
PZT	Lead Zirconate Titanate
RANS	Reynolds Average Navier-Stoke
Re	Reynolds Number
St	Strouhal Number
VIV	Vortex-Induced Vibration

NOMENCLATURE

A_{swept}	Swept Area
D_t	Tip deflection
E	Elastic Modulus
ε	Output to input power ratio
h	Height of the flexible plate
L	Length of the flexible plate
μ	Mean
R_L	Load resistance
ρ	Density of air
σ	Standard deviation
t_p	Thickness of the flexible plate
V	Flow velocity
V_{pp}	Peak to peak voltage
V_{rms}	Root mean square voltage

CHAPTER 1

INTRODUCTION

With continuous advancement in the fields of micro-electronic sensing and wireless networking, the use of wireless sensors for different engineering applications have gained increasing interest. The micro sensor consumes very low power, up to a few milliwatts (mW), and is apt for many industrial applications like structural health monitoring, wind flow measuring, vibration sensing, etc. In addition, the wireless sensing has also become an attractive solution of problems of data collection at stations of low accessibility, e.g., sensing wind at the peak of sky high towers, at the top of wire bridges, at offshore structures etc. However, powering the remotely located sensors using conventional batteries is a tedious job and also leads to high maintenance cost. Hence, to circumvent this inconvenience, continuous efforts have been made to develop a small scale power source to develop self-powered sensors. Particularly, in the last few years, it has been identified that flow-induced vibration in small structures has potential to be employed as small scale energy harvester and also sufficient to power miniature sensing devices. Although, a majority of relevant projects of energy harvesting by flow-induced vibration are still at development stage and need further investigations.

1.1 Flow-induced vibration as a source of energy

Flexible structures in flow medium experience unsteady forces and show oscillating motion. It is commonly observed in a number of natural and industrial phenomena. The character of vibration depends on a number of parameters like structural geometry, nature of incoming flow, orientation of structural member. In general, based on the governing excitation mechanism, the

flow-induced vibration is classified into three categories as extraneous induced excitation (EIE), movement induced excitation (MIE), and instability induced excitation (IIE) [1].

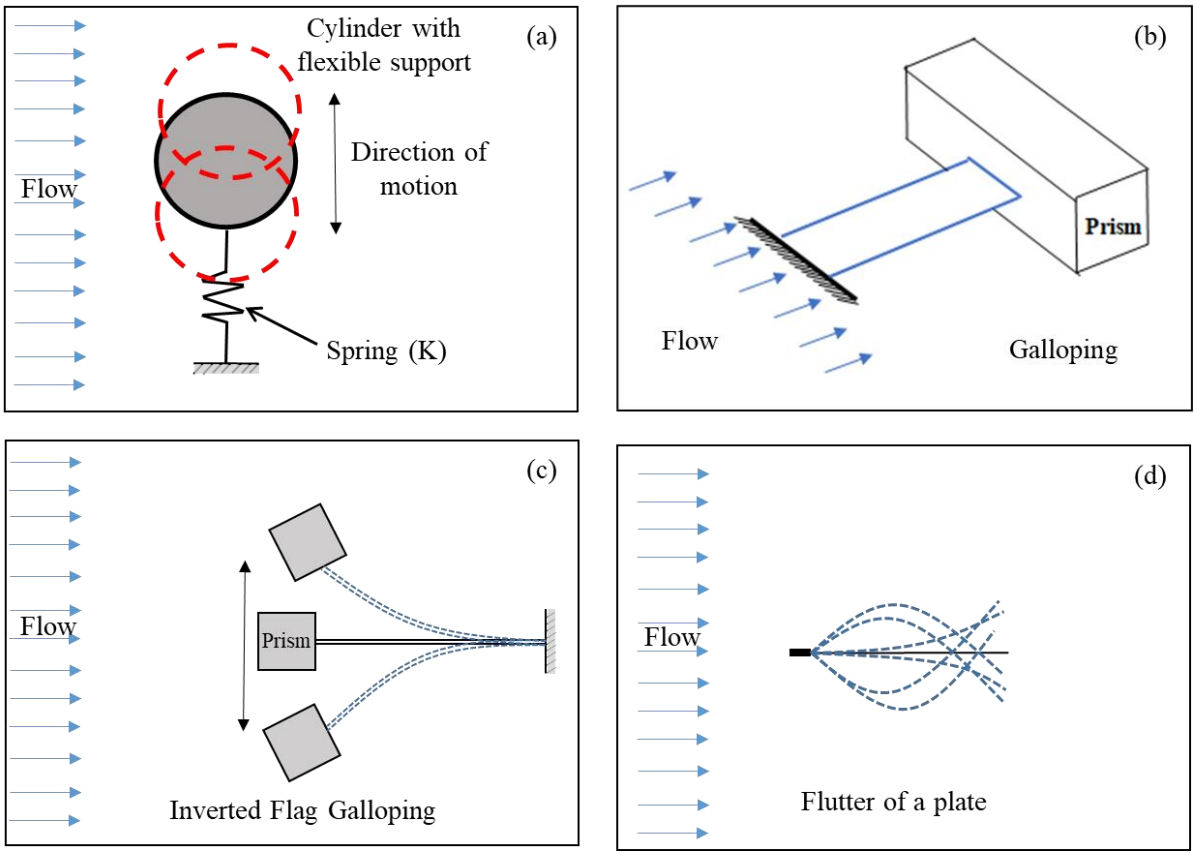

Figure 1.1: Schematic diagram of (a) VIV: cylinder with flexible support in the flow, (b) Galloping: square prism connected at the end of cantilever support, (c) Galloping: inverted flag in flow, (d) Flutter: plate oscillating in higher bending mode in flow

1.1.1 Vortex-induced vibration (VIV)

VIV is a phenomenon that occurs when an object or structure is placed in a fluid flow, such as water or air, and experiences an oscillating motion due to the shedding of vortices in the wake of the object. When a fluid flows past an object, it creates vortices in its wake. The shedding of these vortices can cause the object to vibrate or oscillate, depending on the frequency and magnitude of the vortex shedding. In the case of VIV, the oscillations are self-excited, meaning that they are not caused by external forces but rather by the interaction of the fluid flow and the structure itself. Figure 1.1 (a) shows

typical schematic representation of VIV of a cylinder in flow. When the vortex shedding frequency becomes close to the natural frequency of the flexible structure, large amplitude vibration takes place. In general, VIV is common in many engineering applications, viz. long transmission cable, long riser used in offshore industries, long pillars, chimneys, suspension bridges, automobiles, aircrafts, etc., and considered dangerous for the health of structure. However, it is also utilized to harvest vibration energy using different mechanisms [2]. Apart from a solid body with flexible support, a plane flexible sheet in the wake of an upstream body is another mechanism that exhibits vortex driven vibration. Incoming vortex disturbance imposes unsteady forces on the structure and induces synchronized vibration. It is also called as wake galloping rather than vortex-induced vibration and is defined under EIE. One benefit of vortex-induced vibration (VIV) is its ability to harness energy from fluid flows, including wind or water, without relying on rotating components. However, VIV devices often exhibit a low power output efficiency and are prone to fatigue and damage caused by variations in fluid flow, such as changes in wind or water velocity and direction.

1.1.2 Transverse galloping

Another flow mechanism that is perhaps more extensively investigated from the flow energy harvesting aspect is transverse galloping. Typically, galloping noted in geometries consists of an asymmetric cross-section or attached with an aft structure (Fig 1.1b). The physics involved shows that when the flow passes over an asymmetric section, the flow gets separated and forms circulation bubble (CB), which creates alternating low and high pressure distribution on the structure and leads to an unsteady lift force. In general, galloping is performed using an assembly of cantilever support with considering a tip body. An inverted flag type orientation (Figure 1.1c) also shows galloping in the flow medium. Galloping devices offer the advantage of being relatively uncomplicated and inexpensive

to produce, rendering them a viable solution for specific use cases. Moreover, they are capable of harnessing power across a broad spectrum of wind speeds and frequencies. However, it is important to note that these devices have the potential to induce undesirable vibrations or inflict structural damage upon the host system to which they are affixed.

1.1.3 Flutter

Flutter is a movement induced aeroelastic (MIE) instability whose origin lies in a trade-off between structural and aerodynamic forces. The aerodynamic excitation pumps energy into the structure, which dissipates by the system damping. If the flow energy input becomes larger than the amount dissipated per cycle, vibration amplitude grows and resulting in self-sustainable coupled mode oscillation. It depends on the flow-elastic coupling of attached flow and originates above a threshold flow velocity. Extensive work is reported in literature on prediction of flutter in membranes, flags, papers, etc.; however, a few studies are focused on flutter-based energy harvesters. Flutter devices have the benefit of being suitable for deployment in scenarios involving high flow velocities, coupled mode of vibration, and a wide range of flow velocities and frequencies. However, it is essential to carefully design such devices to prevent damage or failure due to the high forces and speeds involved, as they can be highly intricate and complex in nature.

It can be summarized as follows,

- From the safety of the structures, flow-induced vibration has always been a concerned and researched exhaustively. Majority of researches are dedicated to know either the involved physics or to develop control strategies. Out of several types, the flutter is primarily researched to understand its complex dynamics and post critical behavior.

- Although galloping has been majorly exploited to harvest flow vibration energy than the other mechanisms, and the probable reason for this may be a simple structure that quickly responses in the first bending mode at lower wind velocity.
- Contrary to extensive adaptation for energy harvesting application of galloping, the reason for limited use of VIV based system is probably the narrow operating velocity range (locked in) that hinders its applicability at variable flow conditions.
- In case of flutter-based energy harnessing system, researches are remained only up to laboratory testing where in energy harnessing effect is analyzed in wind tunnel at a sufficiently higher flow velocity [3]. The marginal utilization of flutter in energy harnessing applications may be due to requirement of higher flow velocity than available at normal outdoor conditions.

In the context of conversion of mechanical energy into useful electrical power ~~means~~, piezoelectric transduction has been found to be a commonly adopted transduction. Many active researches are ongoing to develop a piezoelectric energy harvester using wind induced vibration. Piezoelectric harvester works on a simple electro-mechanical conversion principle, wherein the mechanical vibration strains piezoelectric material which in turn generates eclectic charge. The available research indicates that thin layer(s) of piezoelectric material overlaid on flexible sheet provides stable output and can be utilized as power source for wireless sensors.

From the reported research, it has been observed that flutter occurs at significantly higher flow velocity. Nevertheless, it cannot be ignored that the flutter in plane structure is highly coupled mode phenomenon wherein structure vibrates in the combination of first and higher bending modes of a cantilever structures (Figure 1.1 (d)). Moreover, the output along with piezoelectric transduction is a direct consequence of strain induced in the plane structure; the couple mode oscillation (in flutter) has great potential to yield higher electrical energy. Therefore, in order

to truly enhance power extraction from a flutter-based harvester, serious efforts need to be made to extract reasonable power at available ambient flow velocity.

1.2 Motivation of the research work

The present research is inspired by Manela and Howe's [4, 52] study on the forced motion of a flexible flag. From the preliminary theoretical study, Manela and Howe have revealed that the vortex field generated by the flag pole influences the critical velocity of flag flutter. The focus of the present research is to unwrap the effect of incoming wake on the flow-induced instability of plane sheets. Several researches on the flutter have been carried out so far; however, its potential to employ as an energy harnessing mechanism is yet to be systematically explored. Flutter is a high velocity phenomenon, and its energy harnessing application is still under progressive stage. The unique contribution of the present work is a systematic study of flutter in the wake of an upstream object and its impact of energy harnessing performance. However, to the best of our knowledge, no comprehensive investigation is followed afterward. It is interesting to further explore the role of additional wake field on the critical velocity of flutter of a plane structure, and more importantly, as this aspect has not been considered from the point of view of improvement in the performance of flutter energy harvester, a thorough study is warranted to improve the usability of flutter as an energy harnessing mechanism. Moreover, it is learned that flow over a bluff body causes vortex shedding, and if a plane flexible structure is placed in the wake of the body, it exhibits VIV for a give locked in a range of flow velocity. On the other hand, if the same flexible structure is placed in the flow without an upstream bluff body, it shows flutter at a velocity higher than observed during VIV. However, what happens if the flow velocity continuously increases beyond the lock-in range is ambiguous. The knowledge of system response under vortex field at higher flow is a fundamental issue and needs to be clarified systematically. The present work is categorized in a sequential manner, including study of structural mechanism of a fluttering structure and

subsequently study of energy harnessing from the flutter instability. The following concerns are addressed in the present work.

- The role of additional wake on the plane flutter is investigated. For this purpose, flutter of a plane structure is realized in the presence of an upstream bluff body.
- The effect of shape and size of the upstream body on the flutter instability is studied. The vibration is analyzed in terms of amplitude, frequency, and mode shape.
- Initially, numerical simulation is planned to understand overall impact of wake disturbance on the vibration characteristics of a flexible structure. However, the focus is given to the experimental study in wind tunnel environment. In experiments, a reference study of flutter of plane structure is also performed for comparison.
- Energy harnessing under different flow conditions with different geometries is exercised. The piezoelectric transduction is adopted to convert mechanical vibration energy into electric energy.

As the main objective of the present work is to improve the performance of flutter-based energy harvester, the proposed work is an important step that reveals tangible characteristics of flow energy harvesting system and provides fundamental roadmap for commercializing such harvester in future. In addition, it enhances the present understanding of complex dynamics of flutter instability.

1.3 Thesis organization

This thesis consists of six chapters, a brief summary of individual chapters is discussed below.

Chapter 1: Introduction

This chapter discusses need of small scale power sources for powering miniature electromechanical devices planted at remote locations. A brief discussion of theoretical

background of different types of flow-induced vibration (FIV) and their importance in energy harnessing application is given, and hurdles in implementation of flutter-based energy harvesters, present research gap etc., are presented in a systematic manner.

Chapter 2: Literature review

A detailed review of the literature related to FIV and development of energy harnessing devices has been presented in this chapter. Based on different flow-induced excitation mechanisms, the review is mainly divided into three major sections. For clarity, the vibration mechanism itself is explained in the context of energy harnessing work under different conditions. An emphasis is given to the review of flutter instability related research and its implementation for energy harnessing studies performed under different conditions. In the last section, a summary of the review, important literature gaps, and objectives of the present work are presented.

Chapter 3: Numerical study of flow over flexible plate

In this chapter, a numerical investigation of flow-induced vibration of a flexible plate in the wake of different bluff bodies is performed. The work presented targets first three objectives of the research. Computations are carried out on a test assembly of a flexible cantilever 2D structure. Simulations are done in ANSYS multifield solver, and to optimize the computational effort, two-dimensional flow at a low Reynolds number flow condition is considered. Energy harnessing is analyzed based on the strain distribution on the surface of the plane structure.

Chapter 4: Experimental investigation of flutter of a cantilever plate

This chapter focuses on experimental setup design and effect of additional wake on the critical velocity of flutter by introducing bluff body in flow. The main aim of the experiments is a qualitative verification of important findings of the numerical study explained in Chapter

3. Experiments are performed in a low velocity wind tunnel to measure the flutter of a test model of plane sheet at different flow conditions. Moreover, in order to find the role of different shapes of the bluff body on the arrival of flutter, four test sections as square, triangle, cylinder, and D-shape are used.

Chapter 5: Energy harvesting from flow-induced vibration

The effect of additional wake on the critical velocity was discussed in the previous chapter. This chapter focuses on corresponding energy harvesting. The comparison is made by considering the power output as a parameter in both the cases, i.e., flat plate and different shapes of upstream bluff body. For energy harnessing purpose, Micro fiber composite (MFC) has been used.

Chapter 6: Conclusions and future scope of the work

This chapter summarizes the main conclusions of the research work and describes the possible future directions which warrant attention.

CHAPTER 2

LITERATURE REVIEW

Energy generation at mass level from non-traditional sources like solar, wind, tidal etc., has been a field of interest from decades. However, with recent advancements in microelectronics components, demand for small scale energy harvesters has increased extensively. Particularly for remotely located sensors, flow-induced vibration (FIV) has been identified as a potential source to harvest electrical energy, and significant research is undergoing to create a sustainable source. In recent past, different harvesting systems based on different flow excitation mechanisms are developed and tested under different flow conditions. In case of a flag like structure in flow, it behaves differently based on the incoming flow condition and results in both synchronized oscillation as well as unstable vibration. The present research is dedicated to performance analysis of a flutter-based energy harvester under the presence of additional wake field. Since the work carried out involves understanding of flow field and its impact on the flexible structure and subsequently energy harnessing aspects of the flow-induced vibration, a thorough literature review of flow-induced vibration and corresponding research of energy harvester has been conducted. The entire review is mainly divided into three parts, i.e., (1) VIV, (2) Galloping instability, and (3) Flutter instability. For clarity, the vibration mechanism itself is explained in the context of energy harnessing work under different conditions. An emphasis is given to review of flutter instability related research and its implementation for energy harnessing process using piezoelectric transduction mechanism. In the last section, a summary of the review, important literature gaps, and objectives of the present work are presented.

2.1 Vortex-induced vibration

When a bluff body is exposed in a flow field, flow stream gets separated and forms shear layers in the downstream side. The shear layer further extends, forms vortex, and subsequently vortex shedding takes place. The alternate vortex shedding imposes unsteady forces on the bluff body, and if the support is flexible, the body vibrates in a direction perpendicular to the direction of the flow, and phenomenon is known as vortex-induced vibration (VIV). VIV is commonly observed in offshore industries, long transmission cables, suspension bridges, long chimneys, and many other engineering applications. The frequency of vibration during VIV is a direct consequence of vortex shedding frequency and is explained by a non-dimensional Strouhal number ($St= f \times D/U$), where D represents the cylinder diameter, f is vortex shedding frequency in Hz and U is the flow velocity. By choice, the Strouhal number is derived for the case of flow over a rigid stationary cylinder/sphere and helped to understand the synchronization of the natural frequency of flexible assembly with the vortex shedding. When the two frequencies become close, high amplitude oscillations happen, and the region of large vibration is defined as the lock-in zone [5]. Suppression of VIV has always been an important aspect of the safe operation of structures/machineries, so extensive experimental and theoretical studies have been carried out on VIV in the past.

Williamson and Roshko [6] have experimentally explored the vortex shedding pattern of a cylinder with flexible support. They have identified lock-in region by varying the flow velocity. They observed a number of different vortex wake mode regimes and classified them into three groups. For different flow velocities, different types of vortex pairs have been reported. In a similar study, Govardhan and Williamson [7] have numerically studied transverse vortex-induced vibration (VIV) of an elastically mounted rigid body in fluid flow. The vortex wake shedding pattern for a cylinder is directed to move in a sinusoidal trajectory over a wide range of wavelengths and amplitudes. Yamamoto *et al*. [8] have compared the results obtained by

Williamson and Roshko [6] have considered a hydrodynamics interaction of a flexible long cylinder in the flow imitating a marine rise in the ocean current. Extensive numerical and experimental research work has been carried out on VIV and documented in comprehensive review studies [9, 10].

Traditionally, the VIV is defined as a single body placed in the flow, and most of the related work reported in the literature is on the flow over a cylindrical body and corresponding VIV. In order to alter the resultant, drag and lift forces, a splitter plate is conventionally attached at the rear side of the structure. The splitter plate hinders the joining of separated shear layers, avoids formation of vortices in the wake region, and delays the vortex shedding phenomenon, which results in a reduction in the lift force. Shukla *et al.* [11] have performed several tests to understand the dynamics of a pivoted cylindrical body with a rigid splitter plate. Contrary to this, if a flexible structure is placed in the downstream side of a bluff body, the vortex field interacts with the structure and induces vibration, which is termed as wake induced vibration or wake galloping [12]. The orientation of the flexible structure and its position with respect to the upstream bluff body are the key parameters that influence the amplitude and mode of vibrations and have been studied by several researchers.

Wang *et al.* [13] have numerically investigated the vibration of a flexible plate placed at different distance in the downstream wake region of a circular cylinder, and the effect of level of flexibility of the plate on the overall vibration level is analyzed. A low Reynolds number environment is chosen for the study. They found that lower bending stiffness raises higher bending mode vibration in the plate. Turek and Hron [14] have proposed new standards for the challenging valuation of various methods for fluid and structure interaction problems. The model comprises laminar incompressible channel flow around flexible structure which results in vortex-induced oscillation of a hyper elastic 2D plate. Low Reynolds number flow is adopted, and two-way fluid structure is considered in the numerical simulation. To fill a gap of

a benchmark study at higher Reynolds number flow conditions, Nayer *et al.* [15] have presented a case study of fluid-structure interaction in turbulent flow conditions. A similar test model using a rubber splitter plate mounted with a circular cylinder is considered by Turek and Hron [14]. The results obtained are also verified by wind tunnel experiments. A number of similar works are carried out subsequently; however, in most investigation, a low Reynolds number flow condition is considered to reduce the computational efforts [16].

It is observed that in the majority of wake induced vibration investigations, a cylindrical body is used for upstream object; however, the role of different shapes of the frontal object, e.g., square, triangular, and semi-circular section, etc., on the dynamics of the trailing structure is also explored. Lee and You [17] have studied the suppression of vortex shedding from a square body by adding a highly flexible splitter plate at the trailing side. They put effort into establishing a correlation of reduction in the vortex shedding with the flow-induced noise generation. A series of numerical simulations are performed at low Reynolds number conditions, and it is observed that the oscillation frequency is a trade of natural frequency of the structure and the vortex shedding frequency. Hu *et al.* [18] have also considered a similar assembly of squares with a splitter plate and demonstrated lock-in phenomenon in the vibration of trailing plane structure. They employed commercial software ANSYS for simulation, and a low Reynolds number medium is considered. Purohit *et al.* [19] have studied the noise generation from wake-induced vibration of a flexible plate. Low Reynolds number simulations are performed on an assembly of a plate with a square upstream body and concluded that the frequency of flow-induced vibration and surrounding sound field is dominated by the structural natural frequency. It may be interpreted that in the case of a hyper elastic structure, the vortex shedding frequency dominates the vibration, and with a relatively stiffer structure, the structural frequency dominates the coupled FSI phenomenon. Bennett *et al.* [20] have studied dual planner jets to reduce the noise generation from flow-induced vibration. Tandem cylinders

were utilized as the test bodies, and the flow-induced vibration as a noise source, and with the use of CFD models, an ideal location for the cylinders was find out.

The aforementioned literature review illustrates the importance of VIV from the point of view of development of numerical methods, understanding of the flow field, and measures to suppress vibration. Besides this, investigations are carried out to explore the energy harvesting perspective of wake induced vibration. In the benchmark experimental investigation by Allen and Smits [21] charge generation viability of a piezoelectric membrane ("eel") under the vortex flow generated by an upstream bluff body is discussed. Water channel testing is performed, and the lock-in phenomenon is demonstrated by changing both the size of the bluff body and the corresponding gap between the body and piezoelectric membrane. Taylor *et al.* [22] have followed their research, implemented the concept, and proposed an ocean current energy harvesting mechanism. Sivadas and Wickenheiser [23] have numerically calculated energy harvesting from the vibration of a bimorph structure (piezoelectric material bonded at both sides of the plane structure) under the vortex flow from different frontal bluff bodies. Low Reynolds number flow is considered, and the multi-physics software package COMSOL© is used for the numerical study. Three geometries as a cylinder, triangle, and pentagon are used, and a comparison of power generation among different cases has been reported. In the subsequent work, they included a D-shape geometry and concluded a higher power output for the same configuration while compared with previous assemblies [24].

Pan *et al.* [25] have also considered a D-shape object and numerically investigated the vibration behaviour of a flexible plate in flow. They extended the work by exploring the effect of the length of the plane structure on the energy generation performance. Instead of estimating power, they used plane strain induced in the structure to show energy harnessing potential. A series of numerical testing performed by changing the spacing and material property. Akaydin *et al.* [26] have experimentally and computationally investigated flow vibration energy

harvesting via piezoelectric in an inverted flag configuration fixed end of the plate is kept in the downstream direction. The wake turbulence first interacted with the free end of the plate and induced oscillation. Maximum power output is obtained when the natural frequency of the piezoelectric beam matches with vortex shedding frequency. The experiment obtained a maximum power of 4 μW at 7.23 m/s airflow. Similar work is reported in Rashidi *et al.* [27].

It is observed that many of the investigations are reported to show the capability of a particular numerical approach in solving problem of fluid-structure interaction. It should be emphasized that the majority of work on wake induced vibration research is primarily focused on understanding flow dynamics in order to further describe the associated drag and lift forces. In addition, few works are presented on vibration energy harvesting using piezoelectric material or other means.

2.2 Galloping instability

Galloping is usually associated with asymmetric cross sections or an aft structure in geometries. Den Hartog [28] was the first to detect the galloping effect numerically, and he used quasi-steady approximation to determine the criterion for critical velocity of galloping. The physics demonstrates that when a flow passes over an asymmetric portion, the flow separates and forms an inner circulation, resulting in a negative surface pressure distribution and an unsteady lift force, as demonstrated in Figure 2.1. Paidoussis [1] provides a detailed description of the galloping phenomenon, as well as other flow instabilities. In general, transverse galloping of a cantilevered structure with a cylindrical tip mass is the most common system for harvesting energy from flow-induced vibration and has been studied by many researchers. Moreover, other tip geometries, e.g., square, triangular, D-shape etc., are being studied to explore theoverall effect on the power output.

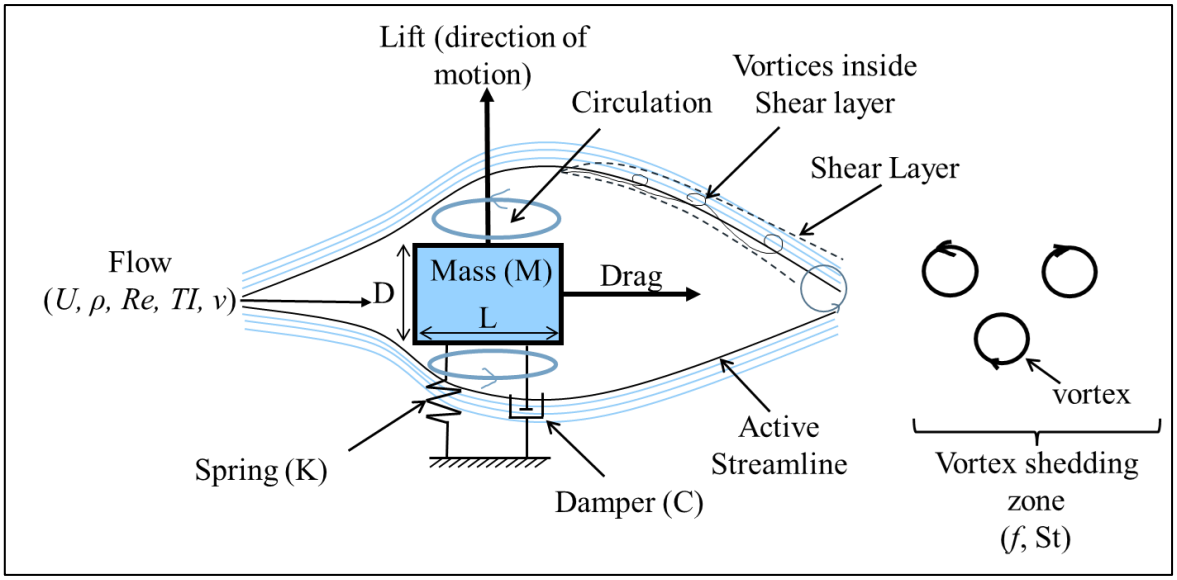

Figure 2.1: A schematic diagram of the fundamentals of wake galloping caused by fluid-structure interactions [29]

Alonso *et al.* [30] have studied the transverse galloping of a triangular cross-section tip body with an aft cantilevered structure. They performed a series of wind tunnel experiments and determined the relation between the transversal displacement of triangular tip mass by changing the angle of attack. They observed that when the incident flow is lined with the lateral sides of the tip mass, the isosceles triangular shows the galloping instability at the lower critical velocity. Mahadik and Sirohi [31] considered a D-shape tip mass and performed experiments to study galloping and corresponding energy harnessing. They explored the impact of several system characteristics such as material of the beam, wind flow velocity, electrical load, and natural frequency of the beam on the output power generation. Yang *et al.* [32] evaluated the effectiveness of the harvester in converting flow energy to electrical energy by using various bodies with different cross-sections (D-shaped, triangular, rectangular, and square sections). In comparison to other sections, the square section is shown to be the most efficient. The output power is 8.4 mW, at a flow velocity of 8 m/s. In a similar manner, a comparison among different models used in galloping based energy harvesting is done by Zhao *et al.* [33]. In general, there are three types of electromechanical galloping based energy harvesting models available,

which include Rayleigh-Ritz discretization model with approximated distributed parameter, a lumped parameter one degree of freedom model, and the Euler-Bernoulli model with distributed parameter multi degree of freedom models. Based on the comparison study, results show that the Euler-Bernoulli distributed model produces consistency in the aerodynamic forces, whereas single degree freedom model gives a better prediction in critical flow velocity. The effect of the tip body (shape, tip length, and weight) on the aeroelastic characteristic of galloping-based energy harvesting was explored by Zhao *et al.* [34]. They performed wind tunnel experiment using different shapes of tip body, i.e., circular, semi-circular, and square body and found that a square cross-section at the tip produces maximum galloping based piezoelectric power output of 8.4 mW at a flow velocity of 8 m/s. They also established an analytical model integrating with the aerodynamic and electromechanical formulation. In the same manner, the influence of tip mass length ratio on galloping-based piezoelectric energy harvester has been quantitatively explored by Yaghoub and Jamalabadi [35]. They consider D-shape bluff body as a tip mass and produces a 100 mW power output at a flow velocity of 20 m/s.

Zhang *et al.* [36] experimental investigated the optimum design for a wind energy harvester with the use of an interference cylinder (IC) using different cross sections (triangular, circular, D-shape, square and flat plate). The maximum average power output of 803.4 μW at a flow velocity of 2.36 m/s with square IC at a spacing ratio of 0.9 is achieved. The experiment results show that the flat plate interference arrangement has a higher power output over other arrangements, especially in the occurrence of vortex-induced vibration. Apart from the conventional geometry, there are different types of non-conventional geometries that have also been used for galloping based energy harvesting.

A novel curved plate bluff body is used to enhance the performance of the galloping based energy harvester by Zhou *et al.* [37], as depicted in Figure 2.2 (a). The experimental results are

compared with the conventional cross section (triangular, square, and D-shape) with the curved plate, and it is noted that the curve plate bluff body generated higher output voltage. They vary the arc length of the curve plate and find out that 45 mm arc length with 820 KΩ optimum load resistance generates a maximum power output of 35.6 μW at a flow velocity of 5.5 m/s. Wang *et al.* [38] have investigated the novel high performance of galloping based piezoelectric energy harvesting with Y-shaped (GPEH-Y) attachments, as shown in Figure 2.2 (b). When the additional attachment is removed from the bluff, vortex-induced vibration piezoelectric energy harvester (VIVPEH) is obtained. The results show that an additional attachment on the bluff body changes the aerodynamics characteristic of galloping based energy harvester compared with the VIVPEH. The threshold flow velocity for the VIVPEH 1 m/s ≤ U ≤ 1.42 m/s, which is lower compared to the GPEH-Y is U ≥ 1.28 m/s. In the case of VIVPEH, the lock-in region was observed earlier than the GPEH-Y. A novel fork-shaped bluff body is used to improve the performance of the galloping based energy harvester by Liu *et al.* [39], as depicted in Figure 2.2 (c). The experimental results are compared with the conventional cross section (triangular and square) with the fork-shaped bluff body, and it is noted that the fork-shaped bluff body generated higher output voltage. They vary the front blade length (l_f) of the fork-shaped bluff body and find out a 10 mm front blade length with 1000 KΩ optimum load resistance generates a maximum power output of 1.07 mW at a flow velocity of 5 m/s. Hu *et al.* [40] numerical and experimentally designed a comb-like beam (CombBeam) based PEH that uses the galloping process to capture wind energy, as shown in Figure 2.2 (d). A series of parasitic beams are mounted to a standard cantilever beam with a piezoelectric transducer in the CombBeam-based PEH. The result demonstrates that when compared to a traditional beam GPEH, the CombBeam-based GPEH has a lower fundamental natural frequency and a lower cut-in wind speed, indicating that the Comb Beam-based GPEH is better for low-speed wind energy harvesting.

To determine the dynamic features of galloping-based piezoelectric energy harvesters, a geometrically non-linear finite element (FE) approach was developed by Dash *et al.* [41]. Both structural and aerodynamic nonlinearity are addressed in the developed model. Their study favours a numerical technique over traditional analytical solutions (FE) to tackle the GPEH system's intricate fluid and structure problems.

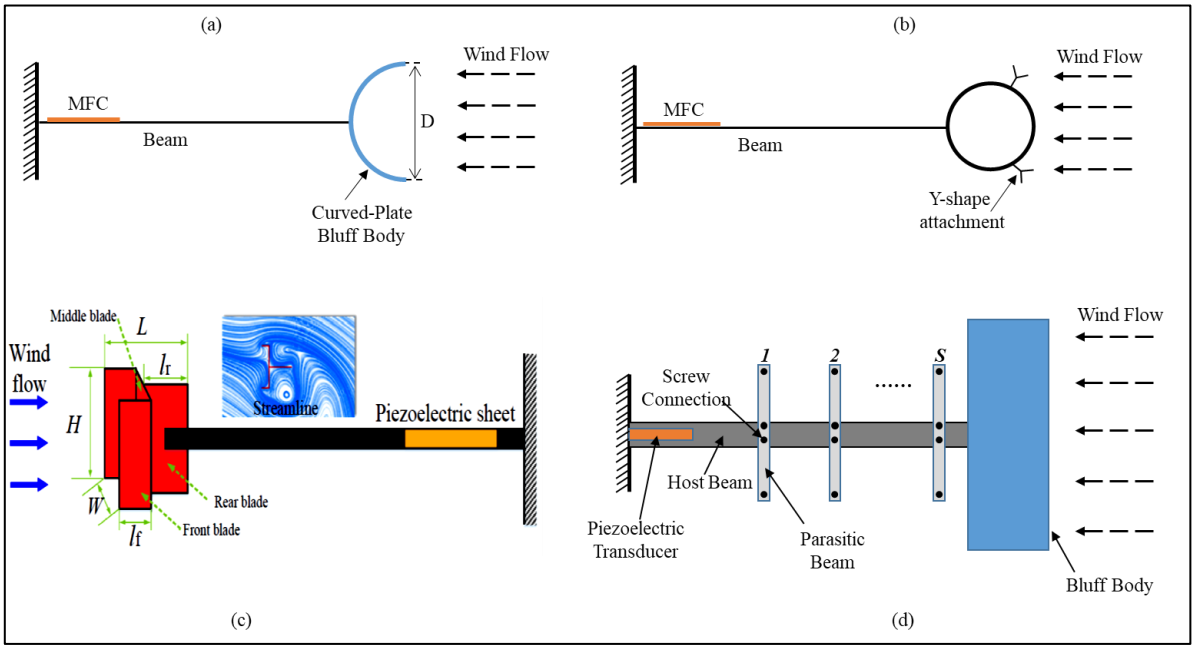

Figure 2.2: Schematic diagram of (a) curved plate, (b) Y-shaped, (c) fork-shaped, and (d) comb-like wake galloping energy harvester system, respectively

It is observed that many studies have been conducted to improve the performance of galloping-based energy harvesting systems. A system of a cantilever strip with a tip bluff body is commonly utilized, and in order to improve output, various shapes of the tip body, viz., square, triangular, D-shape, etc., are extensively researched. The majority of study on transverse galloping is focused on understanding flow dynamics in order to better define the corresponding drag and lift forces. The vortex field and lift generated by different geometries results in different vibration amplitude and, subsequently energy output. The piezoelectric transduction mechanism was used by the majority of the researchers to harvest energy since the main premise of piezoelectric energy harvesting is that it depends on the strain created in

the structure, i.e., the more strain in the beam/structure, the more energy may be harvested. It is important to understand that, aforesaid systems, beam/structure oscillates in first bending mode. As a result, the researcher faces a problem in designing a galloping based piezoelectric energy harvester that can vibrate in a high bending mode and generate more energy.

2.3 Flutter instability

Flutter instability is caused by the flow elastic coupling of the attached flow and occur over a certain flow velocity. It can be seen in a variety of conditions, e.g., a gentle breeze over a flexible flag creates instability in the flag, a gust creates flutter in airplane wings, etc. For a long time, researchers have been fascinated by the process that causes flutter instability. Generally, flutter instability is studied in two types of configurations, i.e., (a) an airfoil rigid section with flexible support, (b) a flag like structure that shows continuous distribution of mass and flexibility. The airfoil section under flutter shows coupled mode vibration under bouncing and torsional mode, whereas the flag shows combined bending mode oscillations. As the present research revolved around the flutter of the plane structure, the scope of the literature review is restricted to instability of the plane structure in flow, although, from the energy harnessing aspect, brief details of other systems are also addressed.

According to Dowell [42] flutter instability is arisen due to fluctuation in pressure at the close vicinity of the plane structure, the flow remains attached, and tail vortices trigger the self-sustainable oscillation in the structure. Since the earliest study by Taneda [43] about flutter of waving motion in a flag, extensive studies focused on mitigating the flutter instability have been carried out till now.

In theoretical studies, a cantilevered thin sheet fixed at the leading edge interacting with the flow has been used as a basic model to investigate unstable oscillations that occurred in many industrial applications [43,44] and natural phenomena [46–48]. Huang [46] investigated

vibration of soft palate responsible for human snoring. He examined flutter of a cantilevered plate in axial flow and was mainly interested in the initial stage of the instability that arises at a critical flow velocity. Wind tunnel testing along with the classical Theodorsen's flow model was conducted. Watanabe *et al*. [44] adopted a comprehensive flow model using Navier-Stokes equation and predicted flutter in paper sheets. They reported a mixed mode vibration of a cantilevered paper sheet at 1.6 m/s flow velocity. Argentina and Mahadevan [49] have proposed a landmark methodology to find flutter in plane structure using thin airfoil theory. The unsteadiness of the flow, vortex shedding from the trailing edge, and effect of additional mass are all explained by thin airfoil theory. This theory can predict the critical velocity of flutter of flapping flag as well as flapping frequency. Eloy *et al.* [45] have developed a 1D structural model of flag with 2D flow field using potential flow model and showed instability under incompressible axial flow conditions. They reported a single neck and a three neck bending mode shape of structure at different flow velocities. Similarly, different theoretical models considering both linear and nonlinear approximation are proposed by different researchers [50, 51], and a variety of cases have been analyzed. In addition to finding critical velocity of flutter, post critical behaviour wherein structure shows LCOs is also remained a field of interest since a long time [52].

In accordance with theoretical investigations, ample experimental study of flutter in a variety of structures is performed. Taneda [43] was the first who carried out wind tunnel experiments and observed waving mode in a flexible flag defined by a cantilever plane structure fixed at the leading edge. He reported that flag exhibits vibration in different modes that is governed by the relative mass of the flag and density of the flowing fluid. Watanabe *et al*. [53] have experimentally analyzed flutter in paper sheets. In addition, they also evaluate the effect of in tension in the sheet, material of sheet, geometry, and mass ratio on the flutter characteristics. Patil [54] examined flutter in the airplane and showed generation of limit cycle oscillation

(LCOs) due to drag involved in the process. Due to flutter induced drag, the aircraft undergoes limit cycle oscillations (LCOs). In wind tunnel testing, Chen *et al.* [55] have observed that at the time of arrival of flutter, the flag exhibits oscillation in second bending mode, and higher mode vibration appears with the increase in flow velocity. The same has been confirmed by Virot [56]. Recently, Kumar *et al.* [57] have carried out comprehensive testing on flutter of a flag and various aspects of structural dynamics and flow dynamics are analysed. They reported that flutter occurs with the second bending mode, by passing the first mode and the flow remains attached even after the large oscillation happened in the flexible flag. In numerical work, the flow has been simulated using standard flow models, thin aerofoil theory [49, 58], vortex shedding model [59, 60], potential flow model [42, 61], Navier stokes [44, 62], etc.

Above mentioned review indicates that the dynamics of movement induced excitation (MIE) are systematically examined in several numerical and experimental studies, although the focus of the research was mainly on understanding the dynamics of coupled FSI and mitigating the structural vibration. The results clearly indicate that flutter arrives at second mode and shifts to higher mode with increase in the flow velocity. Moreover, a number of discrepancies have been observed between theoretical and experimental predictions of flag flutter [63]. In last two decades, major efforts have been dedicated to get an accurate prediction of critical velocity of flutter [50, 64, 65], although less attention has been given to harvest energy from plane flutter.

Energy harvesting from flutter instability

An aeroelastic energy harnessing system is a compact and suitable source to convert wind energy into useful electrical energy. These devices are apt for situations where solar energy is absent, like ducts and geographical poles where no solar energy but wind is present. In order to extract energy from flutter, normally a solid pin connected flap (airfoil shape or plane panel) at the end of a cantilever beam is subjected to flutter, and suitable transduction is employed to harvest energy.

Bryant and Garcia [66] first introduced a novel flutter-based harvester using a piezoelectric transduction based mechanism consisting of a pinned flap at the tip of a cantilever beam, as shown in Figure 2.3 (a). The system in flow shows flutter beyond a critical velocity and limit cycle oscillation at higher flow velocity. A linearized mathematical model is developed to predict critical velocity of flutter, and to study limit cycle oscillation an empirical non-linear model that takes dynamic stall into account is used. Wind tunnel experiments are also performed to validate analytical predictions. In a subsequent study [67], they explored the sensitivity of the proposed system against different system parameters. Hafezi and Mirdamadi [68] have modified a similar system by adding a sliding mass over the beam length and carried out detailed theoretical investigations for energy harnessing aspect. The addition of sliding mass allows system to operate for a wider range of input flow velocity and enhances overall energy extraction by piezoelectric transduction, as depicted in Figure 2.3 (b). Different position of mass influence arrival of flutter and enables the system to tune for a broad range of flow velocity.

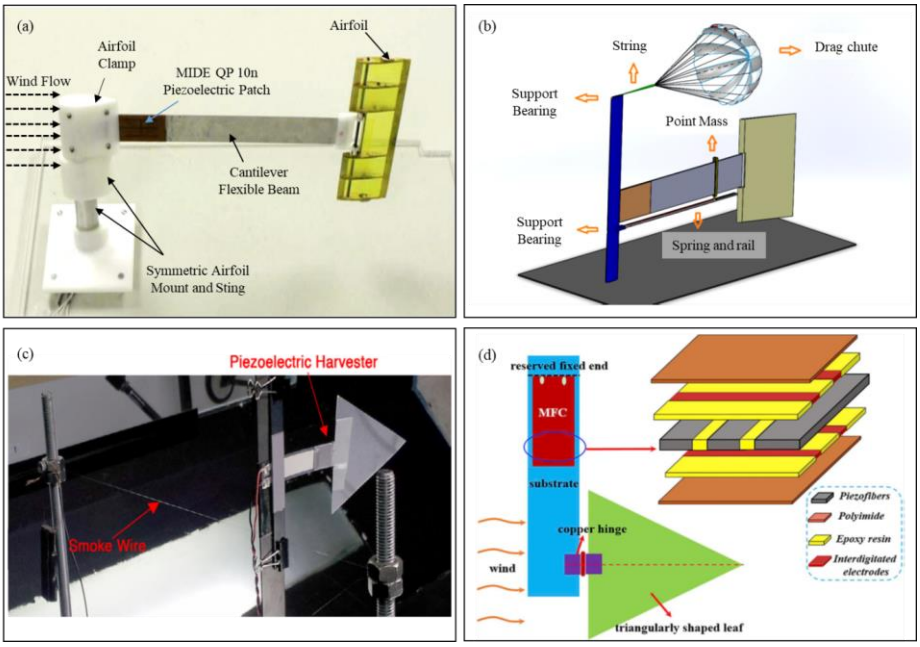

Figure 2.3: (a) Prototype of aeroelastic flutter-based energy harvester [66], (b) 3D model of piezoelectric harvester setup [68], (c) a test model of cantilever PVDF leaf-stalk [69], and (d) schematic diagram of flutter-based energy harvester [70]

Dickson [71] proposed the concept of piezoelectric tree that exploits wind energy to generate electrical power. The tree comprises a piezoelectric patch (the stack) pinned to a triangular polymeric membrane (the leave). Later, McCarthy *et al.* [69] examined the performance of a harvester consists of a triangular flap pinned at the tip of a cantilever structure in the axial flow, as shown in Figure 2.3 (c). The mechanical power is converted into electric energy using piezoelectric PVDF material. They have also compared their work with [67] in terms of changing the flexibility of cantilever structure. Further, Liu *et al.* [70] considered a triangular pin connected flap at a vertically oriented cantilever beam, as shown in Figure 2.3 (d), and piezoelectric Micro Fibre Composite (MFC) element is used to convert mechanical vibration energy into electric energy. The beam displayed large amplitude flapping while the flap flutter in the flow. Series of tests performed corresponding to variety of base material of beam as well as different grades of piezoelectric material and it is reported that both thickness of piezoelectric material and flexibility of base material influences overall power output. They reported that for a given set of MFC with Al base, 82 V open circuit voltage at a flow velocity of 7.5 m/s is observed that can meet the power requirement of a traditional MEMS device. On a similar concept, different non-traditional mechanisms using different transductions are researched.

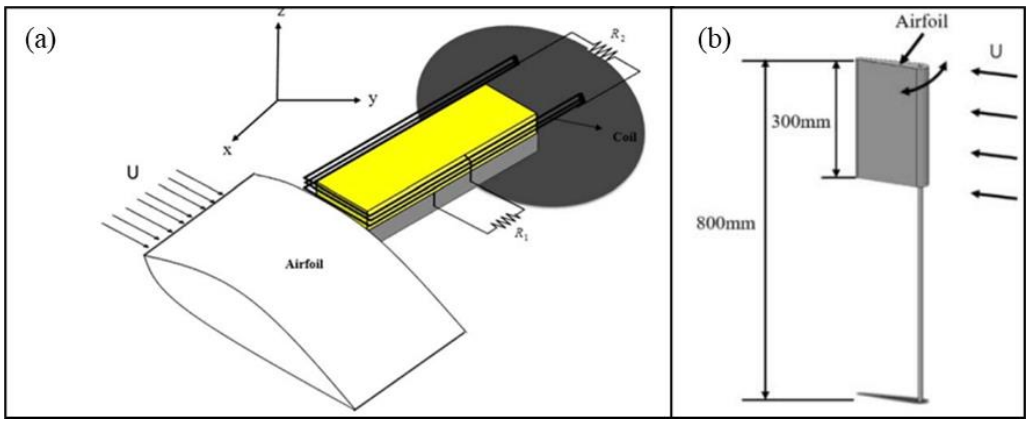

Figure 2.4: (a) Elastic beam with magneto-electro-elastic layer [72], (b) airfoil on a vertical beam [73]

A rigid airfoil connected on an elastic beam with magneto-electro-elastic layer used by Abdehvand [72], as shown in Figure 2.4 (a), and airfoil on a vertical beam that can swing at the base to aligned airfoil with the flow direction, as depicted in Figure 2.4 (b) [73], are a few examples of such systems. Some conceptual models are also proposed and analyzed both experimentally and computationally, e.g., Figure 2.5 (a) shows electromagnetic aeroelastic energy harvester [74], and Figure 2.5 (b) depicts a airfoil flap with torsional flexibility and electromagnetic conversion strategy [75], Figure 2.5 (c) shows electromagnetic conversion based fluttering of a flat belt in the Karman Vortex field from a cylinder [76], Figure 2.5 (d) depicts T-shaped pinned cantilever under rotational flutter [77]. A number of investigations considering similar structure have been carried out in the past [75, 78–80].

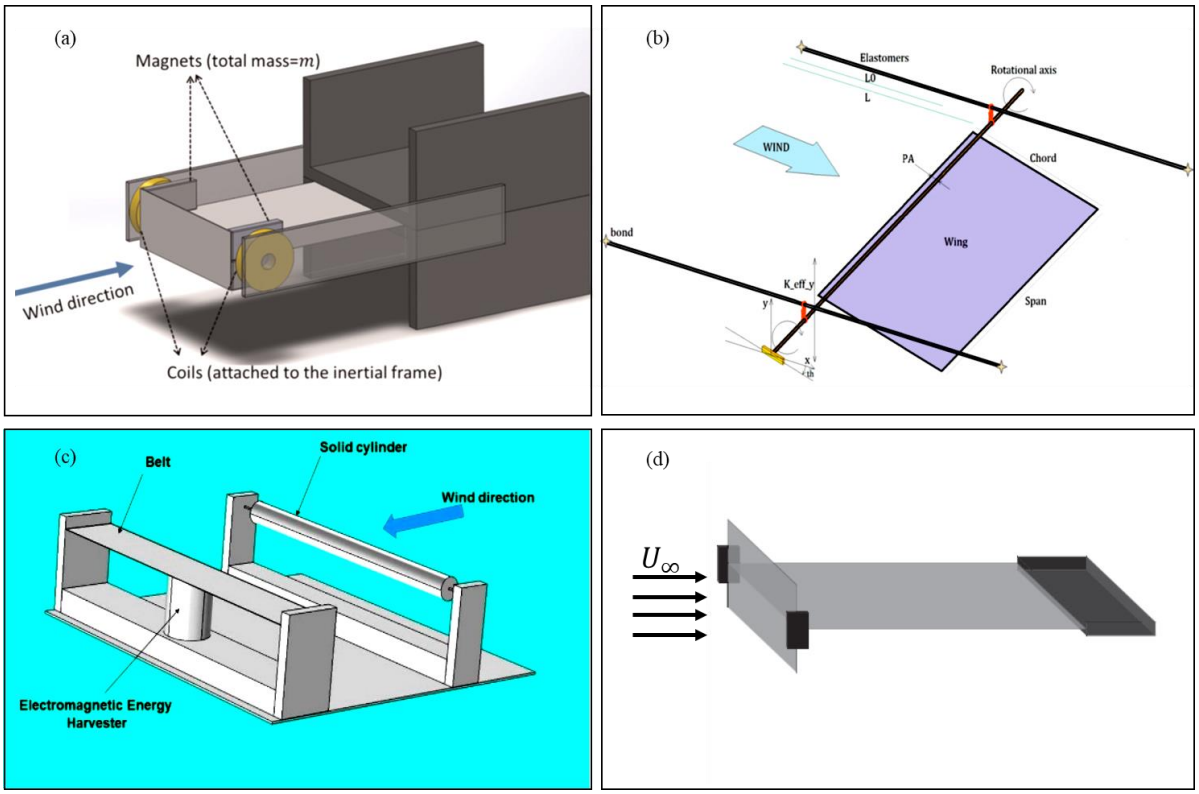

Figure 2.5: (a) 3D model of flutter-based electromagnetic energy harvester [74], (b) a prototype of autonomous powering system [75], (c) physical test model for electromagnetic energy harvester [76], (d) T-shaped cantilever electromagnetic energy harvester [77]

Contrary to extraction of energy from the flutter of a rigid body at the tip of a flexible beam, flutter of a flag like structure is also employed to harvest energy. It is worth to understand that in aforementioned systems, the body under flutter forces the generator mechanism (the beam part) to vibrate in its first bending mode. Particularly during piezoelectric transduction, the strained imparted to the piezoelectric layer is corresponding to first bending mode of the cantilever structure. However, in the case of the flag flutter, the structure oscillates in higher bending mode and results in different strain distribution in the piezoelectric layer.

Based on the previous experience on flutter dynamics of a two-dimensional cantilevered thin flexible plates in subsonic axial flow [81], Tang *et al.* [82] have proposed a concept of a new energy-harvesting device, the ‘‘flutter-mill’’ using flutter of a plane sheet at sufficiently high wind velocity, as shown in Figure 2.6 (a). In their numerical study, a non-linear model of a 2D plane structure is used to predict onset of flutter and subsequent post critical LCO of the sheet. A flexible metallic plate with embedded conductors between two parallel magnetic panel is considered. The flapping motion of the plate results in electric potential generation at its upstream and downstream ends. A maximum power output of 10 W taking a flow velocity at 13 m/s is reported. An analogues model of flutter mill is further researched by Dunnmon *et al.* [83] to extract energy using piezoelectric transduction. The LCO of the plate under flutter is employed to extract energy. Both numerical and experimental investigations are carried out and in testing 2.5 mW power at a flow velocity of 27 m/s is reported. The location of the piezoelectric patch is analyzed based on the mode of vibration of the sheet that appears during flutter. The patch was located at the nodal position of the second mode of a cantilever structure that was found to be dominant in the LCO. Recently, Eugeni *et al.* [84] numerically designed a flag flutter-based harvester and tested experimentally, as shown in Figure 2.6 (c). The dynamics of flutter of a sheet and LCO are numerically predicted, and wind tunnel testing is followed. Piezoelectric (PZT) material is employed for conversion of mechanical energy into

electric energy. In order to check the performance of the of the harvester, the power generated during the testing is measured at variable external resistance. The pitot tube is used to measure flow velocity, and high speed images are captured to get flutter amplitude. Frequency of oscillation is measured by sequential image processing of tip deflection. Two different lengths of the flag 20 cm and 23 cm are considered, and a maximum power of 1.12 mW at 23 m/s flow velocity is reported. Subsequently, from the same group of researchers, by changing the material of the base structure, a power output of 6.67 mW at 25 m/s velocity is reported.

Doare and Michelin [85] have numerically investigated the flutter of a plane structure in axial flow and corresponding energy harvesting using piezoelectric material. The plane structure is sandwiched with the piezoelectric material. The focus of their study was to find out the effect of piezoelectric coupling on linear stability and fluid solid energy generation. They extended their study [86] to investigate the effect of nonlinearity in the system and enhancement in fluid solid energy harvesting. With a non-traditional configuration of vertically oriented flag in wind flow, Zakaria *et al*. [87] have experimental investigated self-induced flutter of a composite beam and harvest wind energy using piezoelectric patch. Flutter is experimentally visualized for different angle of attack, and a subsequent energy generation is studied. The outcomes demonstrate that the frequency of oscillations is strongly influenced by angle of attack and wind velocity. It has been observed that the stiffness of the beam is substantially affected by geometric nonlinearities for high deflections in the composite beam and marginal shift in its natural frequency, which closes to its second bending and torsional frequencies, causing self-induced flutter in the beam. In a similar study of extracting energy from the flutter of a non-conventional system, flutter of two adjacent cantilevered beam placed in vertical orientation (Figure 2.6 (d)) is studied by Hobeck and Inman [88], and it is reported that with an appropriate gap between the two structures, both beams have experienced high amplitude vibration in out of phase fashion.

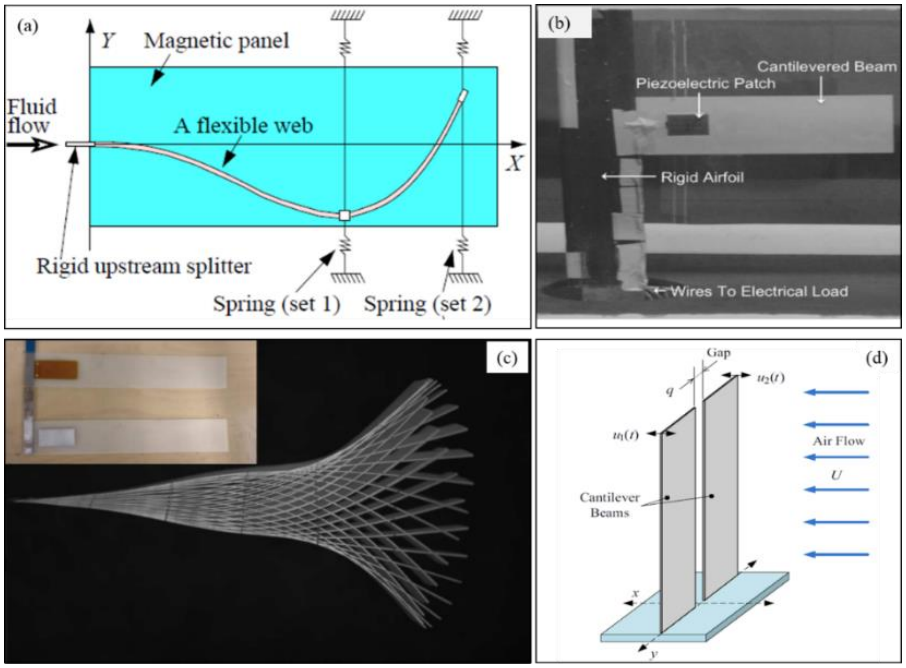

Figure 2.6: (a) Layout of concept of flutter mill [82], (b) experimental setup of flutter-based energy harvesting [83], (c) deformation of cantilever PZT patched flag [84], and (d) schematic of dual cantilever flutter mechanism [88]

Manela and Howe [4, 52] have numerically investigated the dynamic behavior of a flapping flag attached to a cylindrical pole of finite diameter. Two cases of FIV with and without consideration of effect of flag pole on vibration of plate are explored. The region of minimal instability is determined by study of self-induced oscillation, including the balance between inertia of flag, varying tension, fluid loading, and bending rigidity. When the cylindrical pole is attached with the flag, vortex shedding will usually occur from the cylindrical pole at mean flow velocities of the fluid that are substantially subcritical, i.e., at which velocity the homogeneous theory predicts a stable behavior. It is observed that the critical velocity of instability reduces due to presence of flow disturbances generated from the upstream flag pole.

From the literature survey, in addition, ample work is presented on vibration energy harvesting using piezoelectric material or other means. It is noted that the focus of majority of work on flutter/vortex-induced vibration related studies is mainly to understand flow dynamics for further detailing the associated drag and lift forces. Additionally, research on energy harvesting

from piezoelectric material is mainly carried out for general structural vibration (mainly by electromagnetic exciter). It is obvious that flow energy harvesting is a promising area of research and, in the last decade, plenty of effort has been made to improve performance of the flow energy harvester through the frontal bluff body (square and cylinder), but a few works have done by using different bluff bodies (D-shape, Triangle etc.) at low Reynolds number. Also, detailed research related to energy harvesting from flow-induced vibration using piezoelectric material is rare.

2.4 Summary of literature review

In this chapter, literature related to flow-induced vibration and corresponding energy harvesting by different flow-induced vibration mechanisms (MIE, EIE, VIV etc.) using different transduction mechanism is reviewed. There is substantial literature on flow-induced vibration and the use of various numerical/computational approaches to the analysis of a variety of fluid structure interaction (FSI) problems. Flow over a cylinder, flexible plates, long cylinder, electric cable, and long chimney in flow are a few examples of FSI.

The main goal of this thesis is to figure out how a bluff body affects flow-induced vibration of a flexible structure in flow and its effect on the corresponding energy harvesting. Therefore, the flow-induced vibration literature survey is divided mainly into three categories, i.e., (i) Vortex-induced vibration, (ii) galloping, and (iii) flutter.

Table 2.1 shows a summary of various researches about flow-induced vibration based energy harnessing. Based on the review and relative comparison, following important points are observed.

1. It may be concluded that there is significant research done on the flow-induced vibration of elastically mounted rigid structures and flexible beam/plate like structures. Equivalent to VIV of rigid structure, several studies carried out on the wake induced

vibration of flexible beam/plate like structures under the influence of wake flow is studied. The majority of work on wake induced vibration research is primarily focused on understanding flow dynamics in order to further describe the associated drag and lift forces. However, few works are presented on vortex-induced vibration energy harvesting using piezoelectric material or other means.

Table 2.1 Detail of energy harvested by different mechanisms

Mechanism	Numerical/ Experimental	Flow Velocity (m/s)	Flow Medium	Transduction Mechanism	Model	Power output (mW)
VIV	Experimental	7.23	Air	PVDF	Cylinder	0.004 [89]
	Both	10	Air	PZT	D-shape	0.1 [90]
	Experimental	8	Air	PZT	D-shape	2 [91]
	Numerical	0.67	Air	PZT	Cylinder	0.35 [23]
	Numerical	5	Air	PZT	Cylinder	1 [92]
	Experimental	0.35	Water	PZT	Cylinder	0.084 [93]
Transverse Galloping	Experimental	1.56	Air	PZT	D-Shape	1.14 [31]
	Experimental	8	Air	PZT	Square	8.4 [32]
	Experimental	5.5	Air	MFC	Curved plate	0.036 [37]
	Experimental	2.3	Air	MFC	Y-Shaped	1.2 [38]
	Experimental	3.5	Air	PZT	Comb Like	0.15 [40]
	Experimental	3.05	Air	MFC	Iced D-shaped	0.1 [94]
	Experimental	4.05	Air	MFC	Square	5.99 [95]
	Experimental	5	Air	MFC	Fork Shaped	1.07 [39]
	Experimental	2.51	Air	PZT	Square	0.003 [96]
	Both	2	Air	MFC	Cylinder	0.27 [97]
Flutter	Experimental	8	Air	PZT	Fixed-free Beam with a pinned Airfoil at tip	3.3 [68]
	Experimental	7.5	Air	MFC	Fixed-free Beam with a pinned Triangular leaf	0.54 [70]
	Numerical	15	Air	Magneto electro	Fixed-free Beam with a pinned Air foil	8.3 [72]
	Experimental	8	Air	Electromagnetic	T-shaped cantilever structure	1.1 [74]
	Experimental	10	Air	MFC	Vertical beam of carbon fiber	0.3 [87]
	Experimental	27	Air	PZT	Airfoil	2.5 [83]
	Experimental	13.8	Air	PVDF	Cylinder	0.07 [98]
	Both	23	Air	PZT	Flag like plane structure	1.12 [84]
	Both	25	Air	PZT	Flag like plane structure	6.7 [3]
	Both	14	Air	PZT	Dual cantilever beam with Airfoil	2.4 [99]

2. It is observed that many studies have been conducted to improve the performance of galloping-based energy harvesting systems. A system of a cantilever strip with a tip bluff

body is commonly utilized, and in order to improve output, various shapes of the tip body, viz., square, triangular, D-shape etc., are extensively researched. The piezoelectric transduction mechanism was used by the majority of the researchers to harvest energy since the main premise of piezoelectric energy harvesting is that it depends on the strain created in the structure, i.e., the more strain in the beam/structure, the more energy may be harvested.

3. An extensive literature on experimental and numerical work has been reported on flow-induced vibration of both flexible and rigid structures in flow. Three different types of flow-induced vibration mechanisms: VIV, galloping and unstable flutter have been carried out. However, it has been noticed that basic flow models, such as the discrete vortex model, potential theory, thin airfoil theory, and others, have been used in the majority of numerical investigations, which are insufficient to investigate the complicated problem of FSI. In line with this, few work has been carried out on Reynolds Average Navier Stokes (RANS) equation along with the fully coupled FSI (two way FSI) modelling.
4. Most of the work on flow over a flexible structure in flow is mainly focused on numerical investigation effect of the various design parameters, material properties etc., on the dynamics of flutter analysis and is limited to laboratory level.
5. From the number of literature reviews, it has been found that no comprehensive investigation is so far reported on the role of additional wake field on the critical velocity of flutter of a plane structure, and more importantly, this aspect has not been considered from the point of view of improvement in the performance of flutter energy harvester.

2.5 Research Objectives

The aforementioned literature review reveals that increasing the vibration level induces higher strain in vibrating structure, which eventually leads to higher charge yield from smart materials. Therefore, efforts are demanded to increase amplitude of flow-induced vibration either by

putting the system in higher flow velocity or by altering the system geometry to get higher vibration at lower velocity. The prime interest of the present work is to study dynamics of flow generated vibration of a beam/plate like structure. For this purpose, the geometry of the structure is planned to modify. However, small efforts will be made on modeling and computing charge generation from a plate with piezoelectric membrane.

The following objectives of the proposed work are coined:

1. To model and simulate flow-induced vibration of a flat plate with an upstream bluff body and validation of the results obtained.
2. To study influence of different geometrical shapes of upstream bluff body on the level of vibration and corresponding modal characteristics of vibrating system (deformation shape, frequency of oscillation etc.).
3. To calculate overall strain generated in the different cases and electro-mechanical modeling to calculate subsequent energy harvesting.
4. To experimentally:

   (a) Identify critical speed of flutter instability and validation with available standard results.

   (b) Study the influence of presence of a bluff body on critical speed of flow-induced vibration.

   (c) Test effect of shape of upstream bluff bodies on critical velocity.
5. To compare the results obtained from numerical and experimental studies.

CHAPTER 3

NUMERICAL STUDY OF FLOW OVER A FLEXIBLE PLATE

In this chapter, the dynamics of a flexible structure in the flow field are numerically solved and analyzed. The purpose of the computational investigation is to get a preliminary idea about the influence of flow on the vibration characteristics of the plane structure. All investigations are conducted on a test model of a plane cantilevered structure in axial flow conditions. The entire simulation study is carried out in two phases.

- In the first part, the fluid-structure coupling is considered, and vibration of the flexible structure under the wake field of different bluff bodies is studied. All simulations are performed using two-dimensional computational domain with transient flow modelling. It is worth noting that the primary source of excitation of the flexible structure is vortices generated from the front obstacle (bluff body), and the small turbulent eddies in the flow will merely influence the dynamics of the structure. Since the aim of the analysis is to understand the effect of wake field on vibration, low Reynolds number conditions are assumed to be sufficient to serve the purpose, and so the simulations are performed at a Reynolds number (Re=200) value which has also advantageous in terms of lower computational efforts. Before the final simulation run, several validation studies, i.e., mesh convergence, time step convergence, and domain convergence, are carried out.
- In the second section, flow simulations with air as flow medium are performed. It may be noted that the low Reynolds number flow study is primarily done for verifying the

conjecture about variation in the resultant flow-induced vibration of a flexible structure under the wake flow of different upstream bodies. However, to get an idea of real life environment, simulation considering air as the flow medium is performed. As the motion of flexible structure before the arrival of flutter instability is negligible, a rigid structure can serve the purpose of visualization of flow distribution around the body when flutter arrives and hence considered to reduce the computational efforts.

3.1 Numerical Methodology

3.1.1 Flow solver

In order to visualize the flow field around the structure, 2D transient flow simulations are performed. All simulation studies are carried out in ANSYS Workbench. The CFX solver is a flow module that takes care of all aerodynamic computations of the flow. The flow-field is computed by solving the unsteady Navier-Stokes equation (N-S) in their conservative form [100].

$$\frac{\partial \rho}{\partial t} + \nabla.(\rho V) = 0 \tag{3.1}$$

$$\frac{\partial(\rho u)}{\partial t} + \frac{\partial(\rho u^2)}{\partial x} + \frac{\partial(\rho uv)}{\partial y} = -\frac{\partial p}{\partial x} + \frac{\partial \tau_{xx}}{\partial x} + \frac{\partial \tau_{xy}}{\partial y} + \rho f_x \tag{3.2}$$

$$\frac{\partial(\rho v)}{\partial t} + \frac{\partial(\rho uv)}{\partial y} + \frac{\partial(\rho v^2)}{\partial y} = -\frac{\partial p}{\partial y} + \frac{\partial \tau_{yx}}{\partial x} + \frac{\partial \tau_{yy}}{\partial y} + \rho f_y \tag{3.3}$$

where

$$\tau_{xx} = \lambda(\nabla.V) + 2\mu\frac{\partial u}{\partial x}, \qquad \tau_{yy} = \lambda(\nabla.V) + 2\mu\frac{\partial v}{\partial y}, \qquad \tau_{xy} = \tau_{yx} = \mu\left(\frac{\partial v}{\partial x} + \frac{\partial u}{\partial y}\right)$$

Variables ρ, u, v, p and τ_{xx} are instantaneous density, velocity, pressure and shear viscosity of the fluid, respectively; where μ is the coefficient of molecular viscosity and λ is second viscosity coefficient ($\lambda = -\frac{2}{3}\mu$). The flow domain is discretized in a number of finite volumes, wherein the solution variables are stored at mesh nodes or vertices [101]. Around each node, a finite element is constructed, and governing equations are integrated over each finite volume. In computation, the advection term of the N-S equation is calculated using a second-order

accurate high-resolution scheme. For the time-varying terms, the Euler method is applied to capture the change in flow domain.

3.1.1.1 Structural solver for FSI computation

The structural solver executes dynamic analysis by applying an equation of motion consisting of the inertial, damping, and elastic properties of the flexible plate.

$$[M]\{\ddot{X}\} + [C]\{\dot{X}\} + [K]\{X\} = \{F(t)\} \tag{3.4}$$

where [M] represents mass matrix, [C] depicts damping matrix, and [K] represents stiffness matrix. Vectors $\{\ddot{X}\}$, $\{\dot{X}\}$, $\{X\}$, and $\{F(t)\}$ denote nodal acceleration, nodal velocity, and nodal displacement, and load vector, respectively. The structural solver uses finite element based formulation approach which further relies on Newmark time integration method to calculate resultant displacement vector. The FSI problem exhibits transient nature, wherein two solvers are linked to each other. In each cycle of time marching, fluid pressure and structural displacement data are manually exchanged. A common interface between two physical domains is required for coupling. Figure 3.1 shows the schematic of the entire computational methodology. For the FSI, a coupled fluid model is being examined. The entire study is followed by preparation of a model of computational domain, model of solid structure, discretization of structural and flow domain using CFX and transient modules of ANSYS Workbench, respectively, and after then, output is postprocessed to visualize mode shapes, frequency of oscillation, strain distribution corresponding to solid structure. The flow field is analyzed by plotting pressure contours, vorticity contours, and velocity distribution in the flow computational domain.

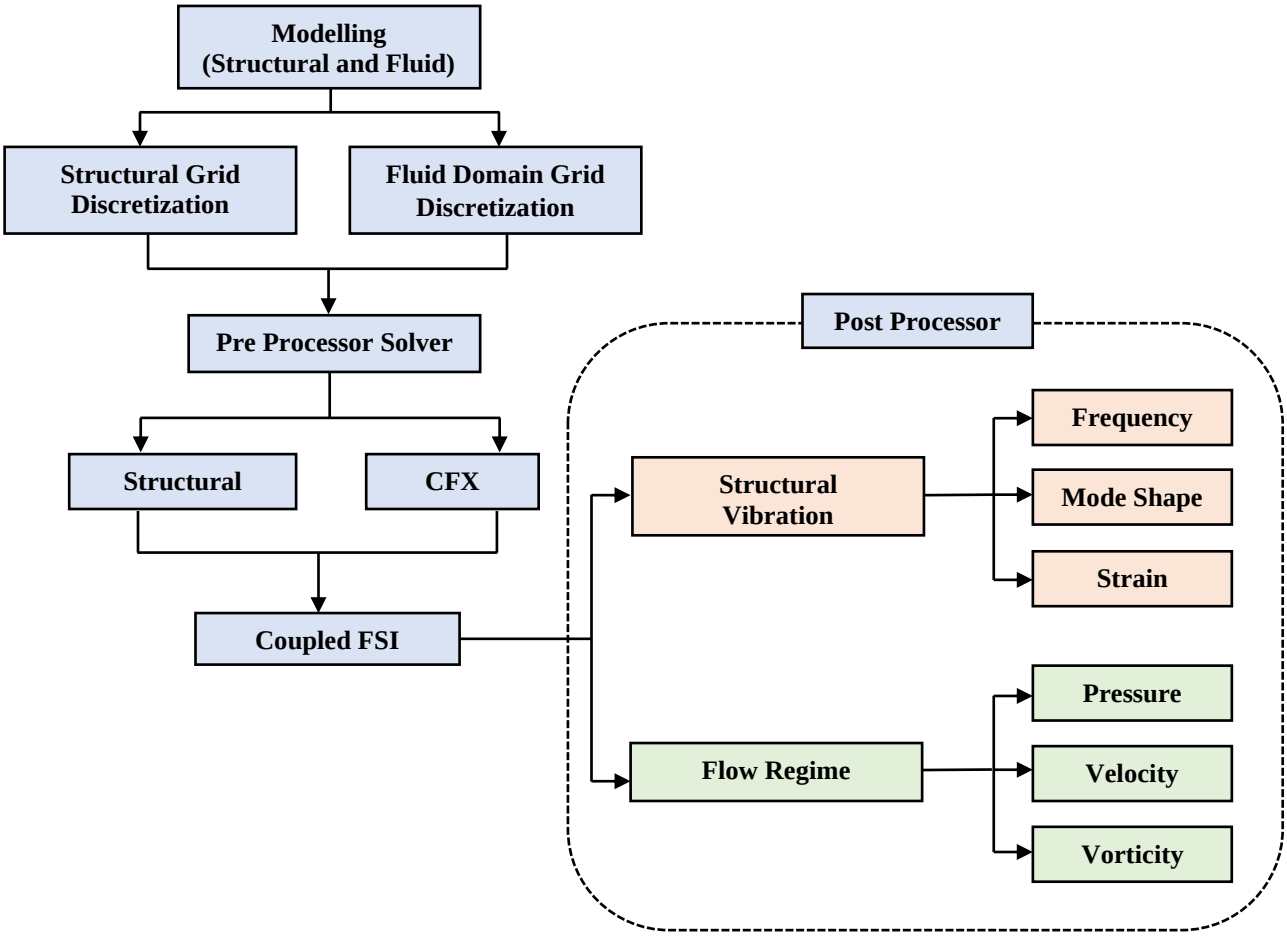

Figure 3.1: Schematic representation of coupled FSI model

3.1.1.2 Test model

The analysis is performed on a test assembly of a 2D flexible plate with an upstream rigid bluff body. Initially, a flat obstacle is considered as a bluff body, and flow-induced vibration is computed. Figure 3.2 (a) shows the schematic of test assembly. The ratio of the plate length (L) to the bluff body size (D=5 cm) is kept at 10, and the thickness of the plate is kept 1 mm. The young modulus and Poisson ratio of the plate are considered as E=200 GPa, and ϑ = 0.3, respectively.

3.1.1.3 Flow computation domain

Figure 3.2 (a) shows the schematic of 2D flow computation domain with different boundary conditions. The top and bottom walls are considered no-slip wall boundaries that are defined

by assuming zero tangential velocity of the fluid at the surface of the wall. At inlet boundary, an input flow velocity of 30 m/s based on a *Re* = 200 is given. The exit boundary is defined by outlet pressure condition (zero-gauge pressure). The surface of the bluff body is also assumed as the no-slip wall boundary, and the flexible plate region is defined as the two-way fluid-structure interaction (FSI) boundary. In the case of FSI boundary, a continuous exchange of displacement quantity and fluid pressure *w.r.t.* the structural and flow domains are considered. The overall dimensions of the flow domain (*800D* × *600D*) have been decided after performing an initial domain convergence study.

The flow domain is discretized using a non-uniform structured grid configuration, as shown in Figure 3.2 (b). Unstructured grid arrangement is easily adjusted, and it is simple to use even with complicated models [102]. The grid refinement is mainly applied in the close vicinity of test geometry to visualize the flow pattern near the wall. A very fine mesh is used near the flexible plate, followed by a coarse grid structure away from the plate. Similarly, high density mesh configuration is adopted near the surface of the bluff body. To get a converged grid structure, numerous mesh structures are tested, and a converged one is eventually used for all the simulations.

3.1.1.4 Grid convergence study

To check grid independency of the computational flow domain, various levels of mesh refinement ranging from a coarse structure to a fine structure have been tested. Simulations are conducted for a model of a flexible plate with a square upstream bluff body at *Re*=200 flow condition. The tip deflection of the plate has been monitored as the convergence parameter.

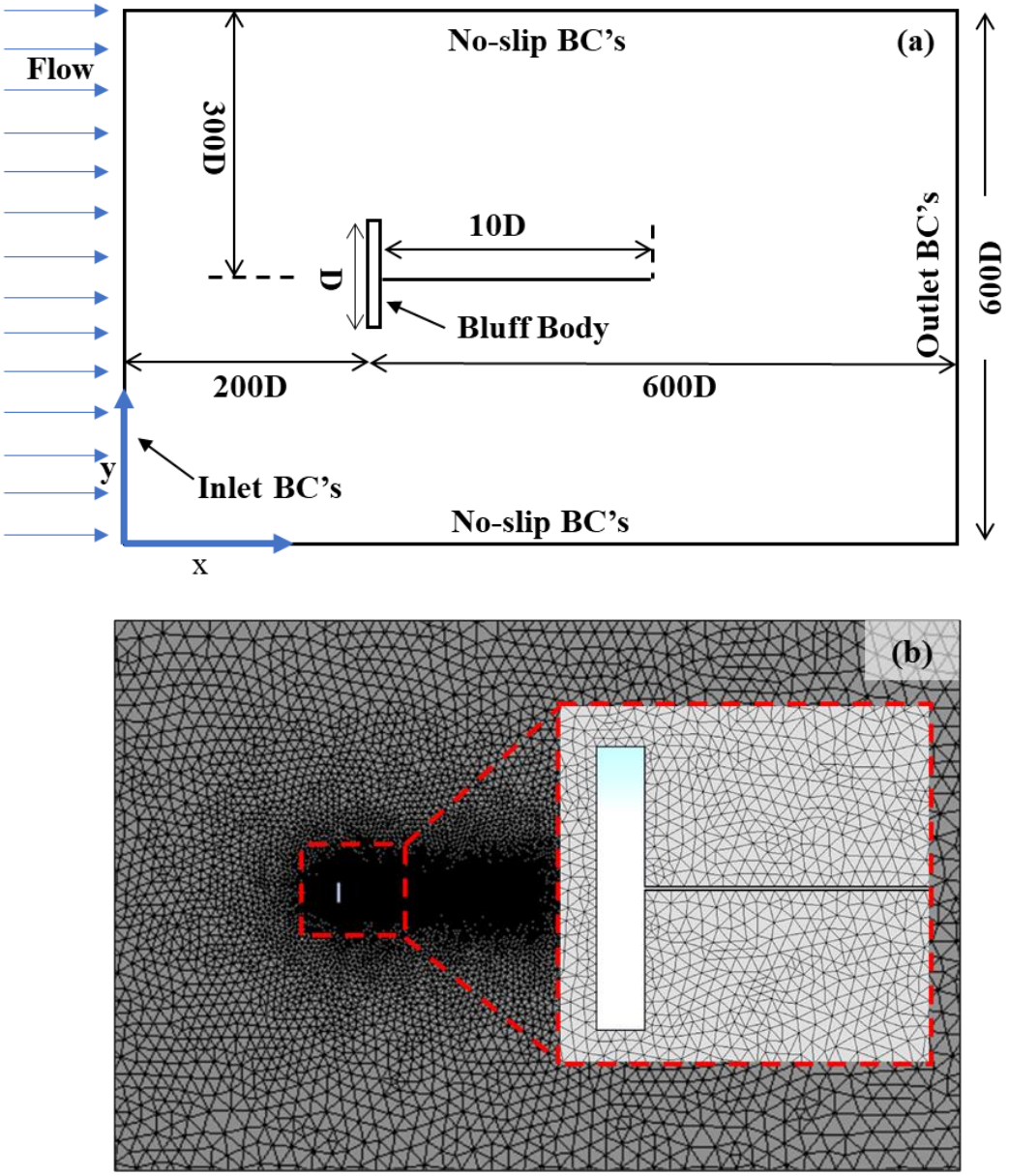

Figure 3.2: (a) Schematic of two-dimensional flow computation domain with boundary conditions, (figure not to scale), where D=0.05 m, (b) gird discretization around the test geometry

Table 3.1 shows the summary of grid convergence study. The table indicates that tip deflection increases as the element increase from 15470 to 21668 (level #4 in Table 3.1), and beyond that, a converged level of deflection of 0.145 m is achieved. Based on this, a converged grid structure of a total of 24120 elements (level #5 in Table 3.1) has been considered for all the simulations. Figure 3.3 shows the grid independency analysis by varying the grid elements.

Table 3.1: Summary of grid independent study

Level	Number of nodes in computational domain	Total number of elements	Tip Deflection in terms of size of bluff body (m)
#1	31328	15470	0.065
#2	36036	17796	0.086
#3	39734	19614	0.122
#4	43906	21668	0.145
#5	48924	24120	0.145
#6	54172	26684	0.145

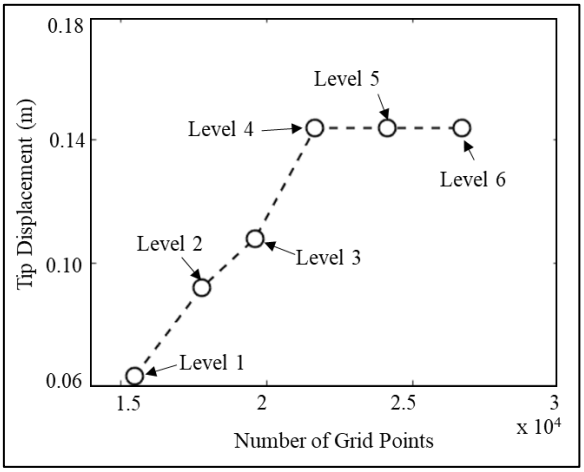

Figure 3.3: Grid independence analysis of tip displacement *vs* number of grid points

3.1.1.5 Domain and simulation time step sensitivity study

To evaluate the effect of size of the computational domain, three domain sizes are analyzed for the case of square bluff body with a trailing plate, detailed in Table 3.2. The results obtained indicate an equivalent tip deflection and a converged size of computational domain of 800D×600D (*D* is size of bluff body, 0.05 m) is considered for all the simulations. As the computational domain is very large than the size of the test model, wall boundary effect will be negligible.

Table 3.2: Domain Validation at *Re* = 200 at computational time step 0.001s

Domain Size	Number of elements	Tip Deflection (m)
1000Dx800D	27509	0.145
800Dx600D	24120	0.145
600Dx400D	22957	0.101

For time step sensitivity analysis, simulations are carried out for the reference case of a flat plate bluff body with trailing plate using a computational domain of 800D×600D at *Re* =200. Table 3.3 shows the tip deflection of the plate for different time steps. The results indicate that beyond the 0.0025s time step, the tip deflection value is converged, and corresponding mode shapes are also equivalent to the first bending mode of a cantilevered beam. Therefore, in the present study, a converged time step of 0.001s is considered for all the simulations

Table 3.3: Time-step validation at *Re* = 200

Time Step	Tip Deflection (m)	Dominating Mode Shape of vibration
0.01	Unstable solution	Mesh deformation error
0.005	0.105	1st bending mode
0.0025	0.145	1st bending mode
0.001	0.145	1st bending mode
0.0005	0.145	1st bending mode

3.1.2 Natural frequency of the plate

Before computing the flow-induced vibration response of the structure, modal analysis of the structure is carried out. This included the finding of the free vibration frequencies and corresponding mode shapes of the cantilever plate. Table 3.4 shows the summary of modal analysis of the plate where both deflection shapes and corresponding natural frequencies are listed.

Table 3.4: Summary of the modal analysis of the plate

First bending mode	3.27 Hz	
Second bending mode	20.47 Hz	
Third bending mode	32.62 Hz	

3.2 Vibration response of plate with a flat bluff body in flow

When the flow passes over the structure, it is observed that the fluid first interacts with the frontal body and forms two shear layers separated from the leading edge of the flat plate bluff body. As the flow advances, the shear layer extends and reattaches onto the surface of the trailing plate. Figure 3.4 (a-d) shows velocity distribution of the flow field, which indicates the beginning of separation of the shear layer and its reattachment on the trailing plate. The flow field is subjected to unsteady forces on the surface of the flexible plate; consequently, an oscillatory bending motion is induced in the trailing plate. Figure 3.5 (a-d) shows vorticity contours of the flow field at different time instances.

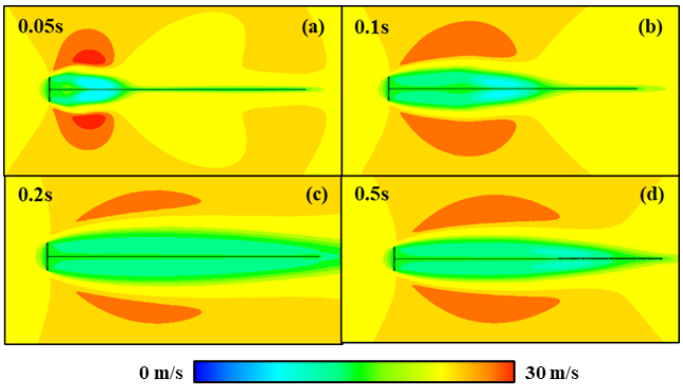

Figure 3.4: Velocity contours of the flow field around the vibrating plate plotted for flat bluff body with various time steps

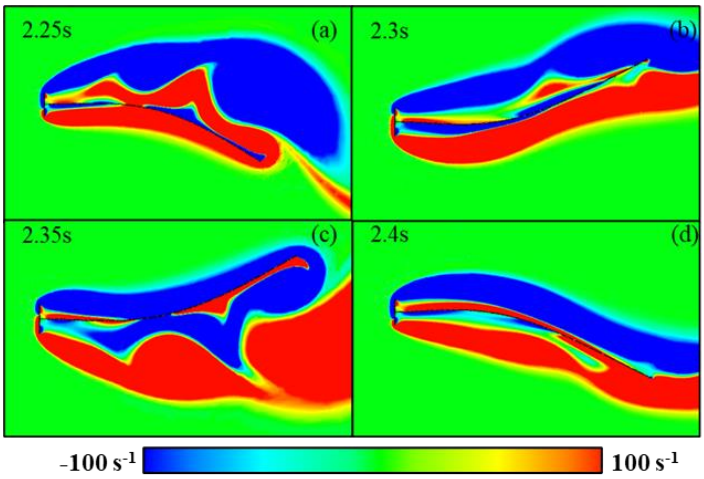

Figure 3.5: Vorticity contours of the flow field around the vibrating plate plotted for flat bluff body with various time steps

Figure 3.6 (a-c) shows time history, frequency spectrum of tip deflection of the plate, and superimposed image of deformation shapes of the cantilevered plate observed at different time steps, respectively. It is observed that the plate motion is close to the first bending mode of a cantilevered plate, and with the course of time the plate vibration grows and reaches a steady state level. The frequency spectrum (Figure 3.6 (b)) indicates that the dominant frequency of the vibration is 4.79 Hz, which is close to the first free vibration frequency of the plate 3.27 Hz (Table 3.4).

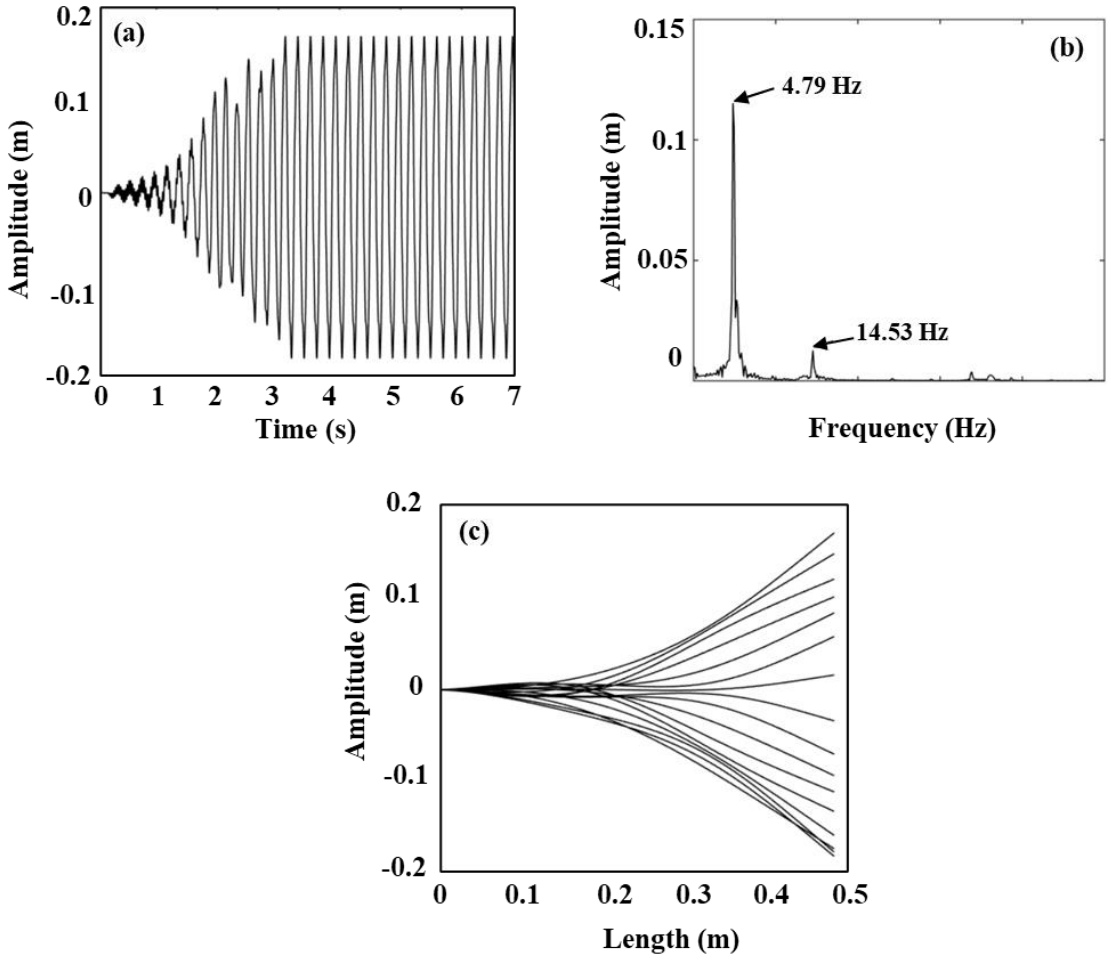

Figure 3.6: (a) Time history, (b) frequency spectrum, (c) superimposed images of tip deflection of the flexible plate with the flat bluff body

In addition to the dominant frequency component, higher harmonics are also presented in the frequency spectrum (14.53 Hz), which are probably presented due to periodicity in the measured tip deflection. As the structure has higher flexibility, large amplitude vibration is

taken place which is account considering geometrical nonlinearity in the simulation. The probable reason of odd harmonics is the half wave symmetry of the vibration of the tip deflection. It may be inferred that both flow vortex field and structure vibration are coupled and primarily dominated by the structure motion. The probable cause of this fact is further investigated in the next section.

3.3 Study with different shapes of upstream geometry

The foregoing analysis shows an initial study of flow-induced vibration of a plate in the vortex field from a simple upstream obstacle. Now, to understand the role of the shape of bluff body on FIV, different sections such as square, equilateral triangular, D-shape, and cylindrical shapes are considered. Figure 3.7 (a-d) shows the schematic diagram of the four test models. The purpose of selecting different shapes is to find out overall effect on various parameters such as mode shape, vibration frequency, the amplitude of vibration, etc. However, before performing the FSI computation, the Strouhal number of the combined geometry of plate with an upstream body is also computed to understand the relative influence of the structural and fluid domain on overall vibration characteristics under different wake conditions.

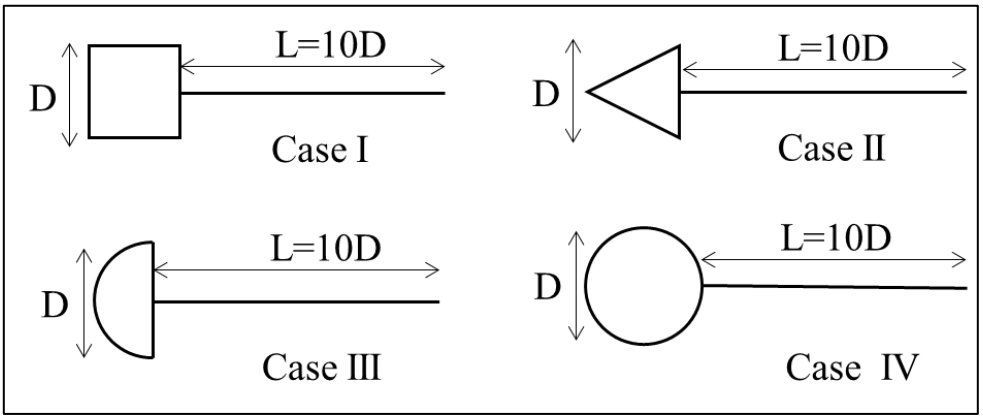

Figure 3.7: Geometry of test models (the figure is not to Scale), D = 0.05 m

3.3.1 Strouhal Number of the test geometries

As previous finding (Section 3.2) shows the dominance of structural natural frequency in the overall vibration of coupled fluid and structural domain; to check the coupling of vortex field

with the overall structural vibration, Strouhal number corresponding to different geometries is now investigated. The Strouhal Number ($St = f \times D/u$) represents the relation between the vortexes shedding frequency (f), flow velocity (u), and the size of the bluff body (D). Traditionally, St is calculated for the vortex shedding from a standalone rigid bluff body under different Reynolds numbers ($Re = \rho \times u \times D/\mu$) regime [24]. As the present test model is an assembly of a bluff body with a trailing structure, St is estimated for different shapes of bluff body with a trailing rigid plate. The Reynolds numbers are also varied up to 750.

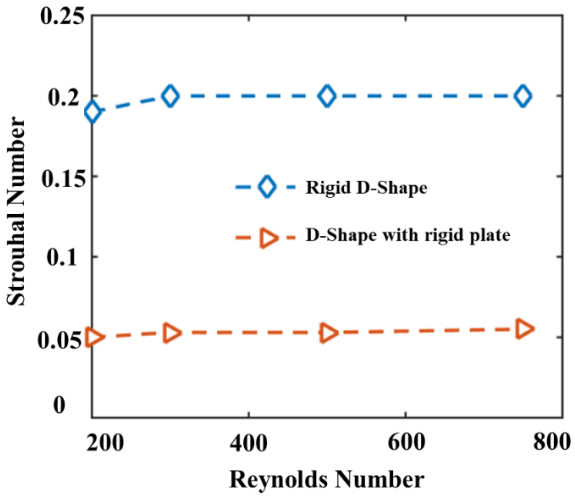

Figure 3.8: Reynolds number *vs* Strouhal number for the case of D-shape bluff body

All simulation is performed on the same computational domain as considered in the previous section, and only the front body is changed sequentially. Rest all parameters are kept as it is. For reference, an additional case of standalone bluff body is also included.

Figure 3.8 shows the Strouhal number of the two cases as flow over a single D-shape body and D-shape body with a 2D rigid trailing plate. The results obtained for the standalone D-shape objects ($St=0.19$ at $Re=200$) show a good match with the results obtained by Sivadas [23]. Contrary to this, the presence of a trailing plate changes the flow dynamics dramatically, and the Strouhal number reduces drastically from the range 0.2-0.3 (without a trailing plate) to 0.05 approximately. A probable reason for the reduction is the presence of a trailing plate that delays the vortex formation and reduces vortex shedding frequency. In the similar fashion, Strouhal

numbers for the other test section is calculated and summarizes in Figure 3.9. In all the cases, the *St* reduces on the order of one.

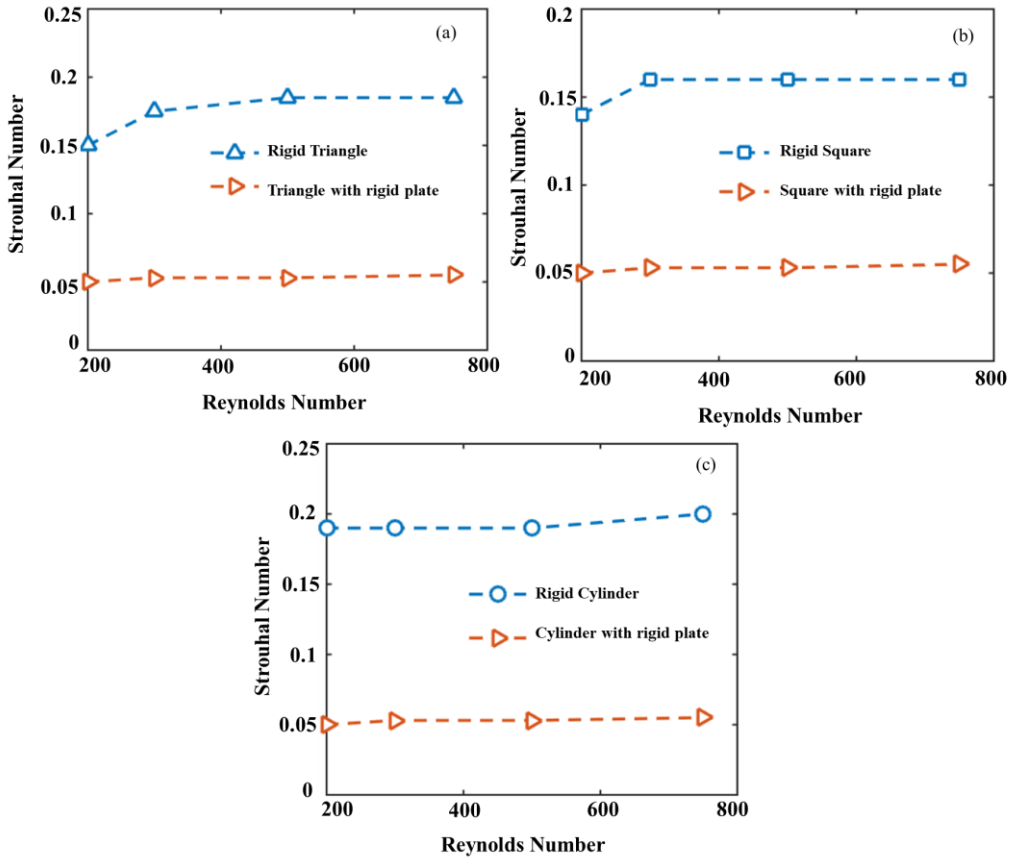

Figure 3.9: Reynolds number *vs* Strouhal number for the case of (a) triangle bluff body, (b) square bluff body, (c) cylindrical bluff body

3.3.2 Vibration response of the plate

3.3.2.1 Case I- Flow over the plate with square bluff body

Figure 3.10 (a-d) shows velocity distribution of the flow field, which indicates the beginning of separation of the shear layer and its reattachment on the trailing plate. The flow field was subjected unsteady forces on the surface of the flexible plate and consequently, an oscillatory bending motion induced in the trailing plate. Figure 3.11 (a-d) shows vorticity contours of the flow field at different time instances. Figure 3.12 (a-c) depicts time history, frequency spectrum of tip deflection of the plate, and a superimposed image of deformation shapes of the cantilevered plate observed at different time steps, respectively. It is observed that the plate

motion is close to the first bending mode of a cantilevered plate, and with the course of time the plate vibration grows and reaches a steady state level. The frequency spectrum (Figure 3.12 (b)) indicates that the dominant frequency of the vibration is 4.35 Hz, which is close to first free vibration frequency of the plate 3.27 Hz (Table 3.4). In addition, higher harmonics are also observed (15.88 Hz). It may be inferred that both flow vortex field and structure vibration are coupled and primarily dominated by the structure motion.

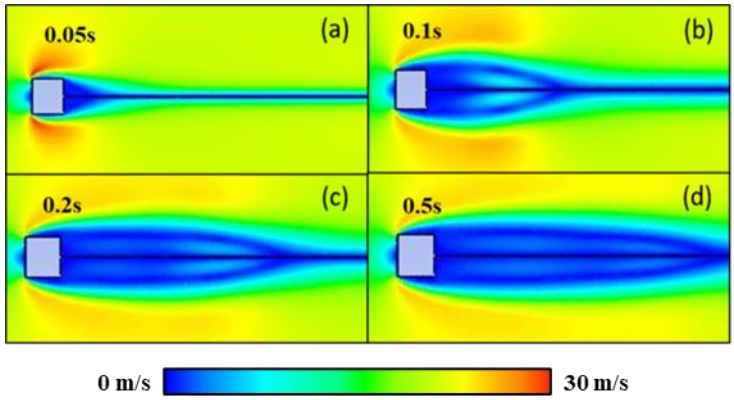

Figure 3.10: Velocity contours of the flow field around the flexible plate plotted for square bluff body at different time instances

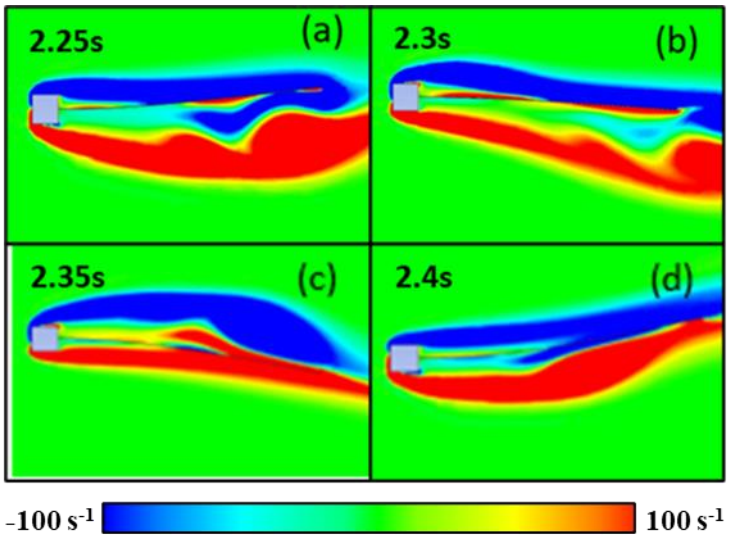

Figure 3.11: Vorticity contours of the flow field around the flexible plate plotted for square bluff body at different time instances

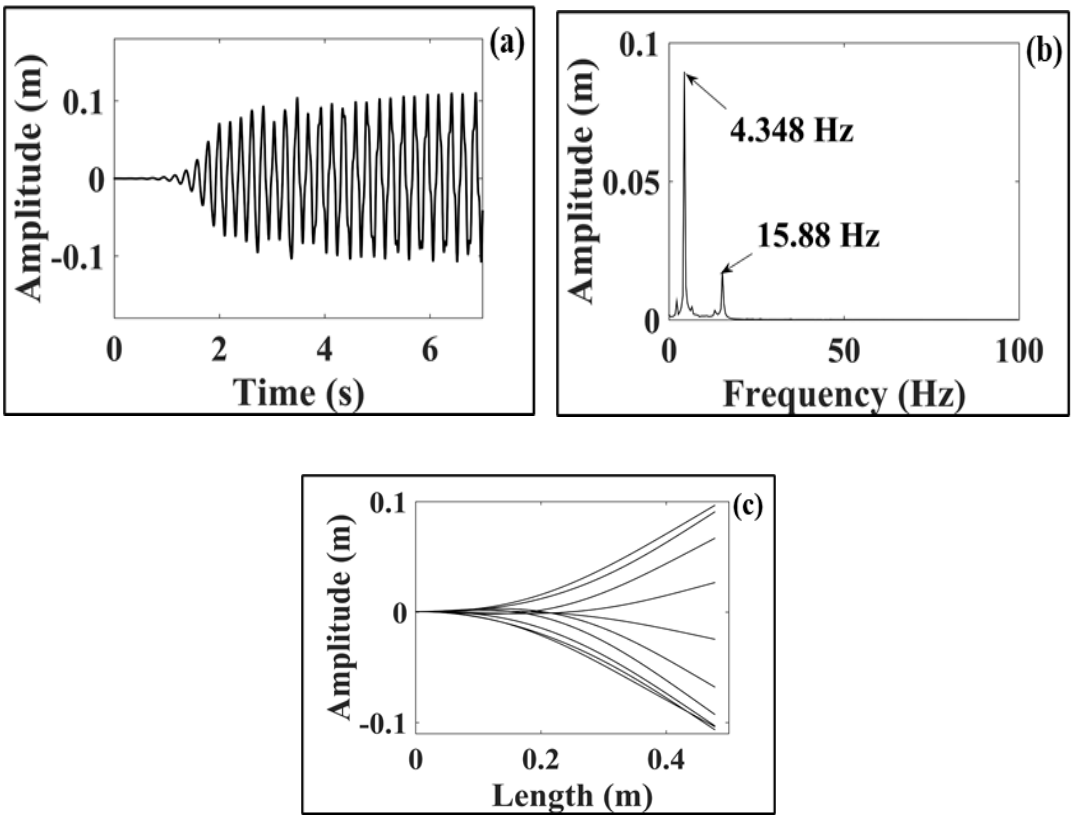

Figure 3.12: (a) Time history, (b) frequency spectrum, (c) superimposed image of tip deflection of the flexible plate with the square bluff body

3.3.2.2 Case II- Flow over the plate with D-shape bluff body

In the case of flow with D-shape frontal bluff body, the initiation of flow is similar to observed in the case of flow with square bluff body. The shear layers get separated after striking the front face of bluff body as shown in Figure 3.13 (a-d), extend on the downstream side, and are reattached to the surface of the plate. Figure 3.14 (a-f) depicts the vorticity contours and position of the oscillation plate with respect to time. The figures show the oscillating motion of plate and corresponding vortex shedding from the trailing edge of the plate. Figure 3.15 (a-c) shows time history, frequency spectrum, and superimposed image of tip deflection, respectively. The plate vibration increases with the passage of time and reaches a steady state level. Figure 3.15 (c) represents the superimposed image of vibrating shapes of the cantilever plate at various time instances. The figure shows that the motion of the plate is a combination of fundamental and higher bending modes. The frequency spectrum shows a dominating

frequency of 4.03 Hz. In addition, odd harmonics of the first dominating frequency are also noted, which may be presented due to periodicity in the motion of the plate. From the frequency spectrum, it is noted that the fifth harmonic of the first frequency component (5×4.03 Hz) and the second modal frequency (20.57 Hz, Table 3.4) are close enough and presented together in the spectrum.

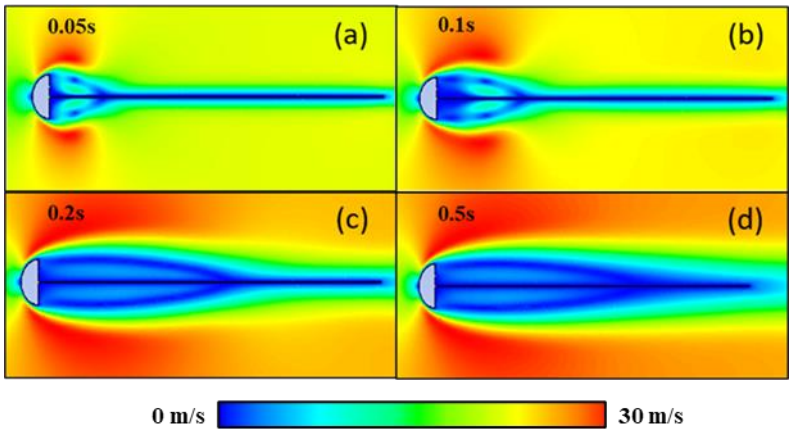

Figure 3.13: (a-d) Velocity contours of the flow field around the flexible plate plotted for D-shape bluff body at different time instances

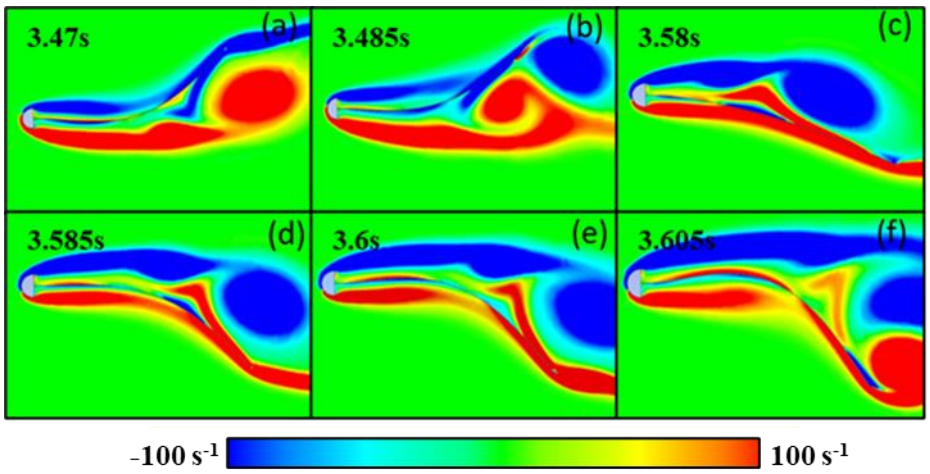

Figure 3.14: (a-f) Vorticity contours of the flow field around the flexible plate plotted for D-shape bluff body at different time instances

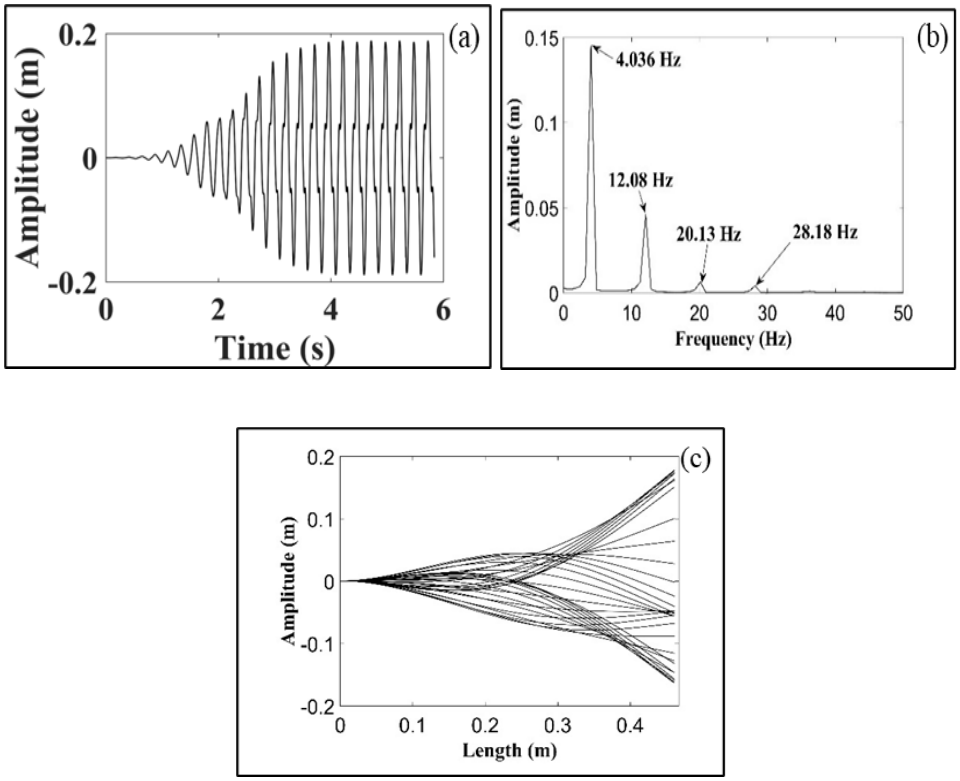

Figure 3.15: (a) Time history, (b) frequency spectrum, (c) superimposed image of tip deflection of the flexible plate with the D-shape bluff body

3.3.2.3 Case III- Flow over the plate with triangular bluff body

Figures 3.16 and 3.17 show velocity contours around the test geometry and vorticity contours of the flow field, respectively. The qualitative inspection of the flow field indicates a similar characteristic as observed in the case of flow with a square body and D-shape body.

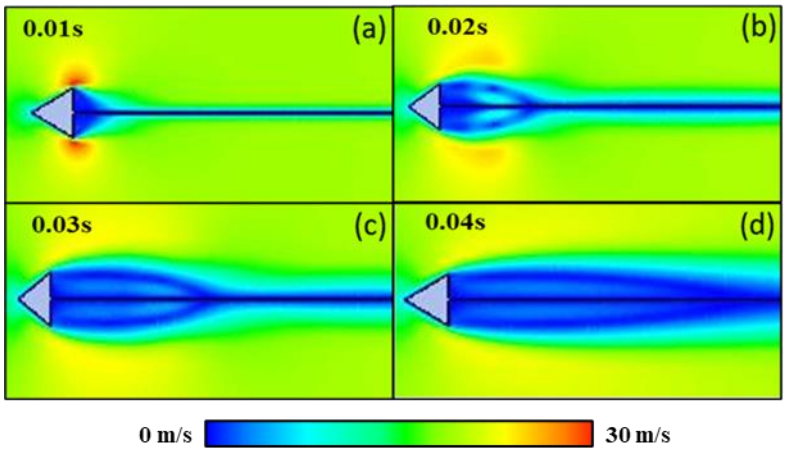

Figure 3.16: (a-d) Velocity contours of the flow field around the flexible plate plotted for triangular bluff body at different time instances

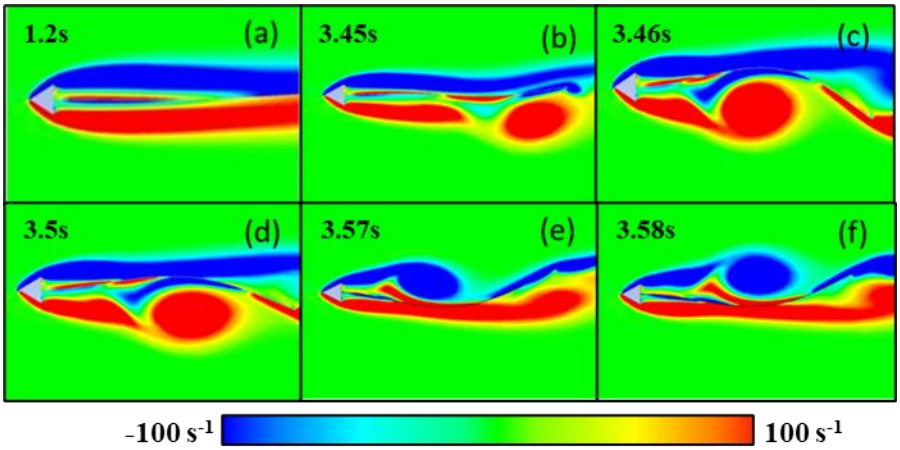

Figure 3.17: (a-f) Vorticity contours of the flow field around the flexible plate plotted for triangular bluff body at different time instances

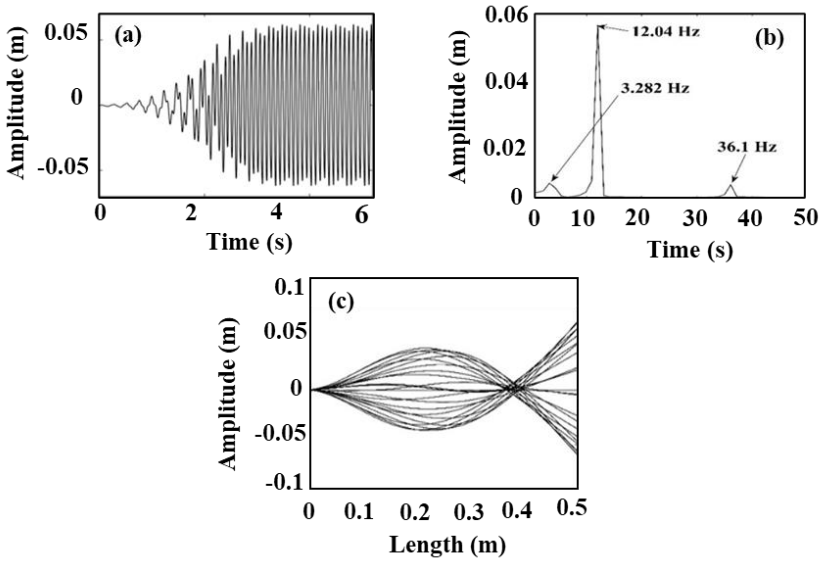

Figure 3.18: (a) Time history, (b) frequency spectrum, (c) superimposed image of tip deflection of the flexible plate with the triangular bluff body

3.3.2.4 Case IV- Flow over the plate with cylinder bluff body

Figures 3.19 and 3.20 show velocity contours around the test geometry and vorticity contours of the flow field, respectively. Figure 3.21 (a-c) shows the time history, frequency spectrum, and superimposed image of plate deformation with time for the cylindrical obstacle. The spectrum indicates a mixed mode oscillation (Figure 3.21 (c)); however, the first bending mode is dominating.

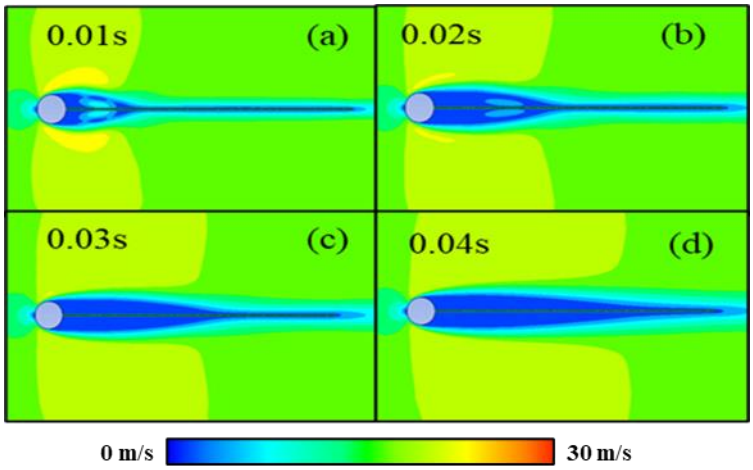

Figure 3.19: (a-d) Velocity contours of the flow field around the flexible plate plotted for cylinder bluff body at different time instances

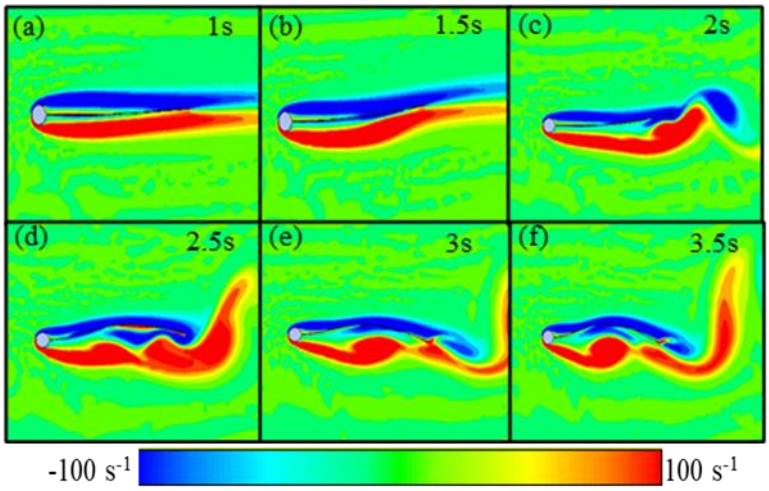

Figure 3.20: (a-f) Vorticity contours of the flow field around the flexible plate plotted for cylinder bluff body at different time instances

From the aforementioned details, it may be inferred that the shape of bluff body has a marked influence on the vibration characteristics of the flexible plate. In all the cases, deflection shape of the plate is found to be different. It is noted that the vibration level induced by the D-shape body is larger than in the other three cases. The probable reason for variation in the deflection shape may be extracted from understanding the flow field around the structure.

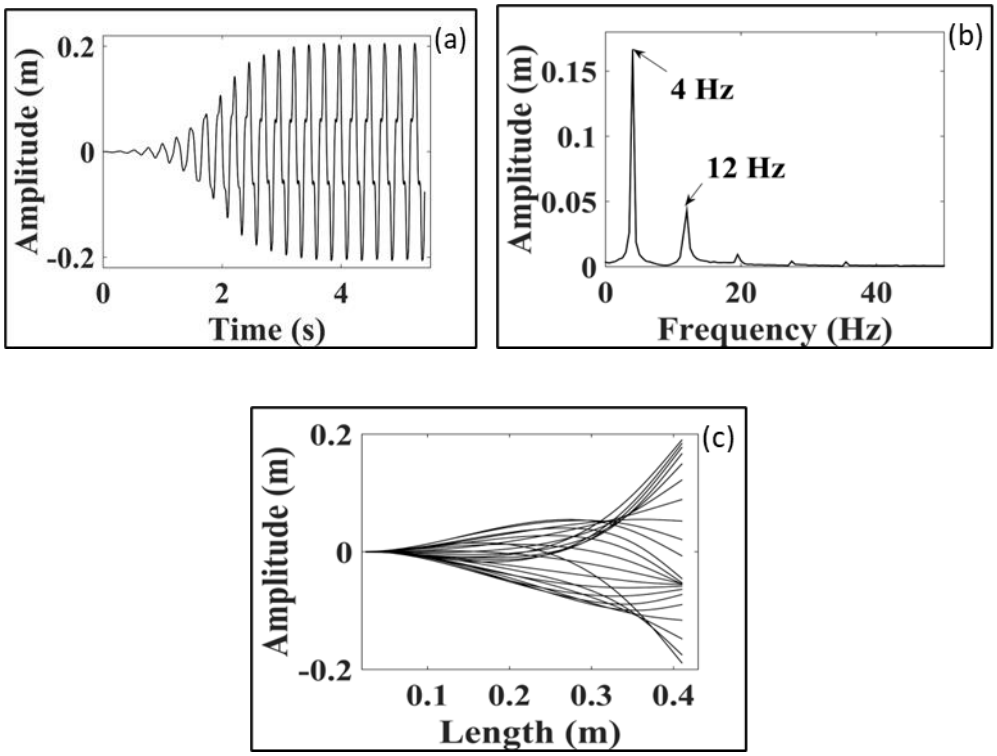

Figure 3.21: (a) Time history, (b) frequency spectrum, (c) superimposed image of tip deflection of the flexible plate with the cylindrical bluff body

A systematic observation reveals that the position of reattachment point of the extended shear layer on the trailing plate is different corresponding to different bluff bodies. In the case of square body, the reattachment location is towards downstream side from the free end of the plate. Although, in the cases of triangle, circular and D-shape bodies, the position of reattachment point is on the plate towards the fixed end of the plate. Qualitatively, the location of their reattachment point is close to each other. It is expected that the distributive loading over the trailing plate is governed by the location of reattachment of a shear layer that is eventually responsible for the deformation of the shape of an oscillating plate.

Figure 3.22 (e-p) shows instantaneous pressure contours around the trailing plate for all four cases. In addition, for the comparison, the superimposed image of deformation pattern of plate is also attached. The contours are plotted for initial time instances while the plate oscillations have been building up. From the pressure contours, it can be noted that the pressure loading changes from positive to negative values (gauge pressure) on both sides (top and bottom) of

the plate, which may be primarily responsible for the resultant deflection shape of the flexible plate.

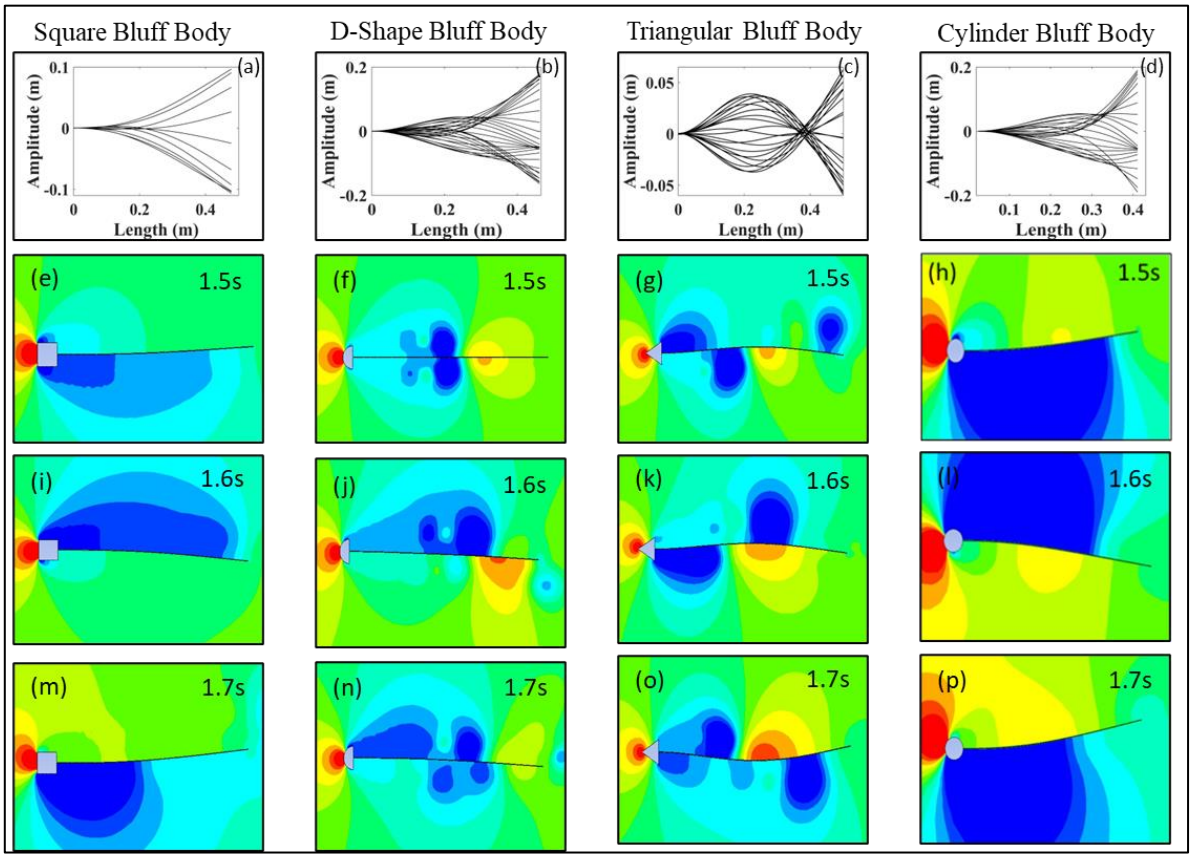

Figure 3.22: (a- d) Superimposed images of plate deflection, pressure contours of flow field corresponding to different bluff bodies, (e, i, and m) for square section, (f, j, and n) for D-section, (g, k, and o) for triangle section, and (h, l, and p) for cylindrical section

In the case of triangle and D-shape bodies (Figure 3.22 (g, k, and o) and (f, j, and n)), the level of pressure across the plate varies along the length. On the other hand, in the case of a square bluff body, the pressure field is of identical nature for two-third length of the plate approximately. In the case of cylinder, a similar pressure field is observed; however, the influence of second bending mode is also noted. Hence, the pressure field can be considered as an equivalent loading over the plate. It can be assumed that a uniform loading over a span of 2/3rd length of the plate causes a fundamental mode of vibration. Conversely to this, frequent variation of loading across the thickness may induce higher modes (Figure 3.22 (a-d)).

In order to correlate the lock-in of vortex shedding and structural oscillation, the Strouhal number of each test model with respect to the frequency of oscillation is calculated. Table 3.5 shows the summary of *St* corresponding to four reference models as standalone rigid body, body with a rigid trailing plate, and with a flexible trailing plate is calculated. Understanding the table reveals interesting facts. The vibration frequency is neither dominated by the vortex shedding of a standalone bluff body nor by the bluff body with a rigid trailing plate. The coupled dynamics of fluid and structure are found to be governed by the structure's natural frequency. The outcome indicates strong synchronization of flow domain with the structure oscillation.

Table 3.5 Summary of *St* corresponding to four reference models

Shape of bluff body	Rigid Bluff body	Rigid Bluff body with rigid plate	*St* based on natural frequency of flexible plate	
			1st Mode	2nd Mode
Square	0.14	0.05	0.0072	0.026
D- shape	0.19	0.05	0.0067	0.020
Triangle	0.14	0.05	0.0054	0.020
Cylinder	0.19	0.05	0.0067	0.020

3.4 Strain distribution and charge generation from vibration

This section discusses the energy harnessing potential of the flexible structure when piezoelectric transduction is employed. For the simplicity of the calculation, it is assumed that a plan structure along with the piezoelectric layer will show equivalent oscillation characteristics as obtained for plane structure, and the aspect of electro-mechanical coupling is also ignored. As the amount of energy yield depends on the level of strain generated in the material, the focus is primarily given to estimate the strain distribution responsible for the

generation of electric charge. The linear piezoelectric constitutive equation (PZT equation) shows the yield of charge per unit area as [103]

$$D_z = d_{13} E \varepsilon_x + \vartheta_{33} V_z \tag{3.5}$$

$$Q = \int D_z ds \tag{3.6}$$

where d_{13} is dielectric constant, subscript 13 indicates the charge generation along the axial direction. E is elastic constant, ε_x is strain in the axial direction, υ_{33} is dielectric constant and is the electric field across the thickness of the plate. The total charge can be obtained by integrating the charge/unit area shown in Equation (3.6). In the absence of an external electric field across the thickness, the charge generation solely depends on the term $d_{13} E \varepsilon_x$. Which clearly indicates the proportionality of charge with the induced strain. Owning this fact, in the present study, strain distribution over the structure is primarily used as the measurement of piezoelectric power yield, and comparisons are performed. The axial strain (ε_x) is computed by equation 3.7

$$\varepsilon_x = z \frac{\partial^2 w}{\partial x^2} \tag{3.7}$$

where z represents the coordinate of a layer along with thickness with respect to the neutral plane. Deflection is defined by *w*, and *x* represents the length dimension of the beam. From our analysis, it is observed that the level of tip deflection is highest for D-shape bluff body and lowest for square body. Although, the mode shape of vibration in all four cases is different. Therefore, unless the level of strain distribution is investigated, it is difficult to compare the energy harvesting among the four cases. Figure 3.23 (e-l) shows the instantaneous strain distribution and RMS strain distribution along the length of the plate. For reference, deflection shapes are also depicted in Figure 3.23 (a-d).

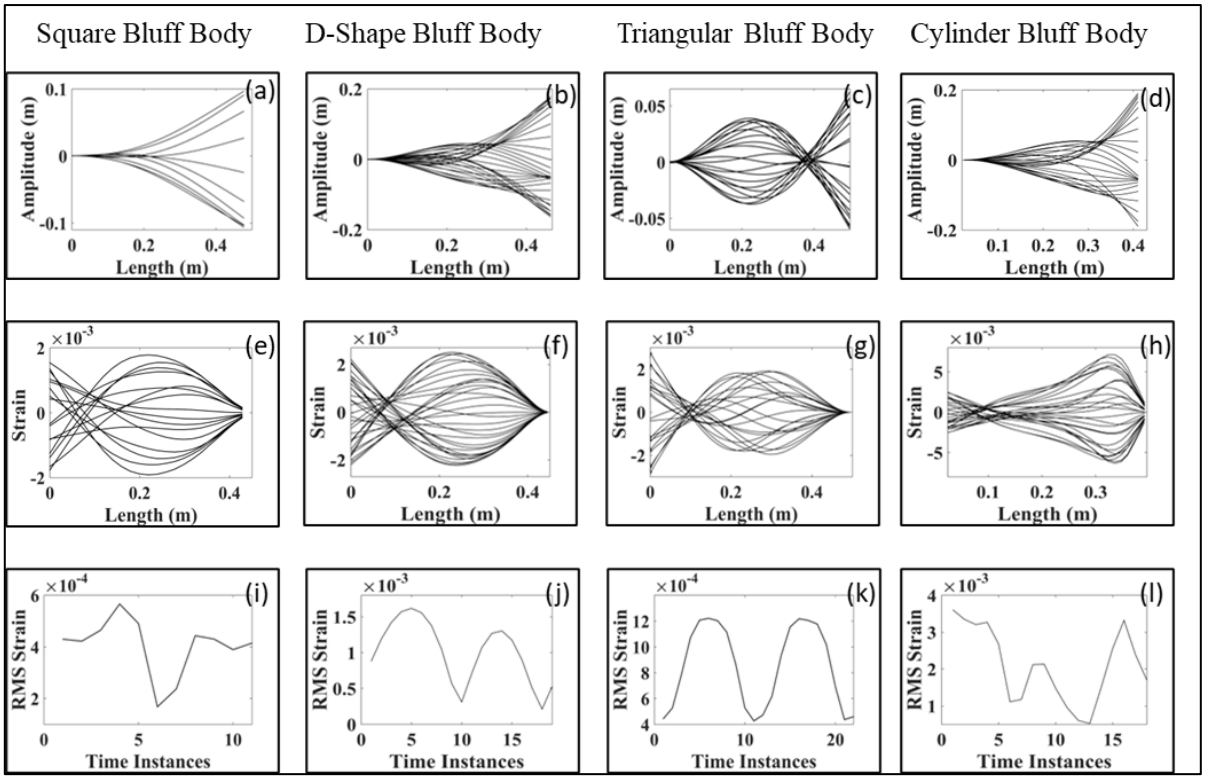

Figure 3.23: (a-d) Superimposed images of tip deflection, (e-h) strain distribution over the plate, and (i-l) RMS strain of the plate in case of square, D-shape, triangle, and cylinder, respectively

From the instantaneous strain distribution (Figure 3.23 (e-h)), it is noted that in the case of a square body, the strain level reduces as it moves from fixed to free end, that is expected since the structure is oscillating in the first bending mode of the cantilevered plate which causes high strain at the root of the plate. However, in the case of D-shape, the strain shows two maxims, strain level is higher at the root and, as moved from fixed to free end (Figure 3.23 (f)), it shows a second maximum at mid-length (approximately) of the plate. A similar strain characteristic has been observed in the triangle section (Figure 3.23 (g)); however, the second maximum is noted at 0.7*L* away from the fixed end. In the case of a cylindrical body, a sharp variation in the strain is observed. For a small length, a very high strain level is noted. Quantitative comparison of the maximum strain shows (Table 3.6, column 4) that cylinder and square bluff bodies induce maximum and minimum strain, respectively. The level of maximum strain at a point generated by D-shaped body is approximately 20% less than the generated by the triangle

body. It may be noted that analysis of maximum strain gives an idea of an instantaneous level of peak strain. However, for energy harnessing using a layer of piezoelectric material over the entire length of the plate, the cumulative strain is responsible. Therefore, it is more appropriate to analyze cumulative strain level than maximum strain. Hence, cumulative root mean square (RMS) strain is also calculated by considering 200 discrete points over the plate and integrating it for one cycle of oscillation. In addition, to see the effect of frequency of the vibration on the overall charge generation, charge per second is also calculated by using the equation (3.7). Surprisingly, it is observed that cylindrical object has maximum cumulative RMS strain; however, in the case of charge per second (calculated based on cumulative RMS strain), D-shape shows maximum generation. Figure 3.23 (i-l) shows a variation of cumulative RMS strain with respect to time. Table 3.6 summarizes results corresponding to strain calculated in the four cases.

Table 3.6 Strain level and charge generation for different cases

Shape	Max deflection (m)	Dominating bending mode	Maximum strain	Cumulative RMS strain (maximum)	Average Charge (Q/D_z) (Per second)
Square	0.1076	First	0.000693	0.000566	0.0015
Triangle	0.06274	Mixed	0.002817	0.001375	0.0038
D-shape	0.1778	Mixed	0.002414	0.001613	0.0042
Cylinder	0.1875	Mixed	0.004031	0.001553	0.004

The present analysis is also useful to find optimum placement of piezoelectric material in case of partial layering of piezoelectric patches than covering the entire length. To find the optimum location, the entire length of the plate is divided into five zones, and equivalent average strain corresponding to each zone has been calculated. Figure 3.24 shows the level of strain calculated for all four cases. It is observed that, at all the locations, the level of strain corresponding to square body is relatively very low. In the middle length, both triangle and D-shape sections

have equivalent strain distribution. In the case of cylindrical body, a higher strain is noted at the 3/4th length of the beam from the fixed end. At the root zone, D- shape case shows higher strain than the case of triangle body, which is reversed for the tip zone area.

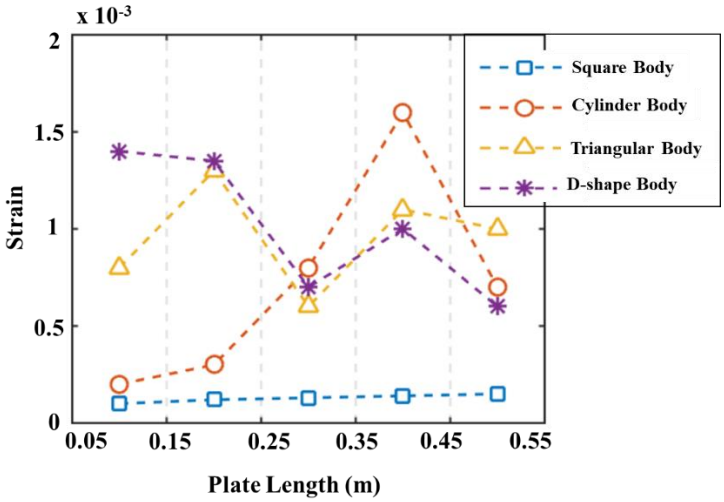

Figure 3.24: Strain level over the plate length

3.5 Effect of flow velocity on vibration

The aforementioned investigations revealed notable effect of geometry of the upstream body; however, to see the effect of flow velocity (Reynolds number) on vibration characteristics, additional simulations are performed for velocity ranging from 15 m/s to 50 m/s (Reynolds number ranging from 100 to 333). In all the cases, the flow field indicates the excitation mechanism is due to circulation passing over the surface and inducing motion. It is observed that the plate motion is close to the first bending mode of a cantilevered plate, however, the presence of higher mode is also experienced. Table 3.7 shows the relative tip displacement, dominant frequency of the vibration at different flow velocities. Figure 3.25 shows the graphical presentation of oscillation frequency and tip displacement for various flow velocities. It is found that with increase in the flow velocity, the vibration amplitude increases while flow increases from 15 to 30 m/s and then remains comparable up to 35 m/s flow speed. Beyond 35 m/s flow, the amplitude again reduces. The dominant frequency of the vibration is increasing

with increase in the flow velocity but remained in the close vicinity of the first free modal frequency of the sheet 3.27 Hz.

Table 3.7: Summary of tip deflections, frequencies at different flow velocities

Flow Velocity (m/s)	Tip Deflection (m)	Frequency (Hz)
15	0.045	2.01
20	0.06	3.04
25	0.09	3.47
30	0.10	4.38
35	0.095	4.68
40	0.085	4.82
45	0.08	5.18
50	0.075	5.43

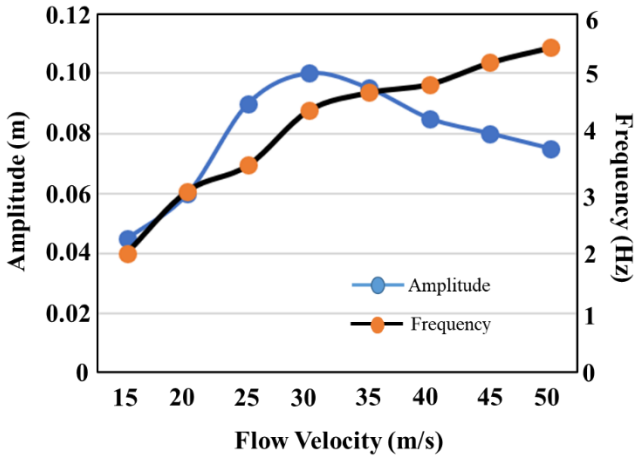

Figure 3.25: Variation of oscillation frequency and amplitude *w.r.t.* various flow velocities

3.6 Flow-induced vibration with air as flow medium

Results of the previous section show that the shape of the upstream body influences the nature of vibration significantly and so the amount of charge generated from the system. The D-shape upstream body causes higher bending mode vibration and corresponding higher charge generation. Since the previous computational study is carried out considering a low Reynolds

number environment, to reassure the concept build and for the final experimental verification, a further short study with air as the flow medium is carried out. As the present interest is to visualize the flow distribution over the trailing structure just before the flutter arrives, it is assumed that knowing the flow field around the rigid trailing structure will be useful to interpret the findings of the study. A rigid test geometry consists of a 2D plate with different bluff bodies considered, and the flow field is visualised thoroughly. Air is considered as a flow medium. Figure 3.26 (a) shows the schematic of the 2D computational domain along with the test model and different boundary conditions.

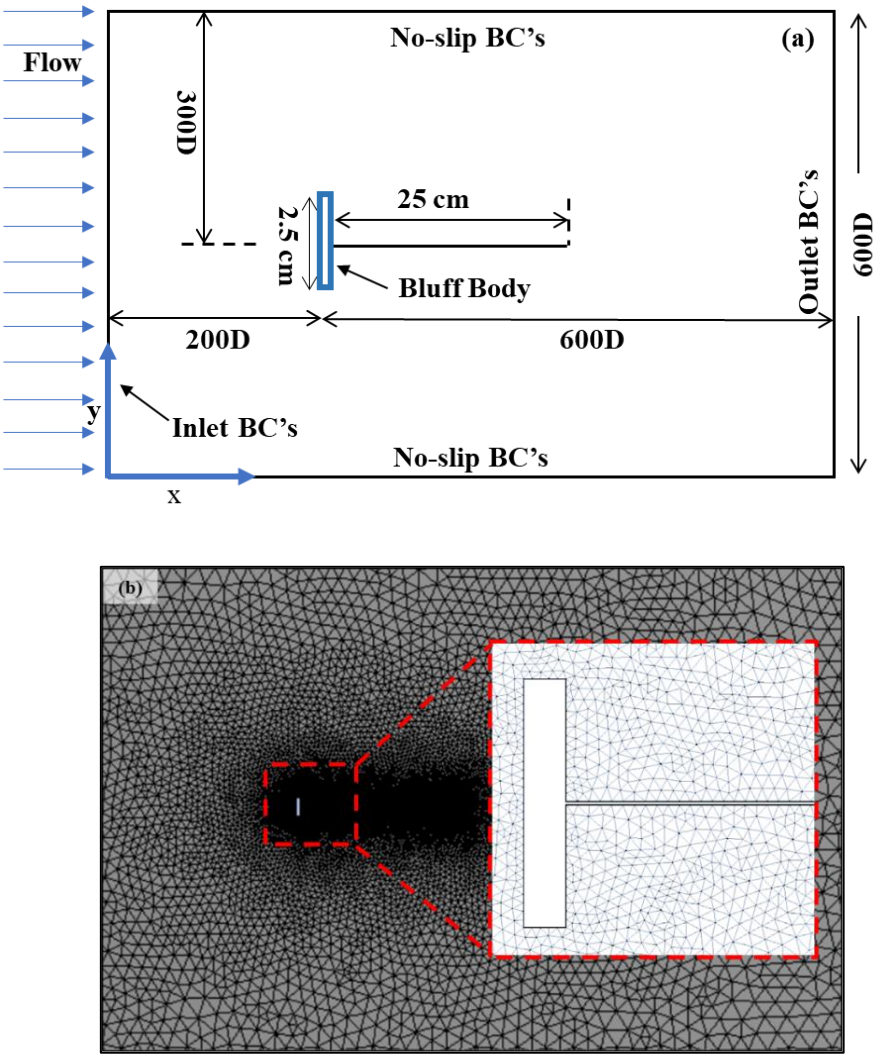

Figure 3.26: (a) Schematic of computational domain, (b) computational mesh for the rigid plate with flat bluff body

The simulations are performed on a two dimensional domain using RANS equation in commercial ANSYS Workbench [104]. It may be noted that in this study, flow velocity of 5 m/s is considered for all the simulations. The value of velocity and the dimension of the test model is selected based on some pre testing in the wind tunnel section. It is learned that actual flexible structure is not perfectly plane and when mounted in the test section, twisting took place. The amount of twisting further increases with the length of the structure. Therefore, after sufficient number of trials, a L/D = 10 ratio is selected.

Similarly, after a few tests run in the wind tunnel, it is observed that the structural instability occurs at around 5 m/s, and hence the same is considered for the simulations. The same model checked in simulation is later used in the experimental study. For discretization, a fine unstructured mesh with higher density close to the test model is considered. Before actual simulation, pre simulations are performed to check the mesh convergence and time step convergence and based on the results obtained, a converged mesh of 153234 elements with 163458 nodes and a converged time step of 0.001 seconds is considered, as shown in Figure 3.26 (b).

The flow field visualization shows that, as the flow passes over the body, shear layers separate and form circulation over the trailing plate. Figure 3.27(a-b) shows a close view of the flow distribution over the plane with a flat obstacle and D-shape body, respectively. It is observed that after initial fluctuation, the circulation zone attains a steady state configuration and imposes negative pressure distribution on both the sides (top and bottom) of the plate. The effect of circulation zone can be assumed to be equivalent to the instability generated during transverse galloping mechanism. It may be concluded that under the influence of the mixed excitation by the wake circulation and by the attached flow, the plate experiences flutter at a relatively lower critical velocity. Moreover, the size of the circulation is a direct consequence

of size of the obstacle and so the magnitude of the negative pressure, which eventually causes a higher drop in the threshold velocity.

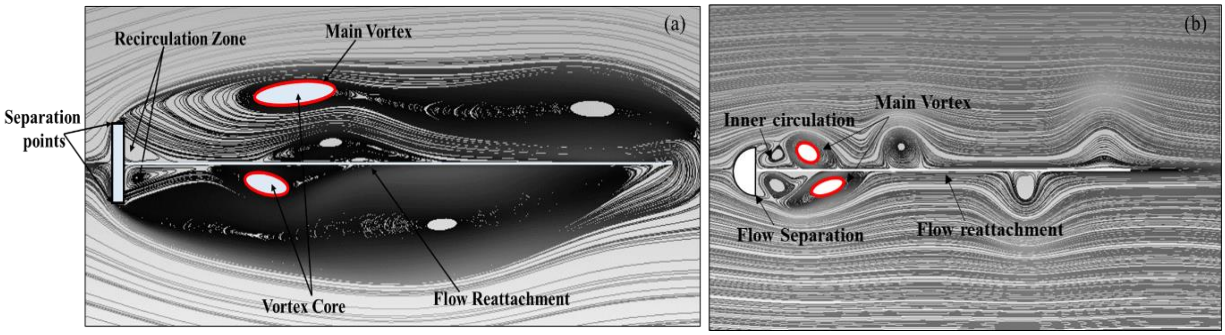

Figure 3.27: Streamline contours with circulation zone (a) flat obstacle, (b) D-shape bluff body

Figure 3.28 illustrates the vorticity and streamline patterns observed during flow over a model plate with various geometries, including flat, triangular, square, D-shaped, and cylindrical bluff bodies, at different flow velocities. In all the cases, the pressure distribution along the length varies due to the vortex field, which changes based on the different geometries. The results obtained from a similar system with a flexible trailing structure provide important conclusions regarding the onset of flutter. For an equivalent input flow condition, the flow distribution over the plate differs in terms of pressure distribution, location of the reattachment point of the shear layer, expansion of the shear layer in the cross-flow direction, and distribution of vortices on the top and bottom sides of the structure, as shown in figure 3.28 (a-a1, e-e1, i-i1, m-m1, and q-q1).

Figure 3.28 (i1) shows inner circulation forms in the near wake region after the flow separates from the leading edge of the bluff body. The recirculation bubble then shrinks and adheres to the rear wall of the bluff body. Initially, the circulation zone experiences some fluctuations, but eventually reaches a steady-state configuration and imposes negative pressure distribution on both the top and bottom sides of the sheet.

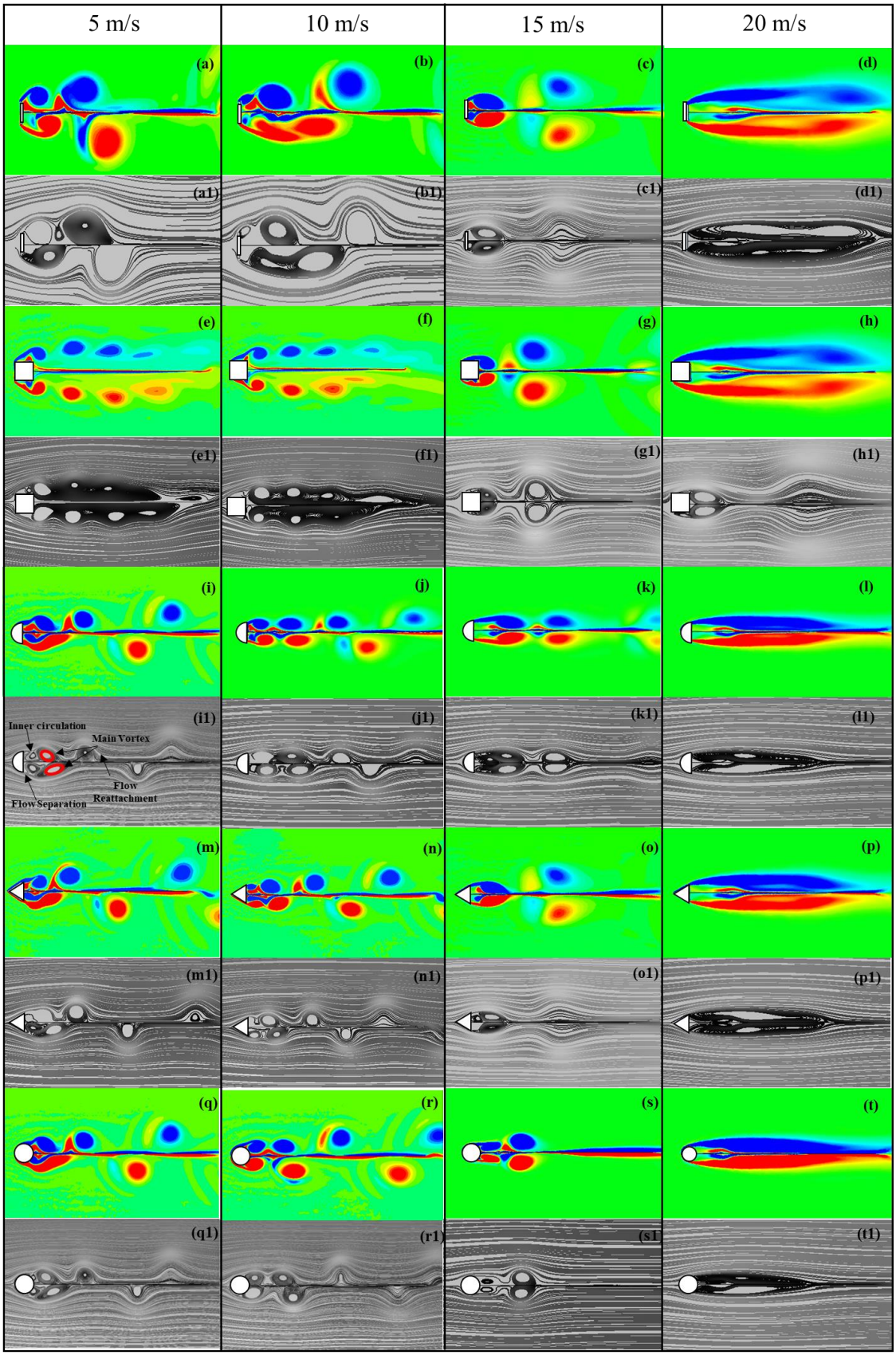

Figure 3.28: Vorticity contours and streamline contours plotted for different cases at different flow velocity at 2s

In the case of conventional flutter, the flow remains attached to the surface of a flexible structure and is typically triggered by perturbations originating at the tip region. However, for triangle, cylindrical, and D-shaped bodies, the vorticity pattern is alternate in nature, as depicted in Figure 3.28 (i-j, m-n, q-r). On the other hand, for flat plates and square bodies, the vorticity pattern is symmetric with respect to the top and bottom sides of the plate, as shown in Figure 3.28 (a-b, e-f).

3.7 Summary

3.7.1 Low Reynolds number flow study

- In this chapter, the numerical investigation of flow-driven vibration of a flexible plate with an upstream bluff body is carried out. The prime objective of this work is to identify the role of shape of a bluff body in the generation of different mode shapes of a flexible plate and then to correlate the oscillation with the corresponding piezoelectric energy harnessing. A two-dimensional low Reynolds number flow is considered, and four different shapes of the bluff body viz., square, equilateral triangle, cylinder, and D-section are tested. To get optimum grid configuration, a grid convergence study is also performed. In addition to the study of vibration characteristics, flow field around the plate is also investigated by analyzing flow velocity, vorticity, and pressure contours.
- The results obtained indicate that for a given flow velocity, the nature of vibration is not similar in all the cases, and different vibration frequency and mode shapes are observed. The square section induced fundamental mode vibration of the plate, whereas, in the case of a D-shape, circular, and triangular section, a mix of fundamental and higher bending modes are noted. Analysis of flow regime illustrates that the location of reattachment of the shear layers plays a crucial role in the generation of different modes. Pressure loading over the plate explained by the pressure contours

indicates different distribution that forces the plate to form different deflection shapes. The strain induced in the plate is measured to comment on the aspect of piezoelectric energy harnessing. The calculated strain distribution indicates that the plate with a square section showed the lowest level of strain (0.000693), and the circular section showed the highest level of strain (0.004031). However, the cumulative RMS strain measured over the entire length is highest in the case of D-section (0.001613) and lowest for the square section (0.0005663). The strain level is directly proportional to the power harnessing from a piezoelectric layer. Thus, it may be concluded that for a given flow condition, application of D-section bluff body will give rise to higher power yield by inducing higher bending mode oscillations.

3.7.2 High Reynolds number flow study

- It is noted that in a conventional flutter, the flow remains attached to the surface of flexible structure and is generally triggered by the perturbation that originated at the tip region. Manela and Howe [52] reported that flag pole vortex field alters the critical velocity of flutter. Hence, from the present simulation, it is interpreted that variable pressure distribution is responsible early flutter than observed in the traditional flutter of plane structure.
- From the perspective of variation in flow distribution corresponding to shape of upstream body, flow distribution highlights interesting facts. In the case of flat plate and square body, the vorticity pattern is symmetric with respect to top and bottom side of the plate, as shown in Figure 3.28 (a-h). Whereas, in the case of a triangle, cylinder, and D-shape body, it is alternative in nature, as depicted in Figure 3.28 (i-t).
- A similar field is observed in the case of a flat obstacle, which is expected as in both the cases the slow separates from a similar type of leading edge configuration. In the case of D-shape upstream body, vortex is distributed in an alternate manner. If we

correlate the pressure distribution over a cantilever structure and the mode generated in structure, alternate distribution will be more responsible for the generation of a higher bending mode than the symmetric distribution.

- The observation supports the findings of the previous study at low Reynolds number conditions and indicates that the wake field from a D-shape bluff body study may create higher bending mode vibration.

Further verification related to flutter arrival in the presence of different wake fields is investigated in the experimental study in wind tunnel environment.

CHAPTER 4

EXPERIMENTAL INVESTIGATION OF FLUTTER OF A CANTILEVER PLATE

The flow-induced vibration of a cantilever structure in flow has been numerically investigated in the previous chapter. The results of computational study have aided in understanding the physics involved in flow-induced vibration and influence of additional wake fields from an upstream body. In this chapter, experimental investigations are carried out to test flutter instability of a plan structure and to identify energy harnessing potential of resultant oscillating motion. Experiments also verify the numerical findings, increase confidence in the numerical study used in simulation, and reinforce the thought of the physics involved in the process. In the present chapter, an experimental examination of flutter analysis of a cantilever plate with and without the wake of an upstream bluff body is discussed. The energy generation from the FIV is discussed separately in the subsequent chapter. Entire experimental investigations are performed in a low speed wind tunnel. First, flutter of a plane structure is thoroughly investigated, and subsequently, the effect of additional wake from the upstream bluff body is explored. Initially, a flat body is used as the upstream body, and then four different shapes are considered in testing.

4.1 Flutter of plane structure

4.1.1 Experimental setup

The experiments are conducted in an open ended type wind tunnel of section size 400 mm × 400 mm, with a maximum wind velocity of up to 25 m/s. To ensure uniform flow condition

and laminar flow at inlet, honeycomb meshes are used before the test section. For measuring flow velocity, hotwire anemometers (*ESF-35-2, Greystone energy system*) and Pitot tubes are placed at the inlet and outlet of the test section. The flow velocity is controlled through a variable frequency drive (*Atsel VFD 3HP*) that gives a least change in velocity of 0.1 m/s.

4.1.2 Plane Structure

For the plane structure, a laminated sheet is selected after a number of trials in the wind tunnel environment. It may be noted that based on the numerical investigations, a proof of concept is learned that indicates the effect of an upstream body on FIV of plate. The numerical study is performed considering a plate of thickness of 1 mm, Elastic constant of 200 GPa, Poisson ratio, ϑ=0.3, and *L/D* ratio of 10 (*L*=50 cm, *D*=5 cm). However, in the actual testing, due to limitations in test facility, a different plane structure was adopted. In pretesting, it is noted that a 50 cm long sheet of thickness 1mm (Elastic constant 200 GPa, and density 7800 kg/m^3) is not perfectly plane and has an inherent uneven surface. When the flow passes over the structure, instability arrives at a very high flow velocity (beyond 20 m/s). During oscillation, the amplitude of vibration is very high such that the structure strikes at the side wall of the (400 mm × 400 mm) test section. Therefore, based on the available size of the test section, a shorter length structure is finalized. Similarly, to test the instability and to verify the conjecture drawn by numerical study about role of bluff body in the arrival of instability, a relatively more flexible structure is considered. Moreover, to ensure the experimental results, entire experiments are repeated for two plane sheets of different dimensions.

Investigations are performed on a plane laminated sheet prepared by sandwiching a paper sheet between two polythene films. These films are bonded through a hot roller laminated machine whose temperature is set at 120℃, and the heat-activated films adhere to the paper sheet. As mentioned, experiments are conducted on two test sheets; in the first testing, a 200 mm long,

295 mm wide, 0.28 mm thick sheet is used, and in the subsequent testing a sheet of 250 mm long, 380 mm wide, and 0.32 mm thick is used.

Figure 4.1 (a-b) shows the schematic diagram and photograph of the laminated sheet attached to metal strips. The sheet is mounted in a conventional flag type orientation; the fixed end is towards the upstream side. The cantilever structure is created by fixing leading edge between two metal strips of a thickness of 1.5 mm. Figure 4.2 shows 3D schematic view of the test section and Figure 3 depicts the wind tunnel setup with other apparatus.

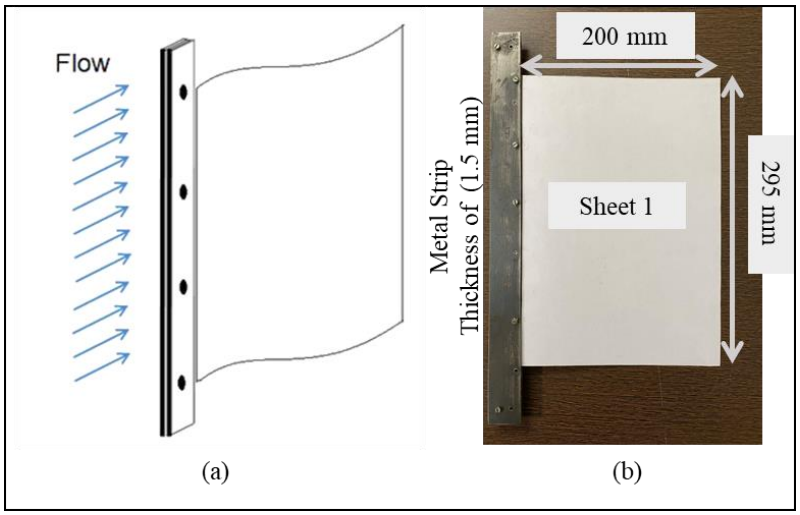

Figure 4.1: (a) Schematic of assembly of a laminated sheet with metal strips, (b) photograph of the laminated sheet

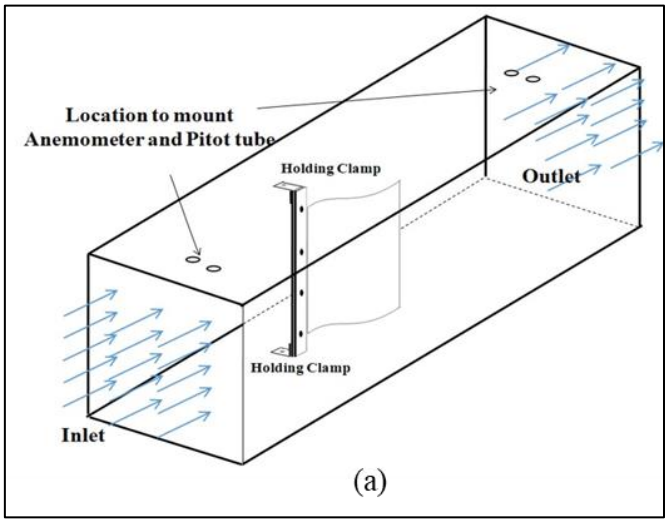

Figure 4.2: 3D schematic view of the test section

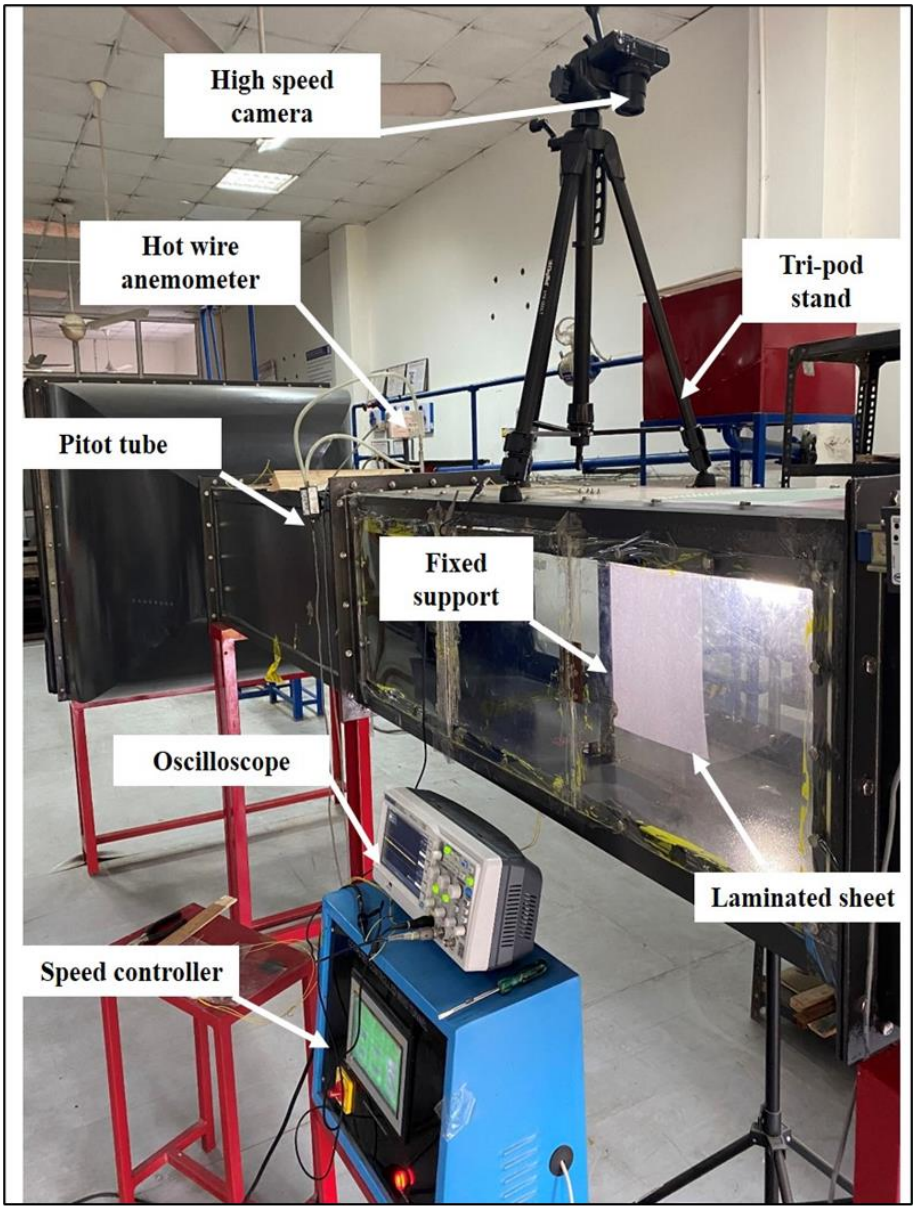

Figure 4.3: The experimental test showing wind tunnel section and other apparatus

4.1.3 Data collection

To visualize oscillation, motion is recorded by a high speed camera (*Sony Rx100m5*) at a high resolution of 1280 × 1024. Oscillations are recorded for 15 seconds at 1000 fps. For illumination, LED lights of 1400 LM luminance are employed. In order to sense the frequency of oscillation, a low cost solution using piezoelectric elements is adopted. A circular shaped piezoelectric element (*Lead Zirconate Titanate-PZT*) is attached at the root of the sheet. The reason of selecting a circular element is its readily availability and high sensitivity. Other

shapes are also utilized for energy harnessing purposes; however, most commonly used piezoelectric elements are of circular shape. Moreover, as the purpose of the element is to sense frequency, circular element is used. Figure 4.4 shows the placement of the piezoelectric element. The 1/3rd area of the circular element is sandwiched between the metal strips, and the remaining portion is left free rather than applying adhesive bonding that may influence the flexibility of sheet. Since the element is not bonded, it will get strain only for the half cycle of the sheet motion, when the sheet oscillates towards the piezo-element side. Therefore, it is expected that the voltage response will be more periodic than harmonic; however, the time history of the voltage response can be used to sense the frequency of oscillation. To verify this fact, a validation study is carried out using rap test of a cantilever metallic beam. The beam oscillations are measured simultaneously by an accelerometer and by a piezoelectric element, and the resultant frequency of oscillation obtained from both the transducers is compared.

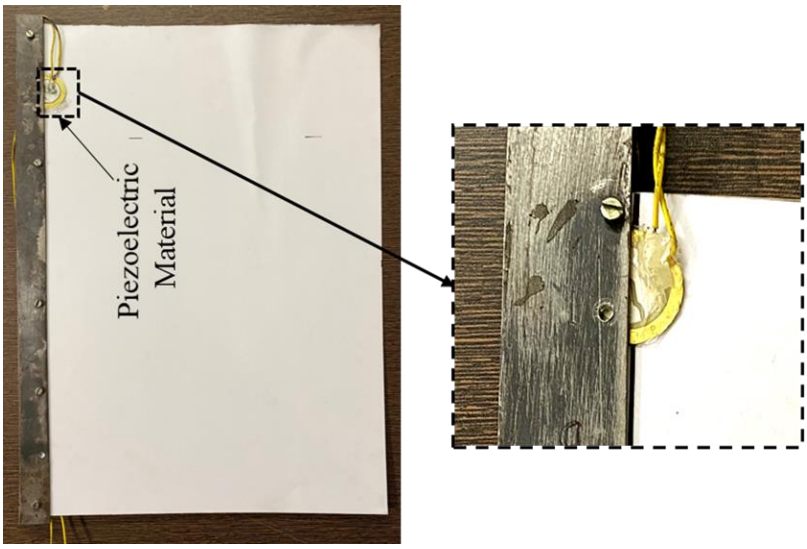

Figure 4.4: The piezoelectric elements and its fitment with the test model

The length, width, and thickness of the metallic beam are 250 mm, 20 mm, and 2 mm, respectively. A piezoelectric element (*PZT type*) and an accelerometer (*B&K 4722*) are mounted on the beam for vibration measurement, as shown in Figure 4.5. The piezo element is partially clamped between the beam and C-clamp. The vibration signal is recorded through a

signal conditioner (charge amplifier) and oscilloscope. Figure 4.6 shows frequency spectrum of samples collected from the rap test. The measured 13 Hz frequency in both the spectrums verifies that a partially clamped piezoelectric element can be used for the measurement of frequency of oscillation of beam. Moreover, in the piezoelectric sample, apart from the dominant frequency of 13 Hz, higher harmonics are also noted, which are presented due to periodicity in the signal recorded.

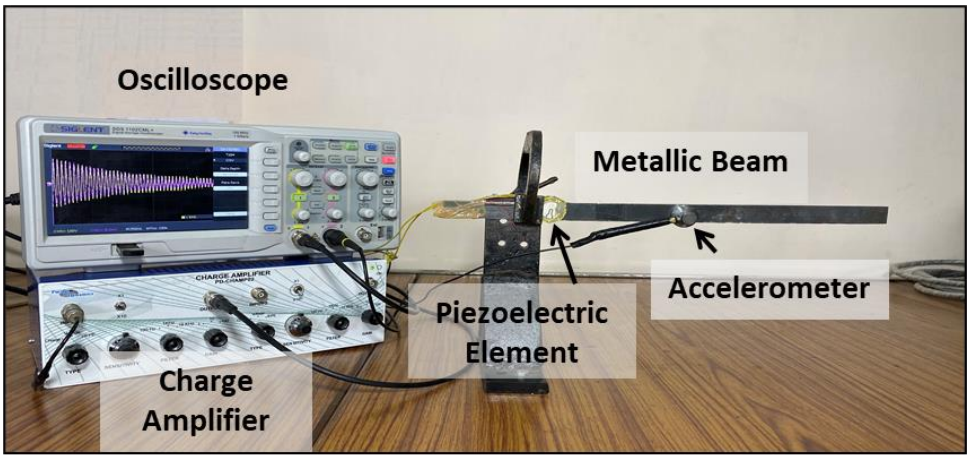

Figure 4.5: Experimental setup to measure the frequency of metallic beam by accelerometer and the piezoelectric element

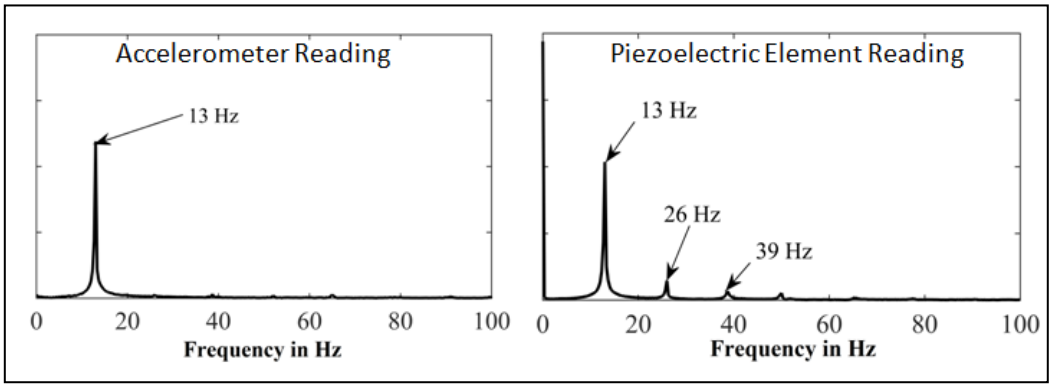

Figure 4.6: Frequency spectrum of the sample measured from accelerometer and piezoelectric element

4.1.4 Estimation of properties of laminated sheet

Since the used laminated sheet is not made of standard material, its mechanical properties are not available in the literature. It may be noted that there are several methods available to find

material property of laminated composite of functionally graded material (FGM); however, the present material is a simple three layer laminated, and for obtaining its property, the experimental approach is adopted [105, 106]. The density *(ρ)* of 1174 kg/m^3 is obtained using mass (by weighing) and volume of a sheet. The elastic constant is determined by using free vibration of a test cantilevered beam made by the sheet material. The following equation is used to find the elastic constant [107].

$$\omega = \frac{2\pi}{T} = (\beta l)^2 \sqrt{\frac{EI}{\rho A l^4}} \tag{4.1}$$

After rearranging equation (4.1)

$$E = \left(\frac{2\pi}{T}\right)^2 \frac{\rho A l^4}{I} \frac{1}{(\beta l)^4} \tag{4.2}$$

Equation (4.1) shows the formula of a beam natural frequency, where *T* represents time period, *E* is the elastic constant, (βl) is a constant depending on boundary condition, and *I* represent second moment of area of the cross section.

For vibration testing, a test strip of size 8 cm × 1.2 cm is cut from the laminated sheet and clamped as a cantilever beam. Figure 4.7 (a) shows the strip fixed on a bracket as cantilevered beam. To measure its bending natural frequency, small displacement is given at the tip of the beam in lateral direction, and its free vibrations are recorded using high speed camera. It is expected that the tip excitation will predominantly force the beam to vibrate in the first bending mode. Figure 4.7 (b) shows the superimposed images of the beam oscillations, which indicate that vibration mode is equivalent to the first bending mode of a cantilever beam. The motion is visualized at a rate of 1000 fps, and the time period of oscillation is measured from a sequence of recorded video images. The measurements are repeated at least five times, and the average time period is considered to remove the errors. Table 4.1 shows the calculated elastic constant by putting the average time period into Equation (4.2).

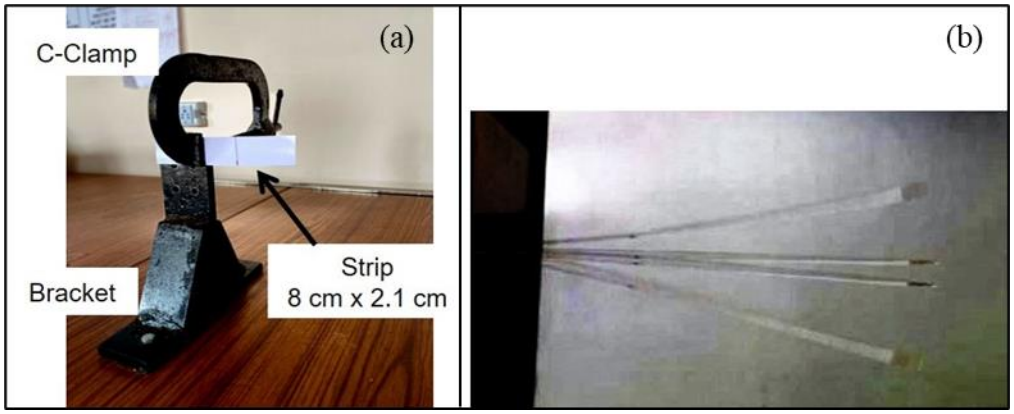

Figure 4.7: (a) The strip fixed on a bracket as cantilevered beam, (b) superimposed image of the beam oscillations

Table 4.1 Material property of the laminated sheet

Density	Elastic constant
1174 kg/m^3	9.51 GPa

4.1.5 Natural Frequency of the sheet

Before performing the wind tunnel testing, bending natural frequency of the sheet used for the testing is calculated using Equation (4.1). In addition to that, to visualize the bending mode shapes of the cantilevered sheet, a finite element model based on the Euler-Bernoulli beam equation is also evaluated [108].

$$EI\,\varphi'''' + \rho A\,\ddot{\varphi} = 0 \tag{4.3}$$

The above Equation (4.3) represents the dynamic motion of a beam of length *L*, where *φ(x,t)* shows transverse displacement of the beam. Assuming a cubic variation of the displacement, the solution can be written as

$$\varphi(x,t) = \sum_{i=1}^{4} N_i(x) q_i\,(t) \tag{4.4}$$

where $q(t) = \begin{Bmatrix} v_1 \\ \theta_1 \\ v_2 \\ \theta_2 \end{Bmatrix}$

In the above Equation (4.4), *N* presents shape function determined using boundary conditions. *v* and θ represent linear displacement and rotation, respectively. Subscripts 1 & 2 indicate beam element boundary as $x=0$ and $x=l$, respectively. By employing the energy approach, stiffness and mass matrices are derived, and an eigen value problem is solved to find out bending modes of the beam.

$$([K]-[M]\omega^2)\{q\}=0 \tag{4.5}$$

where [M] and [K] are mass and stiffness matrices as

$$[M]=\frac{\rho Al}{420}\begin{bmatrix}156 & 22l & 54 & -13l\\ 22l & 4l^2 & 13l & -3l^2\\ 54 & 13l & 156 & -22l\\ -13l & -3l^2 & -22l & 4l^2\end{bmatrix} \qquad [K]=\frac{EI}{l^3}\begin{bmatrix}12 & 6l & -12 & 6l\\ 6l & 4l^2 & -6l & 2l^2\\ -12 & -6l & 12 & -6l\\ 6l & -2l^2 & -6l & 4l^2\end{bmatrix}$$

Using mass and stiffness matrices, a finite element model of a beam is prepared and solved using MATLAB. Table 4.2 illustrates the first three natural frequencies, and Figure 4.8 shows three bending modes.

Table 4.2 Modal frequency of the laminated sheets

Dimension	Ist bending natural frequency (Hz)	IInd bending natural frequency (Hz)	IIIrd bending natural frequency (Hz)
Sheet 1 (20 cm × 29 cm × 0.028 cm)	3.32	20.83	58.34
Sheet 2 (25 cm × 38 cm × 0.032 cm)	2.43	15.24	42.67

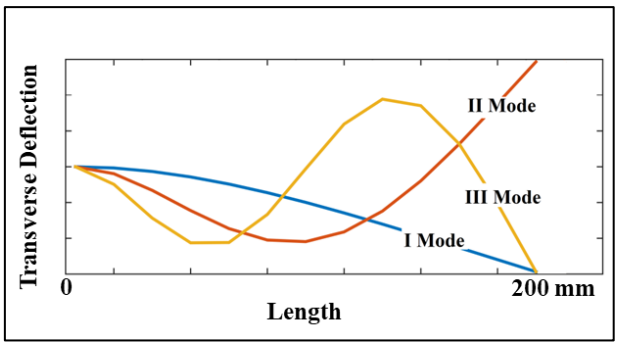

Figure 4.8: Three bending modes of the cantilever sheet

4.2 Vibration response of test sheet I *(length = 20 cm and thickness=0.28 mm)*

The vibration response of the cantilevered sheet is recorded by increasing flow monotonically from 2 m/s to 12 m/s with an incremental change of 0.2 m/s. It is observed that the sheet remains undisturbed until the velocity reaches to 10.2 m/s, shows small movement at 10.4 m/s followed by sudden high amplitude oscillations at 10.6 m/s. Figure 4.9 (a-b) shows time history and frequency spectrum of the measured voltage signal from the piezo-element recorded at a rate of 10k samples/second. The frequency spectrum indicates a dominant frequency of 17.4 Hz and its higher harmonics. The harmonics are expected as the piezo-element is not bonded to the sheet surface and thus showed periodic motion that results in multiple harmonicas in the frequency spectrum. However, the frequency spectrum suffices for the objective of knowing oscillation frequency which has been further verified by the sequence image processing of recorded video. Figure 4.9 (c) depicts that the mode of vibration is predominantly a combination of first and second bending modes of cantilever structure. Besides, the visual observation also confirms minor influence of torsional mode.

When the flow velocity is beyond 10.6 m/s, slight increase in both the frequency and amplitude of oscillation is noted. Moreover, the influence of torsional mode was also found to be increased, which may be due to increased three-dimensionality of the flow in the test section. Figure 4.9 (d-f) shows the time history, frequency spectrum, and superimposed image of sheet vibration recorded at 11.9 m/s flow speed. Figure 4.9 (f) indicates that the mode shape of flapping does not alter significantly from the shape observed at the beginning of flutter (10.6 m/s); however, frequency of oscillation increased to 19.8 Hz. Moreover, the hysteretic behavior of the flutter is noted while the flow velocity is reduced below the critical velocity. Figure 4.10 shows that while velocity increases, flutter arrives at 10.6 m/s flow velocity, and with an increase in the flow velocity, the amplitude increases proportionally; however, while the velocity decreases, the flutter remains till 4.8 m/s velocity.

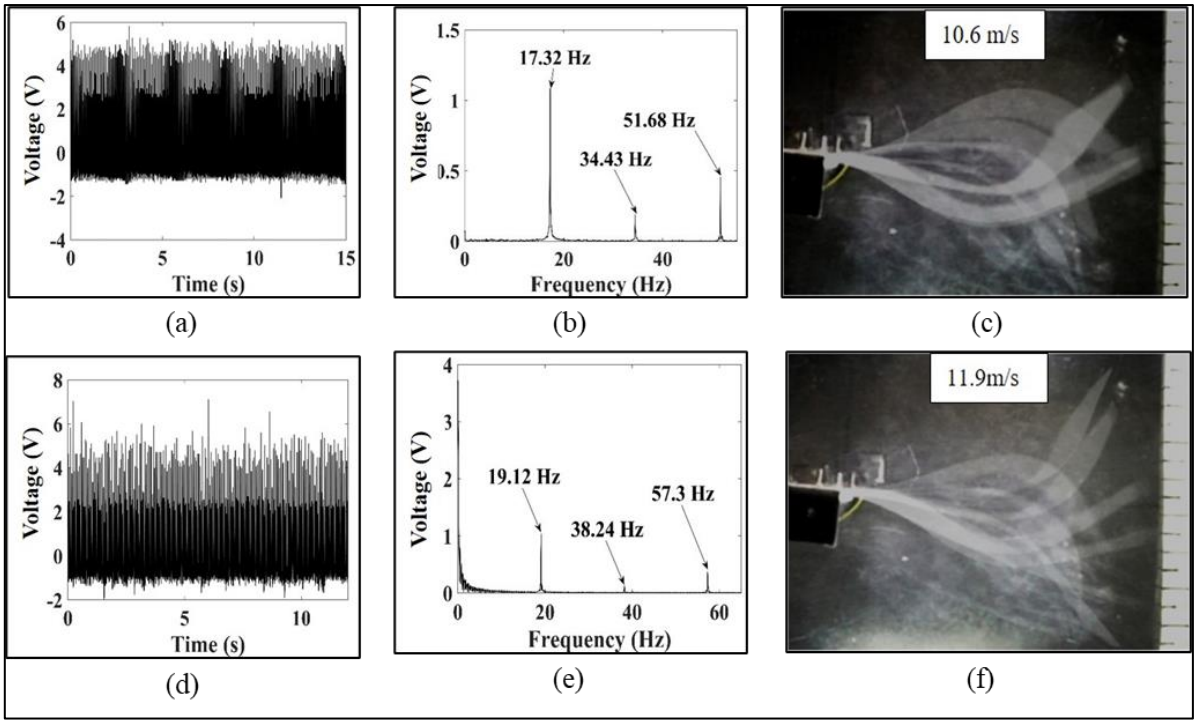

Figure 4.9: Time history, frequency spectrum and superimposed image of vibration (a-c) at 10.6 m/s, (d-f) at 11.9 m/s, respectively

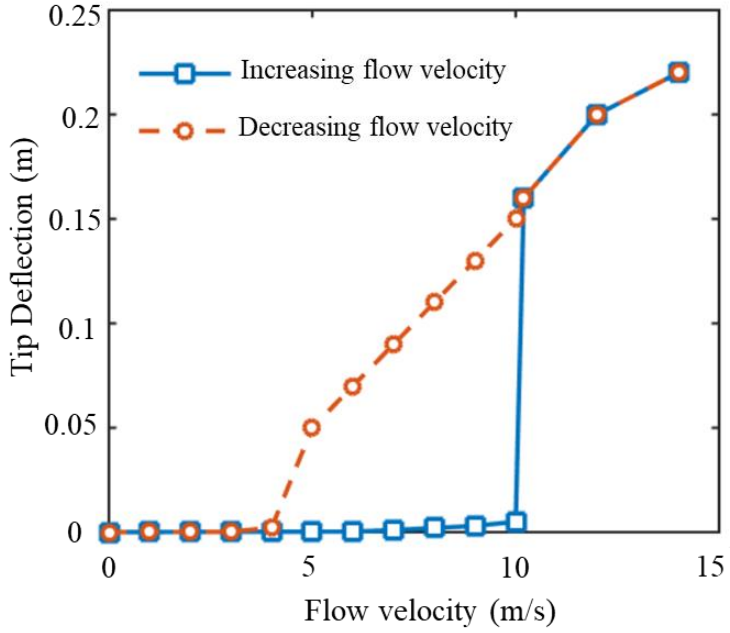

Figure 4.10: A hysteresis behaviour between the increasing and decreasing flow velocity

4.2.1 Analysis of error in measurement

During testing, in order to avoid error in measurement, multiple readings are captured and statistically processed to check uncertainty. In every test, the flow velocity is gradually

increased at a rate of 0.1 m/s per second until the critical velocity has arrived. Then, the system is allowed to reach a steady state before measuring required signals. For every test, minimum of 5 readings are recorded, and the coefficient of variance (COV) is calculated to identify variation in the measured flow velocity and voltage drop. The COV is a common technique to verify the quality of the measured quantities with respect to level of variation in the measurement. It is calculated by taking a ratio of standard deviation (σ) and mean value *(*μ*)* Eq. (4.6-4.7) [109].

$$COV = \frac{Standard\ Deviation}{Mean} \tag{4.6}$$

$$\sigma = \sqrt{\frac{\sum(x_i - \mu)^2}{N}} \tag{4.7}$$

where N is sample size, and x_i is measured value of the experimental reading.

The computed percentage COV value is less than 3% in all the cases (ranging from 1.5%-2.9% in case of velocity), which shows marginal uncertainty in the experimental process, and the measured quantity is acceptable for further processing. Moreover, the outliers in the measured data are ignored, and all analyses are processed considering an average value of five readings of the measured quantity.

4.2.2 Validation of flutter velocity

The results obtained are validated with the standard numerical results obtained in [52], and a marginally acceptable deviation is observed. Table 4.3 shows the validation of experiment results from Manela and Howe [52]. The difference between the theoretical results and the present results is may be due to various reasons e.g., surface is not perfectly plane and uneven density distribution of the laminated sheet, external temperature etc. Manela and Howe investigated the flutter velocity for the clamped-free end condition with dimensionless parameter normalized wind velocity (α) and non-dimensional plate mass (μ) as Eq. (4.8-4.9):

$$\alpha = \frac{U}{U_b} \tag{4.8}$$

$$\mu = \frac{\rho_s}{\rho_0 L} \tag{4.9}$$

Where U is critical velocity of flutter, $U_b = \sqrt{\frac{EI}{\rho_s L^2}}$, E is young's modulus, and I is the moment of inertia per unit length.

Table 4.3 validation of experiment result from numerical results

Dimension	Dimensionless parameter	Experimental Result	Critical velocity (m/s)	Reference Value [52]	Error
Sheet 1 (20 cm × 29 cm × 0.028 cm)	α	9.22	10.6	~10.3	2.9%
	μ	1.46			
Sheet 2 (25 cm × 38 cm × 0.032 cm)	α	11.98	12.6	~11.8	6.7%
	μ	1.34			

4.2.3 Response under the presence of additional wake

After investigating flutter of a plane sheet alone, effect of upstream bluff body (obstacle) is now discussed. It may be noted that in order to acquaint with the initial challenges during performing the experiments and data acquisition and to develop a basic understanding, a simple flat type obstacle is considered as bluff body. In subsequent testing, role of different geometries in arrival of flutter is explored. In addition to this, different *L/D* ratios have been considered for the study. For the sheet of length 200 mm, four sizes of bluff body such as, 15 mm, 20 mm, 25 mm, and 30 mm are also considered.

*I. **Obstacle of size 15 mm***

In the case of a 15 mm bluff body, when the velocity increases up to 8.4 m/s, the sheet remains static, and at 8.6 m/s, noticeable high amplitude vibration is observed. With a further increase in the flow velocity, more violent vibrations are evident. Figure 4.11 (a-c) shows the time

history, frequency spectrum, and superimposed image of sheet vibration recorded at 8.6 m/s flow speed. The mode shape is found equivalent to the shape observed in the previous case.

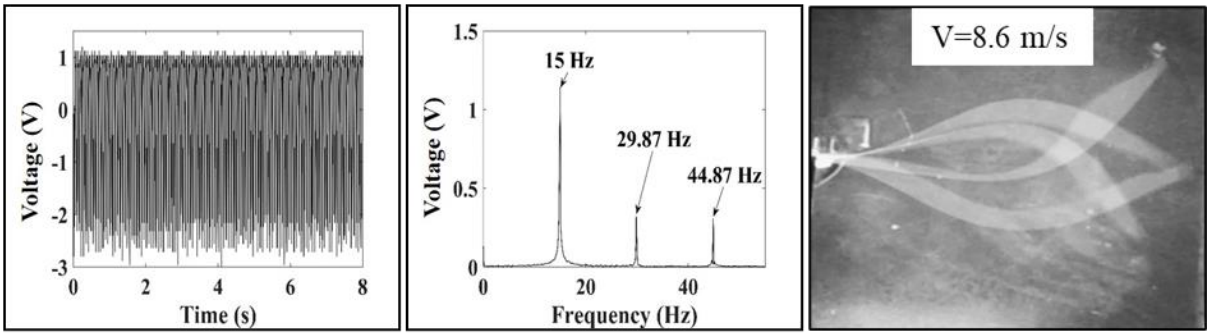

Figure 4.11: (a) Time history, (b) frequency spectrum, and (c) superimposed image of the flexible plate at 8.6 m/s measured with 15 mm bluff body

II. ***Obstacle size 20 mm***

When the flow velocity has increased from 2 m/s to 6.4 m/s, no significant movement of the sheet is observed. However, around 3 m/s velocity, a small level oscillation is observed, which again vanished with increase in flow velocity up to 4.5 m/s. Visual observation indicated an equivalent first bending mode oscillation of the sheet. It may be arisen due to vortex-induced oscillation. When the flow is further increased to 6.6 m/s, noticeable high amplitude vibration is observed. Figure 4.12 (a-b) shows the time history and frequency spectrum of the voltage response. The frequency spectrum shows a dominant frequency component of 14.6 Hz, along with its higher tones, which shows periodicity in the measured signal. The superimposed image indicates a combined first and second bending mode vibration, as shown in Figure 4.12 (c). As the flow velocity increased further up to 8 m/s, the vibration level increased slightly; however, the visual observations have not indicated a noticeable change in the mode shape of the oscillation. Figure 4.12 (d-f) and (g-i) are plotted for 8 m/s and 9.1 m/s velocities, respectively. It can be noticed that in the presence of bluff body, the critical flutter speed reduces as compared to the flutter observed for the case of without bluff body.

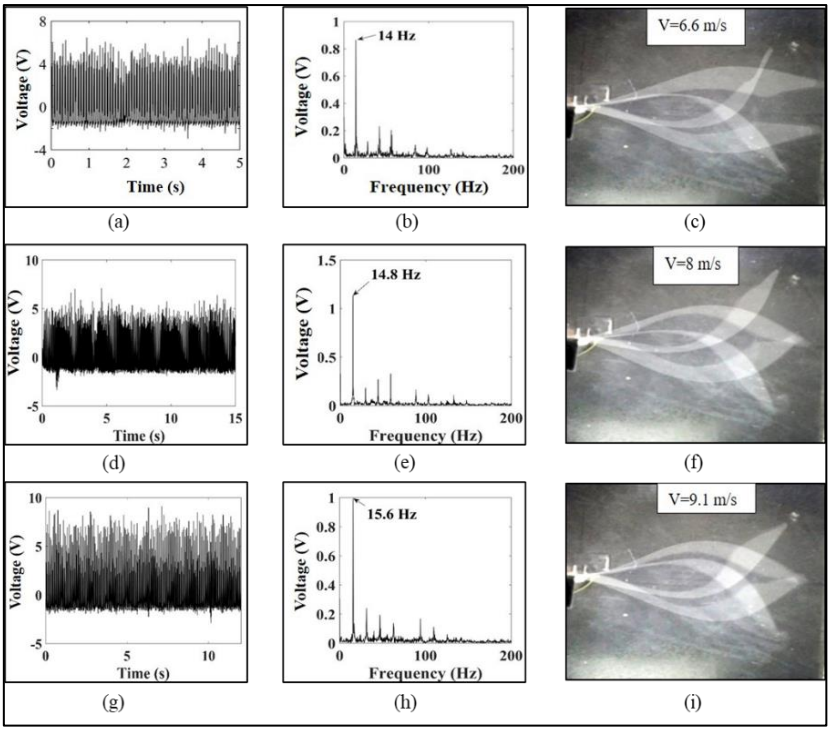

Figure 4.12: Time history, frequency spectrum and superimposed image of vibration measured with 20 mm bluff body (a-c) at 6.6 m/s, (d-f) at 8 m/s, and (g-i) at 9.1 m/s, respectively

III. ***Obstacle size 25 mm***

Now experiments are conducted with a body of 25 mm width. At the flow velocity of 6.1 m/s, the sheet showed intermittent flapping, which is considered the arrival of the flutter instability. When the flow increased further up to 8.5 m/s, the time interval of intermittent oscillation was found slightly changed; however, the intermittent behavior of the oscillation remained the same.

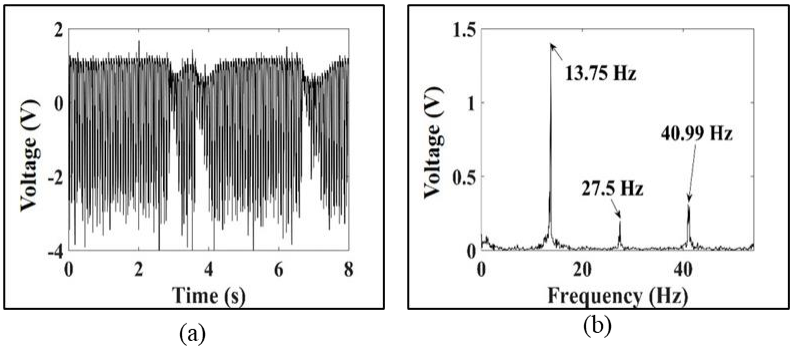

Figure 4.13: (a) Time history and (b) frequency spectrum of the plate vibrating at 6.1 m/s measured with 25 mm flat bluff body

The time history and frequency spectrum of vibration are depicted in Figure 4.13 (a-b). The intermittency can be noticed in the time history at around 3 and 7 seconds. Testing with a 30 mm obstacle showed interesting facts. When the 25 mm body is replaced by 30 mm body, complete suppression of flutter is noted up to 10 m/s flow velocity. The laminated sheet encloses within the shaded shear layer that restricts the reattachment of flow over the sheet and restrains the arrival of flutter. It is expected that reduction in threshold velocity and subsequent disappearance of flutter for larger obstacles is a direct consequence of the size of the wake generated by the bluff body.

4.2.4 Results and discussion

All the results obtained are summarized in Table 4.4. It is clearly observed that the presence of an upstream bluff body has a marked influence on the critical velocity of flutter. For the case of plane sheet, noted critical velocity of flutter is 10.6 m/s, that it reduces by 19% (8.6 m/s) with the introduction of a 15 mm size (L/D =13.33) obstacle. For 20 mm (L/D =10) body, the critical velocity is reduced by 37% (6.6 m/s) and by 42% for the 25 mm (L/D=8) body.

Table 4.4 Summary of results obtained from all the experiments

Size of bluff body (D)	Critical velocity of flutter	Tip displacement (Peak to peak)		Dominant frequency of oscillation
Without bluff body	10.6 m/s	at 10.6 m/s at 11.9 m/s	160 mm 170 mm	17.32 Hz 19.12 Hz
1.5 cm	8.6 m/s	at 8.6 m/s	160 mm	15 Hz
2 cm	6.6 m/s	at 6.6 m/s at 8.0 m/s at 9.1 m/s	160 mm 170 mm 175 mm	14 Hz 14.8 Hz 15.6 Hz
2.5 cm	6.1 m/s (Intermittent flutter)	at 6.1 m/s	160 mm	13.75 Hz
3 cm	6 m/s	Rarely observed		

It may be interpreted that the reduction in critical velocity is related to the effect of circulation zone created in the wake of the obstacle. The shear layers separated from the bluff body form circulation over the trailing sheet, which imposes a fluctuating negative pressure on both the top and bottom sides of the sheet. The magnitude of the pressure fluctuations depends on the size of the circulation zone. A larger obstacle will create widen zone and will apply higher perturbations to the sheet. The effect of circulation zone may be correlated to the instability generated during transverse galloping mechanism [110]. In this state, the sheet is considered to be under mixed excitation as the flow generated instability and the additional wake generated instability which ultimately causes structure to flutter at relatively lower critical velocity.

4.3 Vibration response of test sheet II *(length = 25 cm and thickness=0.032 cm)*

As discussed in the previous testing, a similar procedure is followed for testing with test sheet II. The vibration response is recorded by increasing flow monotonically from 2 m/s to 12 m/s. It is observed that the sheet remains undisturbed until the velocity reaches to 12.2 m/s, showing small movement at 12.4 m/s followed to sudden high amplitude oscillations at 12.6 m/s. Figure 4.14 (a-b) shows superimposed images of the sheet oscillation captured at different time instances and frequency spectrum, which indicates a dominant frequency of 11.88 Hz and its higher harmonics. The harmonics are expected as the piezo-element is not bonded to the sheet surface and thus showed periodic motion that results in multiple harmonicas in the frequency spectrum.

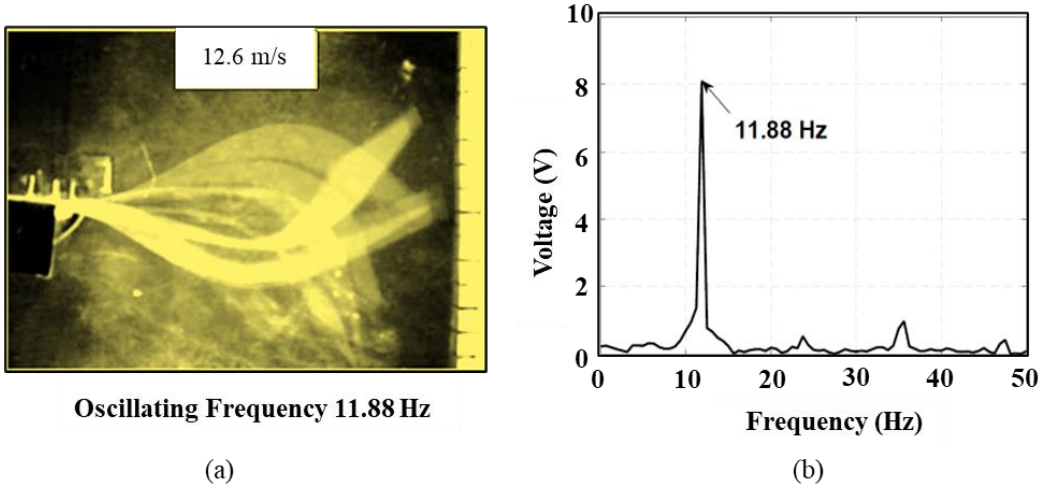

Figure 4.14: (a) Superimposed image of the flexible plate vibrating in the wind tunnel, (b) frequency spectrum of the plate vibration at 12.6 m/s flow velocity

The Figure 14 (a) depicts that the mode of vibration is predominantly a combination of first and second bending modes of cantilever structure. When the flow velocity increases beyond 12.6 m/s, a slight increase in both the frequency and amplitude of oscillation is noted. Moreover, the influence of torsional mode was also found to be increased, which may be due to increased three-dimensionality of the flow in the test section. When the obstacle is introduced in the upstream position, a similar trend of reduction of critical velocity as recorded earlier is observed. Four different sizes as 20 mm, 30 mm, 40 mm, and 50 mm, are considered. In this testing, as an additional study, response at lower velocity region is also analyzed, and a synchronized vortex-induced vibration is observed at lower flow velocity range.

Response at a lower flow velocity

In the case of sheet with 20 mm bluff body, at 1 m/s flow, the sheet vibrates with a tip deflection of 8 mm in a frequency and mode similar to the fundamental mode of a cantilever structure. This amplitude increases to a maximum value of 22 mm at 2.2 m/s and then reduces continuously with velocity till 3.4 m/s; beyond this velocity, up to 8.4 m/s, insignificant flapping is noticed. The findings point out that, in all the cases, the lock-in vibration is presented below 3.5 m/s flow velocity. Figure 4.15 (a-d) depicts the superimposed images of

vortex-induced vibration of 20 mm, 30 mm, 40 mm, and 50 mm flat bluff body, respectively. Among all the cases, 50 mm obstacle shows higher peak amplitude of 60 mm than the other cases of bluff bodies. Figure 4.16 shows the variation of the tip deflection from of plate with the flow velocity. In all the cases, a zone of synchronized VIV is observed; however, it is noted that for smaller body (20 mm), the coupling was weak and intermittent and was continuous and stronger for the larger bluff body (50 mm). Moreover, during the locked-in state, the frequency of oscillation is found to be close to the fundamental natural frequency of a cantilevered structure.

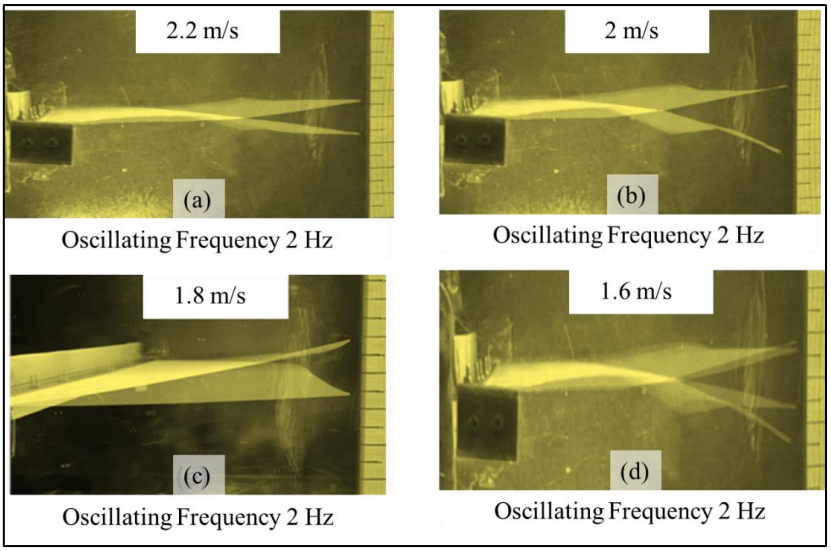

Figure 4.15: Superimposed images of VIV (a) 20 mm, (b) 30 mm, (c) 40 mm, and (d) 50 mm flat bluff body

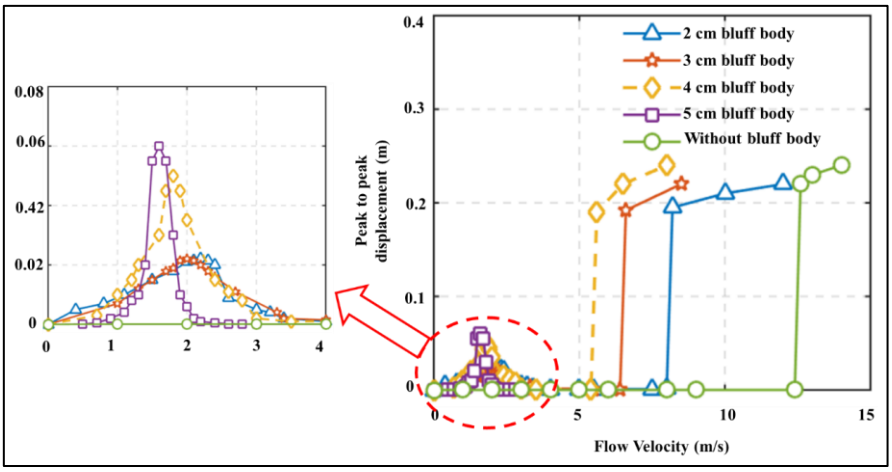

Figure 4.16: Flow velocity *vs* tip deflection (peak to peak) with and without bluff body

Response at a higher flow velocity

Figure 4.17 (a-c) depicts the superposed image of plate motion at the time of arrival of instability and the corresponding frequency spectrum of time history measured by the piezoelectric sensor pasted at the root position. As for the 50 mm obstacle, instability is not observed, and hence response picture is not included in Figure 4.17 (a-c). It is found out that increase in the size of the front obstacle forces sheet to flutter at relatively lower flow velocity; however, beyond a size, early flutter vanishes. Table 4.5 shows the response of the sheet under different conditions.

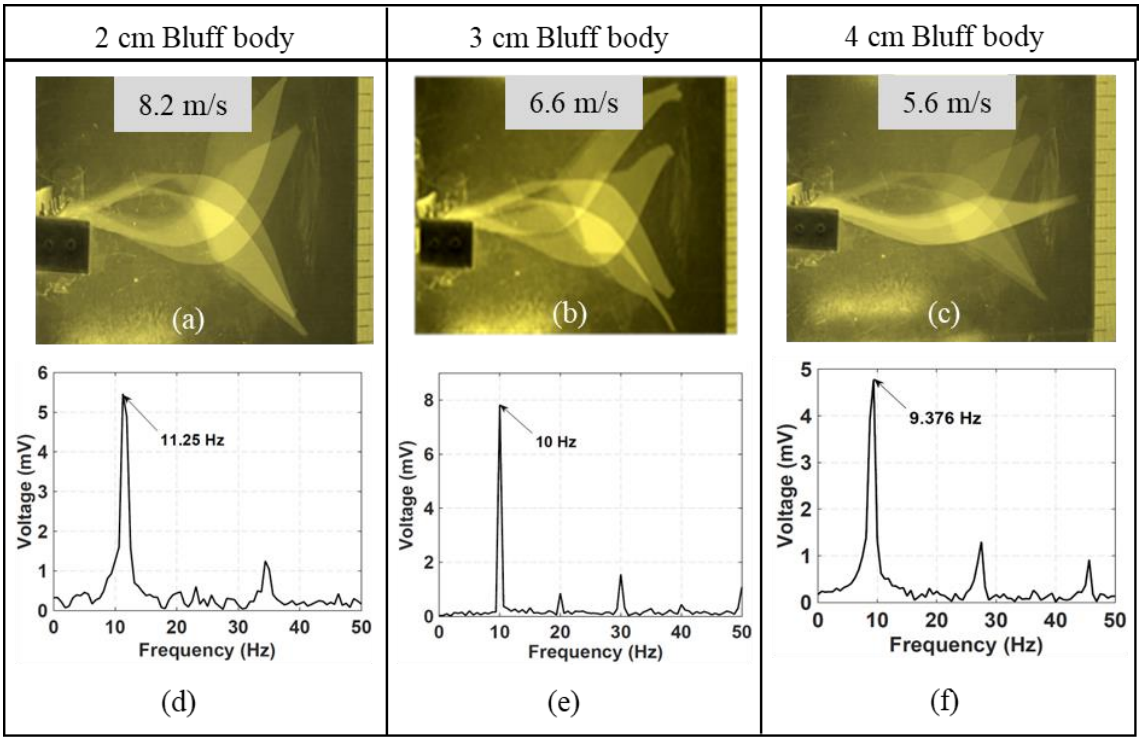

Figure 4.17: Superimposed images of the flexible plate at (a) 8.2 m/s, (b) 6.6 m/s, (c) 5.6 m/s flow speed, and frequency spectrum of the plate vibrating at (d) 8.2 m/s, (e) 6.6 m/s, (f) 5.6 m/s flow speed

Table 4.5 Summary of experimental results

Size of bluff body (*D*) (mm)	VIV			Flutter Instability		
	Velocity (m/s)	Frequency (Hz)	Tip Deflection (peak to peak) (mm)	Critical velocity (m/s)	Frequency (Hz)	Tip Deflection (peak to peak) (mm)
Without bluff body	-	-	-	12.6	11.88	202
20	2.2	2.4	20	8.2	11.25	195
30	2	2.2	22	6.6	10	192
40	1.8	2	50	5.6 (Intermittently)	9.38	190
50	1.6	2	60	Rarely observed		

In the case of 30 mm body, the critical velocity is reduced by 47.26% (6.6 m/s from 12.6 m/s), and for the 40 mm body, intermittent oscillation is observed, and critical velocity is reduced by 55.55% (5.6 m/s). In the case of a 50 mm obstacle, flutter has not been observed which is due to engulfing of the structure by the trailing wake. The laminated sheet encloses within the shaded shear layer that restricts the reattachment of flow over the sheet and restrains the arrival of flutter. It is expected that reduction in threshold velocity and subsequent disappearance of flutter for larger obstacles is a direct consequence of the size of the wake generated by the bluff body.

4.4 Flow-induced vibration of different shapes of bluff body

In the foregoing discussion, testing of vibration of a laminated sheet with a flat type upstream body is explained. As the numerical study (Chapter 3) revealed that different shapes have different resulting modes of vibration and so different strain distribution in the structure, to verify the facts by testing four conventional shapes of frontal bluff body as square, triangle, cylinder, and D-shape are considered for testing. Figure 4.18 (a-d) shows the 3D CAD diagram and Figure 4.18 (e) and Figure 4.18 (f) depict the actual photograph of four bluff bodies and test model of a flexible plate with bluff body and MFC, respectively. Based on the previous

learning, it is found that *L/D* =10 ratio results in a stable limit cycle oscillation, and hence, the same is employed in the present study.

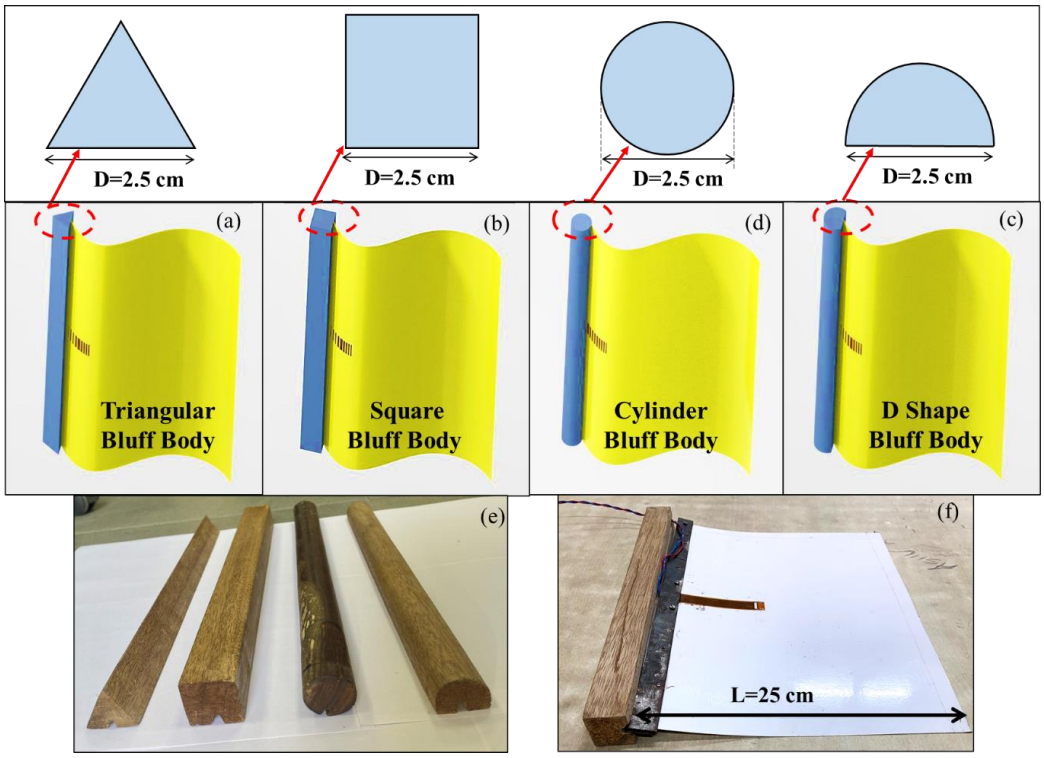

Figure 4.18: (a-d) 3D CAD model of plate with different shapes of bluff body, (e) Different types of bluff body, (f) test model of a flexible plate with bluff body and MFC

4.4.1 Vibration response of the sheet

As a fresh test sheet is prepared for experiments, the process of finding critical velocity of the plane structure is repeated. During test, the flow velocity increases with a 0.1 m/s incremental change, and changes in the motion of the sheet are recorded. Up to a flow velocity of 12 m/s, no significant change in the oscillation is noticed. As soon as the velocity approaches 12.2 m/s, the plate begins to oscillate in an unstable manner with a large amplitude. It may be noted that in the previous testing with the similar sheet of equal dimensions, the flutter arrived at slightly higher velocity of 12.6 m/s small variation in the critical velocity may be due to uneven surface structure of the sheet that occurred during the preparation of sheet under rolling at high temperature. Although it is not directly affecting the objective of the experiments as the results are concluded based on relative changes in the critical velocity. The reduction is measured by

comparing flutter of plane sheet and flutter under the wake flow condition. Figure 4.19 (a) depicts the superimposed image of plate oscillation captured at different time steps. The vibration mode is primarily a mixture of the first and second bending modes of the flexible plate. Figure 4.19 (a1-e1) shows the time history signal measured using the low-cost piezoelectric material and the dominant frequency spectrum, respectively. Furthermore, the effect of torsional mode was observed to be heightened, owing to increasing three-dimensionalities of the flow in the flexible plate.

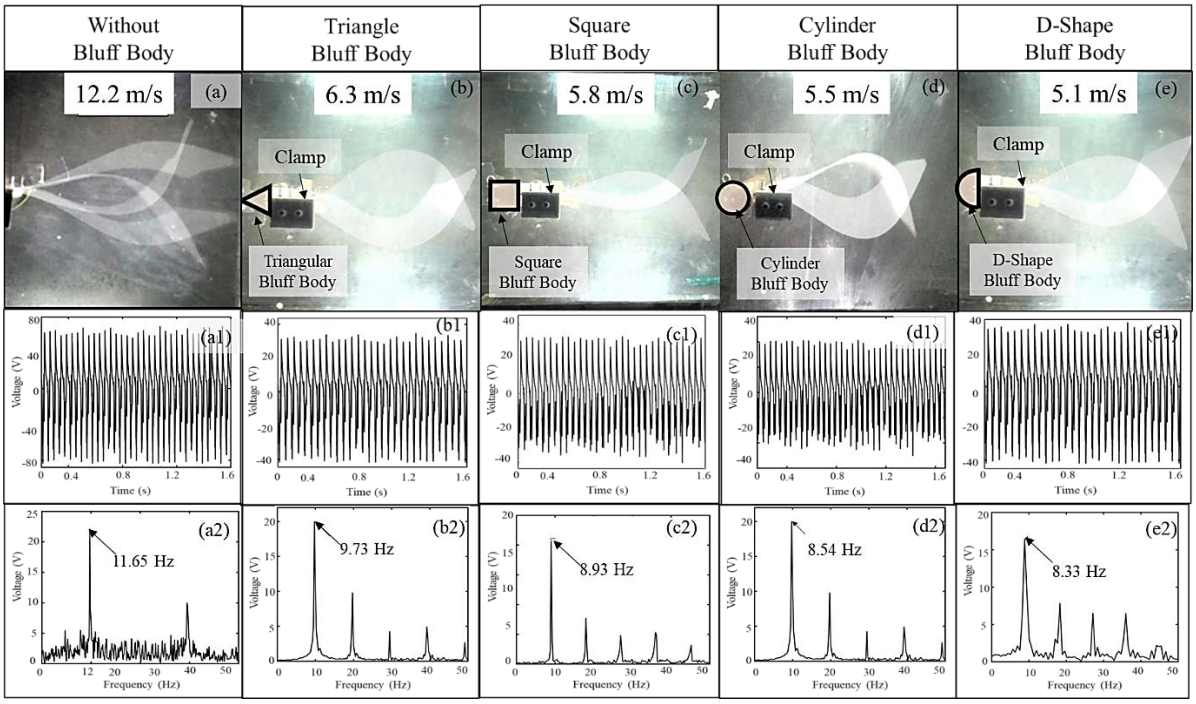

Figure 4.19: (a-e) Superimposed images of vibration, (a1-e1) time domain history, and (a2-e2) frequency spectrum different shapes of bluff body, respectively

In the case of a triangular bluff body, when the flow velocity increases up to 6.2 m/s, the sheet remains static, and after this velocity, intense vibrations appear. Figure 4.19 (b-b2) depicts the superimposed image captured at different time steps, time history, and frequency spectrum of vibration of the sheet for the case of a triangular bluff body. Similarly, in the case of square, cylinder, and D-shape bluff bodies, the flutter is observed at a critical velocity of 5.8 m/s, 5.5 m/s, and 5.1 m/s, respectively. The superimposed images, as shown in figure 4.19 (c, d, and e), indicating a mixed mode bending vibration. Figure 4.19 (c2-e2) shows the frequency spectrum

of the two signals with a dominant frequency of 8.93 Hz, 8.54 Hz, and 8.33 Hz, respectively. Table 4.6 summarizes the results obtained. The presence of higher harmonics in the frequency spectrum is due to periodicity in the measured signal. The spectrum is obtained by applying Fourier's transformation, and the non-harmonic nature of the signal causes higher tones in the frequency spectrum. The measured response also reveals that the sheet exhibits low amplitude vibration at lower flow velocity, which again vanishes with an increase in the flow velocity. This intermittent oscillation can be interpreted as vortex-induced vibration presented for a locked-in range of flow velocity.

Table 4.6 Summary of experimental results

S. No.	Shapes	Critical flow velocity (m/s)	Frequency (Hz)	Tip Deflection (Peak to peak) (mm)
Case 1	Without Bluff Body	12.2	11.65	202
Case 2	Triangular	6.3	9.73	195
Case 3	Square	5.8	8.93	198
Case 4	Cylinder	5.5	8.54	196
Case 5	D-shape	5.1	8.33	197

4.5 Summary

4.5.1 Flat plate bluff body

The flutter instability of the sheet is checked with and without the presence of additional wake flow. Two test sheets of different dimensions are considered, and wind tunnel tests are conducted. A flat bluff body is used to produce a wake field, and effect of different sizes of the obstacle is also analyzed. In both the cases, a similar pattern of flow-induced vibration is observed. The following key points are noted:

- Results obtained from both the test sheets of different lengths and thicknesses indicate a similar trend of arrival of flutter, and impact of presence of an upstream body is noted.

- The upstream body generates vortex flow over the trailing structure that causes flutter at a lower velocity than observed in normal conditions.
- In all the cases with a bluff body, at lower velocity, synchronized (lock-in) vibration is observed that followed to high amplitude flapping at higher velocity. Between the two regimes, the system becomes insensitive to a range of flow velocities. It may be the region between exhibition of VIV and arrival of flutter.
- The impact of size of the bluff body (D) on the critical velocity is not monotonous. The flutter velocity decreases with an increase in the size of the body, but it disappears beyond a certain size of the bluff body.

4.5.2 Different shapes of bluff body

The foregoing study clearly illustrates that the vortex field by a bluff body significantly influences the critical velocity of flutter.

- When the critical velocity is compared with the reference study, it is noted that with a triangular body, it is reduced by 48.36% (6.3 m/s from 12.2 m/s). Similarly for square, cylinder, and D-shape sections, it is reduced by 53.28% (5.7 m/s from 12.2 m/s), 54.9% (5.5 m/s from 12.2 m/s), and 58.2% (5.1 m/s from 12.2 m/s), respectively.
- The output confirms the conjecture reported from the computations. The reason for reduction in the critical velocity may be linked with the additional pressure gradient over the surface of the structure that triggers the instability at early stage. The outcome is further implemented to check the gain in the energy harnessing from the structural oscillations.

The authors would like to highlight an importance aspect about governing mechanism of the instability of sheet. In addition to the flutter, structural galloping is another instability that arises due to presence of circulation bubble [31-35]. From the authors observation, it is appeared to a mixed excitation of circulation and attached flow. Following points may

be important to comment on the governing mechanism of the present vibration,

- In the present experimental study, we have observed that during lower range of flow velocity (up to 2 m/s), the system shows a lock in zone equivalent to VIV or wake galloping and later on a sudden high amplitude vibration at a critical velocity. Numerical simulations suggest that the mechanism responsible for the oscillation of the sheet appears to be a combination of passing circulation over the structure (as observed in structural galloping) and the attached flow (similar to observed in the flutter of plane sheet).
- The analysis of the influence of vortex shedding frequency (f_{vs}) does not show direct correlation of vibration frequency and Strouhal frequency. For example, in the case of 20 mm upstream body (St=0.14 [24,25], 5.8 m/s critical velocity) the frequency f_{vs} is calculated as 32.48 Hz, which is not evident in the frequency spectrum of the vibration (as shown in Figure 4.19 (c2)).
- The visual observation indicates vibration equivalent to phenomenon as flutter under the presence of external wake and so the authors urge to denote the phenomenon as flutter under wake excitation from the upstream object. Manela and Howe [52] have also reported that critical velocity of flutter reduces due to presence of an incoming wake; however, they have not exclusively discussed the governing mechanism of instability.

CHAPTER 5

ENERGY HARVESTING FROM FLOW-INDUCED VIBRATION

In the previous chapters, the dynamics of a plane structure under the influence of flow are explained in detail. As the final objective of the present work is to improve the performance of a flutter-based energy harvester, extraction of energy from the resultant vibration is demonstrated in this chapter. It is worth noting again that flutter has great potential to produce electrical energy using a suitable transduction mechanism, but due to need of high flow velocity available than ambient conditions, its application is so far limited to laboratory testing. While studing dynamics in the previous chapters, it is learned that by adding additional wake disturbances via placing a bluff body in the upstream direction the critical velocity reduces significantly. The same philosophy has been applied now to reduce the input velocity for arrival of instability in the flutter-based harvester, and improvement in the overall performance is demonstrated. In order to measure the improvement in the performance, a comparison is given between energy harnessing from the conventional flutter and the flutter that occurred in the wake field. It has been noticed that different studies have used different transduction mechanisms to extract energy from the oscillating structure under varied flow conditions., i.e., electrostatic, electromagnetic, piezoelectric, triboelectric, etc. Out of a number of means, it has been researched that piezoelectric materials have a simple structure, lower resonance frequency, low cost, good scalability, and hence owning these facts, piezoelectric means have been adopted here for conversion of mechanical energy into electric energy.

5.1 Piezoelectric transduction

Piezoelectricity is defined as the ability of a material to produce an electric charge when subjected to mechanical stress or strain. In the 18th century, this phenomenon was discovered by Pierre and Curie during their study of the effects of pressure on the generation of electrical charge by crystals such as quartz, tourmaline, and Rochelle salt. This piezoelectric effect has been used in various applications, including accelerometers, microphones, ultrasonic transducers etc. Figure 5.1 depicts the schematic working of a piezoelectric material subjected to mechanical stress.

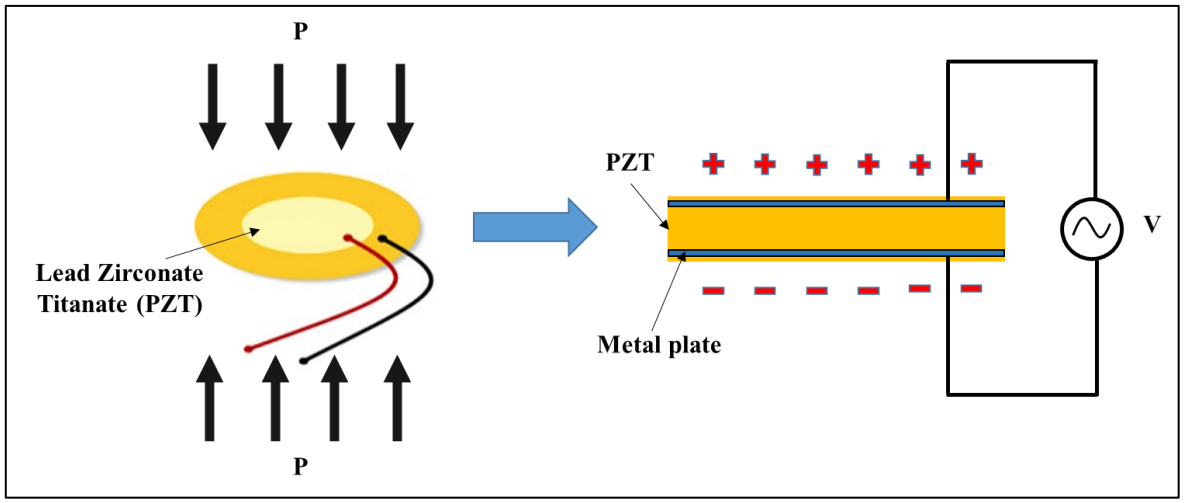

Figure 5.1: Schematic working of a piezoelectric material with generation of electrical charge when mechanical stress applied

Conventionally, in early 1935, potassium dihydrogen phosphate (KDP) and its isomorph were used to show piezoelectric effects. Later, piezoelectricity, barium titanate ($BaTiO_3$) showed extraordinarily high dielectric characteristics and was extensively used. In subsequent time periods, different variety of piezoelectric materials was discovered. Presently, PZT based, MFC, and PVDF are the commonly used piezoelectric material in different sensing and energy harnessing applications.

- *Lead Zirconate Titanate (PZT)*

In the 1950s, it has been found that the PZT (Lead Zirconate Titanate) system showed high piezoelectric properties. Since then, the PZT system with different additions has dominated the piezoelectric ceramic market for a variety of applications [111]. Figure 5.2 depicts the atomic structure of PZT molecule. Although the molecular arrangement of the PZT materials is not balanced, still these materials are electrically neutral. However, when the external force is applied to the PZT, it deforms the structure, causing some of the atoms to move closer or farther away. This throws off the positive-negative balance, resulting in the appearance of net electrical charges. This process is repeated throughout the crystal structure, resulting in net positive and negative charges generated.

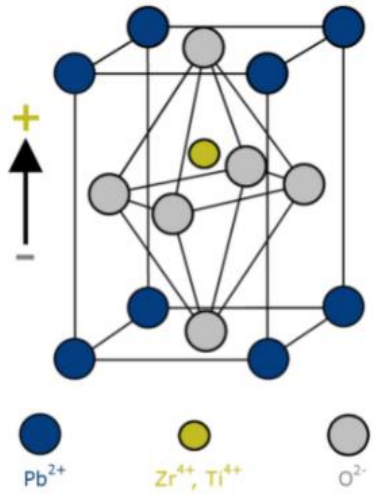

Figure 5.2: The unit cell of PZT material [112]

The PZTs are made in tiny strips of varying sizes and thicknesses, depending on the purpose. However, because of their rigidity, these strips are not suitable for various applications that require flexibility in structure. Due to their brittle nature, they cannot withstand large deformations [113,114]; however, the low cost of the material, sustainability at high frequency, and reasonable charge density make it suitable for

specific energy harnessing applications. Nowadays lead free piezo is also used for energy harnessing purposes [115].

- *Micro Fibre Composite (MFC)*

  To circumvent the restrictions mentioned above, different types of PZT have been created for various purposes that are flexible enough to withstand a high amount of strain. Macro Fibre Composite (MFC) is one such modification of PZT. Figure 5.3 shows layered structure, which consist of rectangular piezoceramic fibers squeezed in between layers of structural epoxy adhesive, polyimide film, and electrodes. The electrodes are connected to the film in an interdigitated pattern on polymide film, allowing the applied voltage to be transferred directly to and from the ribbon shaped rods. This assembly allows for actuation, in-plane poling, and sensing in sealed and ready to use. It can be easily bonded to various types of structures or integrated into a composite structure as a thin, surface conformable sheet (Smart Material Corp. 2012). These MFCs are advanced and very precisely engineering materials with high performance, reliability, and flexbile. However, due to the complexity of production, these sensors and actuators are quite costly.

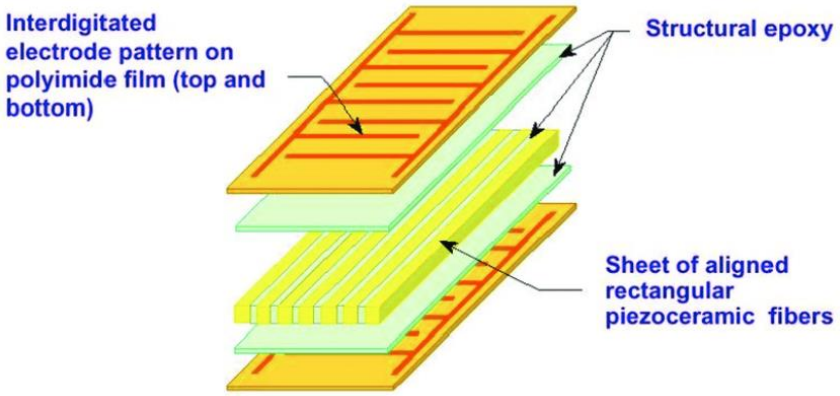

Figure 5.3: Different elements of MFC [116]

- *Poly-vinylidene fluoride (PVDF)*

  It is third type of commonly used material that exhibits high piezoelectricity. PVDFs have now replaced PZTs in various applications due to their affordability, availability, and other piezoelectric properties. PVDFs are more flexible than MFC but less capable of producing high power output.

Another important aspect while extracting energy from a piezoelectric material is the sync of external load with the internal capacitance and resistance. It is noteworthy that the structure undergoes bending oscillation that results in alternate strain in the piezoelectric layer and so alternate current in the external circuit. Since the power is collected across an external resistance (Figure 5.4 (a)), the relative magnitude of the total circuit resistance and capacitance significantly impact the output. According to maximum power transfer theorem [117], when the value of internal resistive load is equivalent to the external resistance, power output becomes maximum. In accordance with it, before final testing of energy harnessing, circuit is calibrated to get the maximum output. Figure 5.4 (b) shows the variation of the output for a range of external resistance.

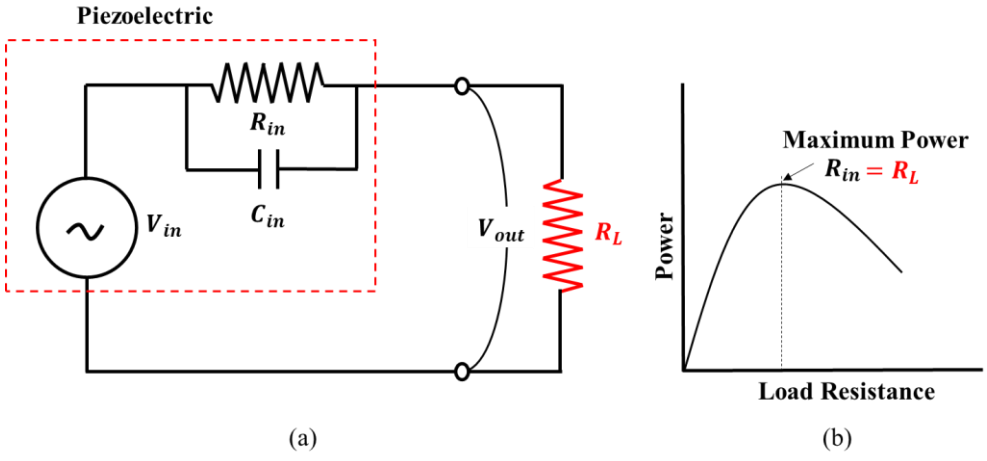

Figure 5.4: Variation of the power output for a range of external resistance

5.2 Flow energy harvesting

The energy harnessing is exercised on a test sheet of 25 cm length and 0.32 mm in thickness. The Micro Fiber Composite (MFC-P2) is used for the piezoelectric transduction. Comparison is made between the energy harvesting from the traditional flutter and the flutter with wake disturbances. The MFC piezoelectric element consists of a layer of piezoelectric fibers embedded in a matrix material, such as epoxy or silicone, and shows high flexibility and high charge density at lower frequency oscillations and therefore employed for energy harvesting. In experimental study, to minimize the impact of the impedance of the connecting cable, copper wire (low impedance) is used. Moreover, since the impedance of the cable is also depended on the length of the wire, short length of the wire is considered (20 cm) to connect piezo element to the data acquisition system. However, it has not been included in the final analysis of the results. The MFC is bonded on the surface of the sheet through adhesive. The position is kept close to the root of the cantilever. Figure 5.5 (a-b) shows the assembly of test sheet with the MFC and placement of bluff body in wind tunnel experiment, respectively, and Table 5.1 shows property of constituents of assembly. In experiments, every test is performed at least five times to reduce measurement error, and the average value is used for post data analysis. As an output parameter, voltage is measured across a load resistance in an external circuit and then processed using equations (5.1) and (5.2) to estimate the power output [118]. The voltage is recorded using the NI 9229 DAQ module.

$$V_{eff} = \frac{V_{pp}}{2\sqrt{2}} \tag{5.1}$$

$$P = \frac{{V_{eff}}^2}{R_L} \tag{5.2}$$

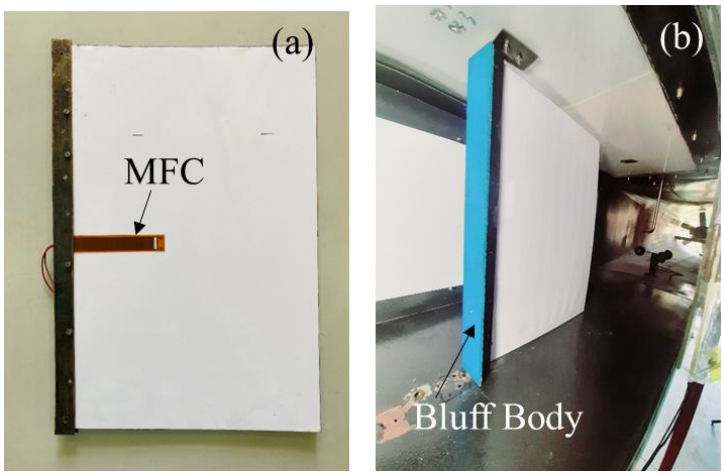

Figure 5.5: Test models (a) sheet along with the MFC piezoelectric elements, (b) placement of bluff body in wind tunnel experiment

Table 5.1 Properties of Plate and MFC materials used in the experiment

Properties	Plate	Piezoelectric
Length L_b, L_p	250 mm	85 mm
Thickness T_b, T_p	1.5 mm	0.3 mm
Width W_b, W_p	50 mm	14 mm
Material	Laminated Sheet	MFC 8514-P2
Mass Density	1174 kg/m^3	5540 kg/m^3
Capacitance C_p	-	25.7 nF
Young's modulus	9.51 GPa	33.336 GPa

5.2.1 Estimation of external load for maximum power output

As output power is greatly affected by the amount of load resistance (R_L), initial testing is done to see the variation in power output with the value of load resistance. The sheet is allowed to oscillate at a flow velocity of 12.6 m/s, and resistance is varied. It is observed that the progression rate of the power first increases with R_L upto 200 KΩ, and then decreases with further increase in R_L. Figure 5.6 shows the variation in power with the load resistance. Owning this fact, energy harvesting tests for different cases are carried out with the 200 KΩ resistance.

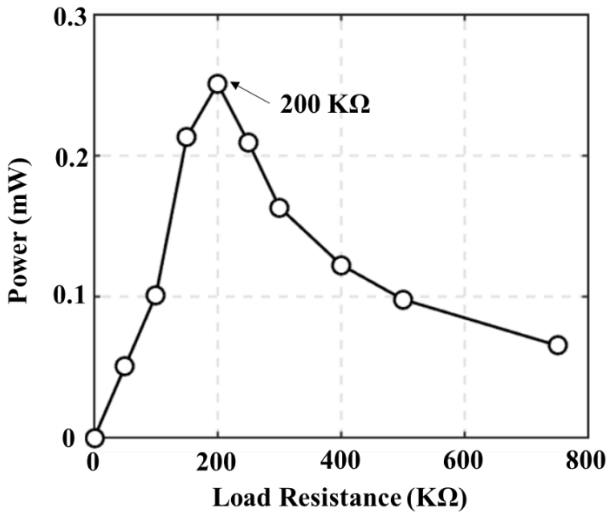

Figure 5.6: Variation of power output with the external load resistance

5.2.2 Measurement of power output

Here, the power measurement corresponding to different sizes of body (20 mm, 30 mm, and 40 mm) is discussed. Figure 5.7 shows the voltage response at the arrival of flutter in different cases. Figure 5.7 (a) shows the reference case of sheet flutter without the presence of a body. In the case of 40 mm bluff body, intermitancy can be noticed in the time history, as shown in Figure 5.7 (d). The voltage output is for the optimum external resistance of 200 KΩ.

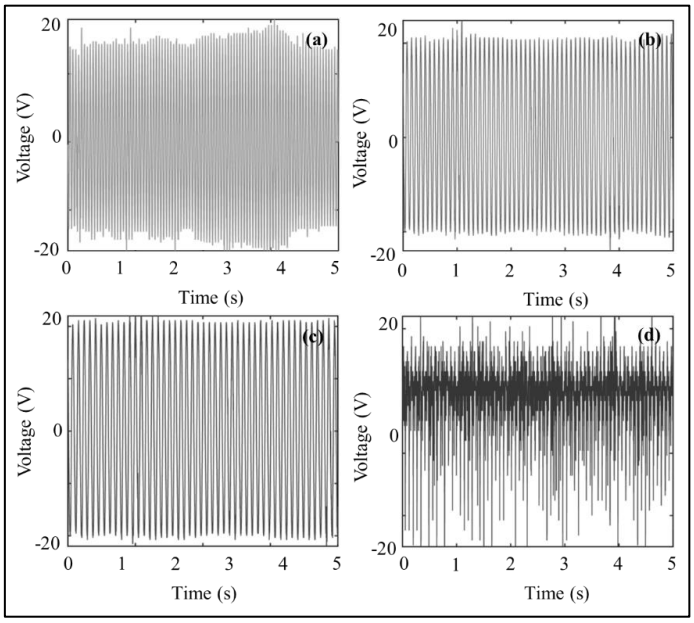

Figure 5.7: Variation of time *vs* voltage (a) without bluff body, (b) 20 mm bluff body, (c) 30 mm bluff body, and (d) 40 mm flat bluff body

Table 5.2 summarizes the flutter velocity for different cases and related power in mW. In addition to this, peak to peak voltage and power at higher velocity is also measured and illustrated in Figure 5.8 (a-b), respectively.

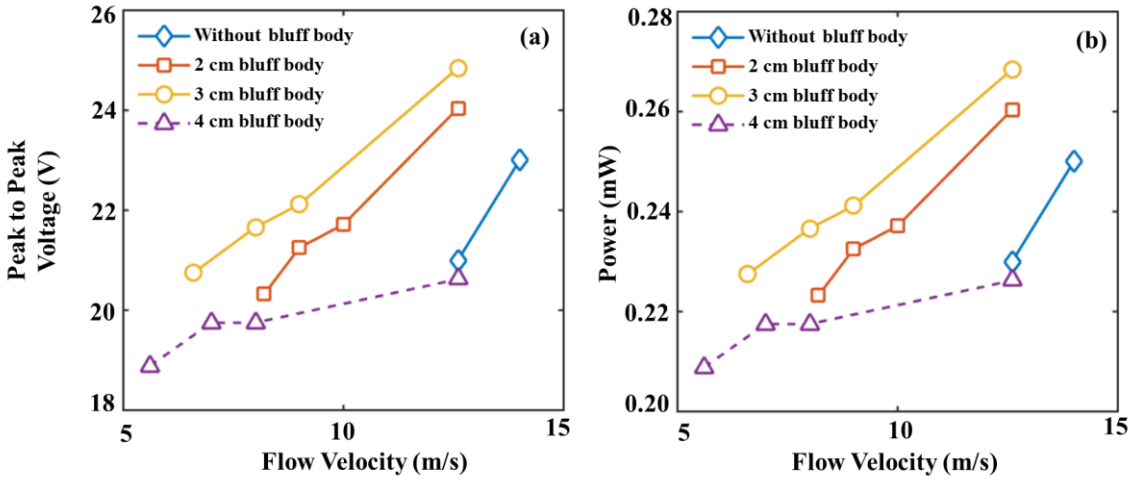

Figure 5.8: (a) Variation in the peak to peak voltage with flow velocity, (b) variation in power output with flow velocity for different sizes of upstream flat body

Table 5.2: Summary of the flutter-based energy harvesting at optimum load resistance

S. No.	Bluff Body	Flutter Velocity (m/s)	Frequency (Hz)	Tip Deflection (mm)	Voltage Peak to peak (V_{pp}) (V)	Optimum load resistance (kΩ)	Maximum Power (mW)	Output to input power ratio (ε)
Case 1	Without Bluff Body	12.6	11.88	202	19.18	200	0.229	2.49×10^{-6}
Case 2	2 cm	8.2	11.25	195	19.42	210	0.224	9.13×10^{-6}
Case 3	3 cm	6.6	10	192	20.04	222	0.228	1.77×10^{-5}
Case 4	4 cm	5.6	9.38	190	19.60	230	0.208	2.74×10^{-5}

It can be pointed out that the output power in all the cases is comparable; however, the input velocity is significantly different and shows a decreasing trend with increasing value. At the critical state, the mode shape of oscillation of the sheet is equivalent in all the cases that generate, and so the output power is also in close proximity; however, the input power is significantly lower for the case of bluff body than the sheet alone. Thus, to clearly understand the improvement in the power output and tangible improvement in the output with reference

case, an efficiency ratio (ε) of output to input power is calculated using following expression.

$$\varepsilon = \frac{P_{out}}{\frac{1}{2}\rho A_{swept} V^3} \tag{5.3}$$

In equation (5.3), the denominator indicates input power, where ρ is the density of the air, V is the critical flutter velocity, H is peak to peak displacement and A_{swept} is constant related to the area swept during the oscillation plotted with the flow velocity. The comparison shows that with reference to simple flutter (Case 1), Case 2, Case 3 and Case 4 yields 3.7, 7.1 and 11 times higher output than the reference case, respectively.

5.2.3 Energy harvesting using different shapes of bluff body

After measuring power for sheet with a flat obstacle, change in output with respect to different shapes of upfront geometry is investigated. A similar configuration of sheet assembly, as used in the previous study, is considered here. The output is measured across the optimum resistance of 200 kΩ. Four different shapes as D-shape, cylinder, square, and triangular bodies are tested and compared with the plane sheet flutter. Figure 5.9 indicates model of four assemblies.

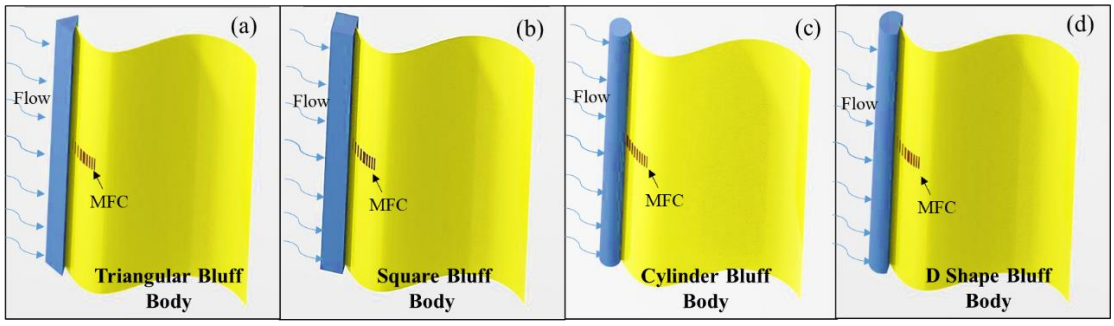

Figure 5.9: 3D model of flexible plate with different shapes of bluff body including MFC

The flutter of the assemblies and corresponding analysis is already explained in the previous chapter (Section 4.2); only power output aspect is discussed here. Figure 5.10 (a-b) shows the output power at different peak to peak voltage and variation of power output *w.r.t.* flow velocity, respectively. Table 5.3 shows different output parameters. It is noted that the D-shape bluff body causes flutter at the lowest velocity at 5.1 m/s.

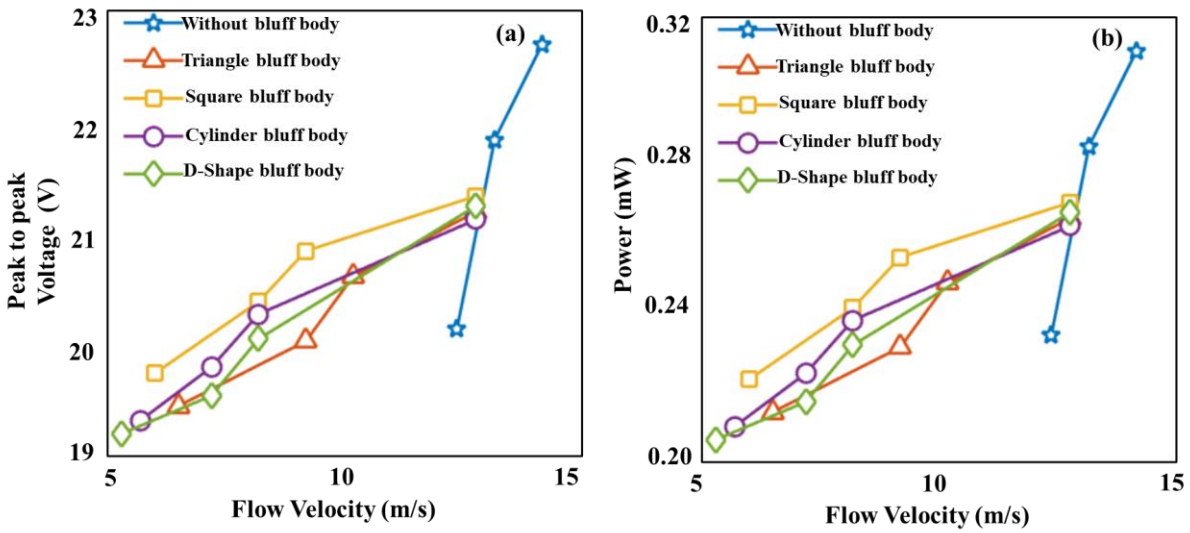

Figure 5.10: (a) Variation in the peak to peak voltage with flow velocity, (b) variation in power output with flow velocity for different shapes of upstream bluff body

Table 5.3 Summary of the flutter-based energy harvesting at optimum load resistance

S. No.	Shapes	Critical Flow velocity (m/s)	Frequency (Hz)	Tip Deflection (Peak to peak) (mm)	Voltage Peak to peak (V_{pp}) (V)	Optimum load resistance (kΩ)	Maximum Power (mW)	Output to input power ratio (ε)
Case 1	Without Bluff Body	12.2	11.65	202	19.2	200	0.231	2.51×10^{-6}
Case 2	Triangular	6.3	9.73	195	19.40	220	0.214	8.9×10^{-6}
Case 3	Square	5.8	8.93	198	19.89	225	0.220	1.71×10^{-5}
Case 4	Cylinder	5.5	8.54	196	20.17	240	0.212	2.55×10^{-5}
Case 5	D-shape	5.1	8.33	197	20.39	250	0.208	3.49×10^{-5}

The optimal load impedance is dependent on the frequency of oscillations. However, it has been observed that the value of the optimum load resistance only varies slightly for small changes in frequency [119]. In the current study, the frequency range encountered is between 9 and 11 Hz, and it was assumed that a single value of optimum resistance will suffice for drawing conclusions from the investigation. However, as suggested, the optimum resistance is evaluated for different cases and corresponding changes are incorporated. The results obtained with new optimum load resistance indicated marginal variation and the conclusions of the study about better performance from a D-shape object remained unchanged.

Flutter has a great potential to capture wind energy in the form of multi-mode oscillations with large amplitude and gained attention as a suitable source of renewable energy to power small electromechanical devices. The greatest challenge in materializing this process is need of higher flow velocity than available in surrounding, which restrains its applicability to the real life environment. Most of the existing studies on flutter-based harvester are limited to laboratory testing. The present research examines energy harnessing potential of flutter of a plane sheet under different flow conditions using different shapes of upstream bluff body (Triangular, square, cylinder, and D-shape). A benchmark study of flutter without additional upstream body is also performed, and a comparison is reported with respect to the arrival of flutter and amount of energy generation in different cases. Following are the key conclusions of the study.

- It is found that in the presence of a flow field generated from the upstream bluff body, the critical velocity reduces significantly, and consequently, the performance of the energy harnessing process improves. Numerical study indicates that the additional pressure distribution over the plane structure is a probable reason of lowering the arrival of flutter.
- With respect to the different geometries of the upstream body, it is noted that the effect of D-shape bluff body on the critical velocity of flutter is highest. When correlating with traditional flutter of the plane sheet, the critical velocity reduced from 12.2 m/s to 5.1 m/s (58.2% reduction), whereas in the cases of cylinder, square, and triangular sections, 54.9%, 52.3%, and 48.4% reduction are recorded, respectively.
- Energy harnessing is realized using MFC material, and with respect to different cases, an output ranging from 0.20 mW to 0.23 mW across an optimum load resistance is observed.

- The relative performance is compared in terms of a ratio of output to input power, and it is noted that triangular, square, cylinder, and D-shape bodies exhibited 3.54, 6.81, 10.16, and 14 times higher output than the benchmark case, respectively.

The aforementioned results indicate that in the presence of the upstream bluff body, the critical velocity reduces significantly, and consequently, the performance of the energy harnessing process improves. Out of the four cases, D-shape bluff body reduces the critical velocity of flutter by 58.2% more than the reference test and subsequently produces a higher output voltage. The power output is compared in terms of a ratio of output to input power, and it is noted that D-shape yields 14 times higher output than the reference case. In the case of triangular, square and cylinder bluff body, critical velocity of flutter reduces by 48.4% and 52.3%, and 54.9%, and corresponding power output is 0.21 mW, 0.22 mW and 0.21 mW, respectively.

As the numerical study (Chapter 3) revealed that different shapes have different resulting modes of flow-induced vibration and so different strain distribution in the structure, to verify the facts by testing four conventional shapes of frontal bluff body as square, triangle, cylinder, and D-shape are considered for testing in Chapter 4. This chapter focuses on corresponding energy harvesting. The results obtained indicate that the shape of the upstream body has significant effect on energy harnessing performance. Due to limitation of computation, low *Re* number condition is considered, and so instead of a qualitative comparison of experimental and numerical results, a quantitative comparison is analyzed. The comparison shows similar trend, i.e., (i) the shape causes variation in vibration characteristics, (ii) the D-shape object produces higher level of vibration and so the higher energy harnessing performance.

CHAPTER 6

CONCLUSIONS AND FUTURE SCOPE OF THE WORK

6.1 Conclusions

Energy generation at a large scale from non-traditional sources such as solar, wind, tidal, and others has been a field of attention for decades. However, there are motivations to identify small renewable sources to power small systems, particularly those mounted at far locations where traditional power supply is either expensive or not feasible. One of the common examples is powering micro sensors mounted in remote locations. It has been observed that flow-induced vibration is one of the appropriate sources to harvest a small amount of energy for small systems and has constantly been researched for years to develop a small scale power generator. Reported literature shows an extensive implementation of galloping and VIV based systems, although the flutter is less explored due to the requirement of a flow velocity higher than the available ambient wind speed. Nevertheless, it is a highly coupled mode of fluid and structure, wherein the structure shows vigorous limit cycle oscillation in combination of different bending modes and hence identified as a potential source to harvest abundant ambient energy. This work proposes a novel solution to improve the performance of a flutter-based energy harvesting by reducing the critical velocity of flutter at the approachable range of flow at ambient conditions. In the present work, both experimental and numerical studies are performed on a test geometry of a flag like structure, and the arrival of flutter under different flow conditions and corresponding energy harnessing performance are analyzed. For variation in the flow condition, wake flow is introduced in the flow using upstream bluff body of

different geometries. The followings are the summary of the work performed and the key conclusions of the respective work:

1. Initially, computational work is performed to visualize the role of an upstream body on the characteristics of the resultant flow-induced vibration of a flexible structure. Two-dimensional computational studies are performed at low Reynolds number flow conditions, and four conventional geometries such as, square section, triangular section, circular and D-section section, are considered to generate wake flow from the upstream location. Outcomes have been recorded in terms of displacement of the oscillating structure, flow pressure, velocity, and vorticity distribution and analyzed by visualizing frequency spectrum plots, pressure, and vorticity contours. Estimation of charge generation from the piezoelectric transduction showed interesting facts. Following are the key findings of the numerical study.
    - Flow over the structure induces periodic motion in the flexible structure.
    - The results indicate that different shapes induce different vibration mode shapes of the plate for a given flow velocity. The square section induced fundamental mode vibration of the plate, whereas, in the case of a D-section, circular section, and triangular section, a mix of fundamental and higher bending modes are noted.
    - Analysis of the flow regime illustrates that the location of reattachment of the shear layers plays a crucial role in the generation of different modes. Pressure loading over the plate, explained by the pressure contours, indicates different distribution that forces the plate to form different deflection shapes. The strain induced in the plate is measured to comment on the aspect of piezoelectric energy harnessing. The calculated strain distribution indicates that the plate with

a square section showed the lowest level of strain (0.000693), and the circular section showed the highest level of strain (0.004031). For comparison among the different cases, cumulative strain with respect to the length of the structure is calculated that has been found highest in the case of D-section (0.001613) bluff body.

- It is observed that, for an equivalent input flow condition in all four cases, the flow distribution over the plate differs in terms of magnitude and nature of pressure on the structure, position of reattachment location of the shear layer, expansion of shear layer in the cross flow direction and induced mode of bending vibration of the structure.

2. After observing the flow-induced vibration of the flexible structure in a low Reynolds number environment, a brief investigation of flow distribution with air as a flow medium is carried out. It is learned that, in the flutter of a plane structure, the flow remains attached to the surface of a flexible structure, and instability is generally triggered by the perturbation originating at the tip region. Hence, owning fact, simulation with air as a medium is performed on a rigid plane structure, and flow distribution with respect to different upstream bodies at different time instances is studied. It is noted that in the case of a triangle and D-shape body, it is an alternative in nature. Although, in the case of a square body, the vorticity pattern is symmetric with respect to top and bottom sides of the plate.
3. A wind tunnel setup is prepared for the experimental study, and numerous tests have been conducted to investigate the flutter of a plane structure and the subsequent effect of additional wake from the upstream bluff body. Experiments are performed on a test model of a flexible laminated sheet. Data is recorded using flow & vibration sensors and a data acquisition system. Initially, a flat body is used as the

upstream body, and then four different shapes (square, triangular, circular, and D-shape) are considered in testing. The study reveals the effect of additional wake disturbances on the plane flutter. The findings showed some fascinating facts regarding the influence of additional wake fields on the critical velocity. Following are the findings of the experiments:

- For a given laminated sheet, when the upstream wake is not added, instability is observed at a flow velocity of 12.6 m/s flow velocity that reduces significantly due to addition of a bluff body. The observation is verified with the reference results, and a good matching is recorded.
- It is demonstrated that a flexible structure in the wake of an upstream bluff body not only exhibits synchronized VIV but also shows flutter, in fact, at reduced flutter boundary observed in the case of conventional plane structure flutter condition.
- The upstream body generates vortex flow over the trailing structure that causes flutter at a lower velocity than observed in normal conditions.
- The impact of wake generated from different sizes of the bluff body (D) indicated a non-monotonous trend. In case of a flat upstream object and a sheet of length 250 mm, flutter velocity decreases up to 55.5% with increase in the size of the body up to 40 mm; however, flutter vanishes when 50 mm size of the bluff body is employed. It is recognized that the extension of the wake from the upstream body engulfs the entire trailing structure, and systematic reattachment of the shed shear layer has not occurred.
- In the case of different shapes of the upstream bluff body (square, triangular, circular, and D-shape), the soul effect of additional wake has remained the same, and the early arrival of flutter is displayed. However, different shapes influence

in a different manner. Among all the four objects, the D-shape upstream bluff body causes flutter at the lowest velocity than the other objects.

4. Flow energy is harvested in terms of the electrical signal using piezoelectric conversion. A piezoelectric element (Micro fiber composite (MFC)) is pasted on the surface of the sheet, and a charge emerges when the sheet gets strained during oscillating motion. The performance of the overall output of energy/power is analysed, and a comparison is made for traditional flutter and flutter in the presence of additional wake from different sizes and shapes of the upstream body.
    - When a flat obstacle is placed upstream, a maximum performance at 6.6 m/s is observed for the case of a 250 mm long sheet and 30 mm upstream body. The amount of output power is comparable with 0.23 mW power generated during plane flutter (benchmark case) at 12.6 m/s flow velocity, although the flow velocity is fairly lower in the previous case. For direct comparison, a ratio of output to input power is calculated, and it is noted that for different sizes such as 20 mm, 30 mm, and 40 mm bluff body exhibits 3.7, 7.1 and 11 times higher output than the benchmark case, respectively.
    - With respect to the different geometries of the upstream body, it is noted that the effect of D-shape bluff body on the critical velocity of flutter is highest when correlating with the traditional flutter of the plane sheet, the critical velocity reduced from 12.2 m/s to 5.1 m/s (58.2% reduction), whereas in the cases of cylinder, square, and triangular sections, 54.9%, 52.3%, and 48.4% reduction are recorded, respectively.
    - The D-shape obstacle showed the highest performance at the lowest flow velocity. The relative performance is compared in terms of a ratio of output to input power, and it is noted that triangular, square, cylinder and D-shape bodies

exhibited 3.54, 6.81, 10.16, and 14 times higher output than the benchmark case, respectively.

The present work is a proof of concept applicable for all kinds of structures that undergoes plane flutter and is beneficial to improve energy harvesting efficiency irrespective of the mode of transduction. The research demonstrated the realization of flutter at ambient conditions and corresponding energy harnessing. It is established that introduction of additional wake disturbance from an upstream object lower downs the critical flutter velocity. It is also reported that equivalent power is generated at 12.6 m/s flow velocity and 6.6 m/s flow velocity by adding an upstream body. The variation in the geometry influences the critical velocity and so the output performance of the harvester.

6.2 Future Scope of the work

Nevertheless, the concept of improving power output from a flutter-based energy harvester is shown successfully; due to limited infrastructure, testing a scaled-up model with highly efficient smart piezoelectric material could not be explored. The real life implementation of the harvester and the physical sensor can be planned. It may be noted that the output is a direct consequence of the quality of the piezoelectric material. A highly efficient and flexible piezoelectric material will yield more electricity.

- A large-scale model can be designed with a different type of transduction, e.g., electromagnetic, electrostatic, piezoelectric, etc. A robust prototype can be planned to check large scall energy generation.

REFERENCES

[1] Païdoussis, M. P., S. J. Price, E. de Langre.: Fluid-structure interactions: cross-flow-induced instabilities. UK: Cambridge University Press. (2011).

[2] Ding, L., Zhang, L., Wu, C., Mao, X., Jiang, D.: Flow induced motion and energy harvesting of bluff bodies with different cross sections. Energy Convers. Manag. 91, 416–426 (2015).

[3] Elahi, H., Eugeni, M., Fune, F., Lampani, L., Mastroddi, F., Romano, G.P., Gaudenzi, P.: Performance evaluation of a piezoelectric energy harvester based on flag-flutter. Micromachines. 11(10), (2020).

[4] Manela, A., Howe, M.S.: The forced motion of a flag. J. Fluid Mech. 635, 439–454 (2009).

[5] Kaneko, S., Nakamura, T., Inada, F., Kato, M., Ishihara, K., Nishihara, T., Mureithi, N.W., Langthje, M.A.: flow-induced vibrations: classifications and lessons from practical experiences: Second Edition. (2013).

[6] Williamson, C.H.K., Roshko, A.: Vortex formation in the wake of an oscillating cylinder. J. Fluids Struct. 2(4), 355–381 (1988).

[7] Govardhan, R., Williamson, C.H.K.: Modes of vortex formation and frequency response of a freely vibrating cylinder. J. Fluid Mech. 420, 85–130 (2000).

[8] Yamamoto, C.T., Meneghini, J.R., Saltara, F., Fregonesi, R.A., Ferrari, J.A.: Numerical simulations of vortex-induced vibration on flexible cylinders. J. Fluids Struct. 19(4), 467–489 (2004).

[9] Sarpkaya, T.: A critical review of the intrinsic nature of vortex-induced vibrations. J. Fluids Struct. 19(4), 389–447 (2004).

[10] Williamson, C.H.K., Govardhan, R.: A brief review of recent results in vortex-induced vibrations. J. Wind Eng. Ind. Aerodyn. 96(6-7), 713–735 (2008).

[11] Shukla, S., Govardhan, R.N., Arakeri, J.H.: Flow over a cylinder with a hinged-splitter plate. J. Fluids Struct. 25(4), 713–720 (2009).

[12] Bearman, P.W.: Circular cylinder wakes and vortex-induced vibrations. J. Fluids Struct. 27(5-6), 648–658 (2011).

[13] Wang, H., Zhai, Q., Zhang, J.: Numerical study of flow-induced vibration of a flexible plate behind a circular cylinder. Ocean Eng. 163, 419–430 (2018).

[14] Turek, S., Hron, J.: Proposal for numerical benchmarking of fluid-structure interaction between an elastic object and laminar incompressible flow. Lect. Notes Comput. Sci.

Eng. 53, 371–385 (2006).

[15] De Nayer, G., Kalmbach, A., Breuer, M., Sicklinger, S., Wüchner, R.: Flow past a cylinder with a flexible splitter plate: A complementary experimental-numerical investigation and a new FSI test case. Comput. Fluids. 99, 18–43 (2014).

[16] Sahu, T.R., Furquan, M., Jaiswal, Y., Mittal, S.: Flow-induced vibration of a circular cylinder with rigid splitter plate. J. Fluids Struct. 89, 244–256 (2019).

[17] Lee, J.: Study of vortex-shedding-induced vibration of a flexible splitter plate behind a cylinder. Physics of Fluids, 25(11): 110811(2012).

[18] Hu, S.L., Lu, C.J., He, Y.S.: Numerical study on vortex induced vibration of a flexible plate behind square cylinder with various flow velocities. J. Shanghai Jiaotong Univ. 19, 488–494 (2014).

[19] Purohit, A., Darpe, A.K., Singh, S.P.: A numerical investigation on effects of structural flexibility on aerodynamic far field sound. Comput. & Fluids. 89, 143–152 (2014).

[20] Zhao, K., Yang, X., Okolo, P.N., Wu, Z., Bennett, G.J.: Use of dual planar jets for the reduction of flow-induced noise. AIP Adv. 7, (2017).

[21] Allen, J.J., Smits A. J.: Energy harvesting eel. J. Fluids Struct. 15, 1–13 (2001).

[22] Taylor, G.W., Burns, J.R., Kammann, S.M., Powers, W.B., Welsh, T.R.: The energy harvesting eel: A small subsurface ocean/river power generator. IEEE J. Ocean. Eng. 26, 539–547 (2001).

[23] Sivadas, V., Wickenheiser, A.M.: A study of several vortex-induced vibration techniques for piezoelectric wind energy harvesting. Act. Passiv. Smart Struct. Integr. Syst. 7977, 79770F (2011).

[24] Sivadas, V., Wickenheiser, A. M.: Small-scale wind energy harvesting from flow-induced vibrations. Smart materials, adaptive structures and intelligent systems. 54716, 737-744 (2011).

[25] Pan, D., Shao, X., Deng, J., Yu, Z.: Simulations of passive oscillation of a flexible plate in the wake of a cylinder by immersed boundary method. Eur. J. Mech. B/Fluids. 46, 17–27 (2014).

[26] Akaydin, H.D., Elvin, N., Andreopoulos, Y.: The performance of a self-excited fluidic energy harvester. Smart Mater. Struct. 21(2), (2012).

[27] Rasani, M.R., Ariffin, A.K., Bashir, M., Wang, J.: Effect of location in a cylinder wake on dynamics of a flexible energy harvesting plate. J. Adv. Res. Fluid Mech. Therm. Sci. 55, 189–198 (2019)

[28] J. P. Den Hartog: The undamped dynamic vibration absorver. Mech. Vib. 82–102 (1934)

[29] Daqaq, M.F., Bibo, A., Akhtar, I., Alhadidi, A.H., Panyam, M., Caldwell, B., Noel, J.: Micropower generation using cross-flow instabilities: a review of the literature and its implications. J. Vib. Acoust. Trans. ASME. 141(3), (2019).

[30] Alonso, G., Meseguer, J., Pérez-Grande, I.: Galloping stability of triangular cross-sectional bodies: A systematic approach. J. Wind Eng. Ind. Aerodyn. 95, 928–940 (2007).

[31] Mahadik, R.R., Sirohi, J.: Harvesting wind energy using a galloping piezoelectric beam. Proc. ASME Conf. Smart Mater. Adapt. Struct. Intell. Syst. 2009, SMASIS2009. 2, 443–450 (2009).

[32] Yang, Y., Zhao, L., Tang, L.: Comparative study of tip cross-sections for efficient galloping energy harvesting. Appl. Phys. Lett. 102(6), (2013).

[33] Zhao, L., Tang, L., Yang, Y.: Comparison of modeling methods and parametric study for a piezoelectric wind energy harvester. Smart Mater. Struct. 22(12), (2013).

[34] Zhao, L., Tang, L., Yang, Y.: Small wind energy harvesting from galloping using. Smart Mater. Adapt. Struct. Intell. Syst. 45103, 919-927 (2012).

[35] Yaghoub, M., Jamalabadi, A.: Effect of Tip Mass Length Ratio on Low Amplitude Galloping Piezoelectric Energy Harvesting. Acoustics, 1(4), 763–793 (2019).

[36] Zhang, L.B., Dai, H.L., Abdelkefi, A., Wang, L.: Experimental investigation of aerodynamic energy harvester with different interference cylinder cross-sections. Energy. 167, 970–981 (2019).

[37] Zhou, C.F., Zou, H.X., Wei, K.X., Liu, J.G.: Enhanced performance of piezoelectric wind energy harvester by a curved plate. Smart Mater. Struct. 28(12), (2019).

[38] Wang, J., Zhou, S., Zhang, Z., Yurchenko, D.: High-performance piezoelectric wind energy harvester with Y-shaped attachments. Energy Convers. Manag. 181, 645–652 (2019).

[39] Liu, F.R., Zhang, W.M., Peng, Z.K., Meng, G.: Fork-shaped bluff body for enhancing the performance of galloping-based wind energy harvester. Energy. 183, 92–105 (2019).

[40] Hu, G., Wang, J., Tang, L.: A comb-like beam based piezoelectric system for galloping energy harvesting. Mech. Syst. Signal Process. 150, 107301 (2021).

[41] Dash, R.C., Maiti, D.K., Singh, B.N.: A finite element model to analyze the dynamic characteristics of galloping based piezoelectric energy harvester. Mech. Adv. Mater. Struct. 1–14 (2021).

[42] Dowell, E.H.: Aeroelasticity of plates and shells., Springer Science and Bussiness Media Vol. 1, (1974).

[43] Taneda, S.: Waving motions of flags. Journal of the Physical Society of Japan, 24(2), 392-401, (1968).

[44] Watanabe, Y., Isogai, K., Suzuki, S., Sugihara, M.: A theoretical study of paper flutter. J. Fluids Struct. 16, 543–560 (2002).

[45] Eloy, C.Ã., Souilliez, C., Schouveiler, L.: Flutter of a rectangular plate. J. Fluids Struct, 23(6), 904–919 (2007).

[46] Huang, L.: Flutter of cantilevered plates in axial flow, J. Fluids Struct. 9(2), 127-147 (1995).

[47] Balint, T.S., Lucey, A.D.: Instability of a cantilevered flexible plate in viscous channel flow. J. Fluids Struct. 20, 893–912 (2005).

[48] Liao, J.C.: A review of fish swimming mechanics and behaviour in altered flows. Philos. Trans. R. Soc. B Biol. Sci. 362, 1973–1993 (2007).

[49] Argentina, M., Mahadevan, L.: Fluid flow-induced flutter of a flag. Proc. Natl. Acad. Sci. U. S. A. 102, 1829–1834 (2005).

[50] Tang, L.: The dynamics of two-dimensional cantilevered flexible plates in axial flow and a new energy-harvesting concept. Thesis (2007).

[51] Shoele, K., Mittal, R.: Flutter instability of a thin flexible plate in a channel. J. Fluid Mech. 786, 29–46 (2015).

[52] Manela, A., Howe, M.S.: On the stability and sound of an unforced flag. J. Sound Vib. 321, 994–1006 (2009).

[53] Watanabe, Y., Suzuki, S., Sugihara, M., Sueoka, Y.: An experimental study of paper flutter. J. Fluids Struct, 16(4), 529-542 (2002).

[54] Patil, M.J.: Limit cycle oscillations of aircraft due to flutter-induced drag. Struct. Dyn. Mater. Conf. 3, 1614–1624 (2002)

[55] Chen, M., Jia, L., Wang, S., Yin, X.: Effects of material damping on flag flutter. Sci. China Technol. Sci. 57, 117–127 (2014).

[56] Virot, E., Amandolese, X., Hémon, P.: Fluttering flags : An experimental study of fluid forces. J. Fluids Struct. 43, 385–401 (2013).

[57] Kumar, D., Arekar, A.N., Poddar, K.: The dynamics of flow-induced flutter of a thin flexible sheet. Phys. Fluids. 33(3), (2021).

[58] Tang, D.M., Yamamoto, H., Dowell, E.H.: Flutter and limit cycle oscillations of two-dimensional panels in three-dimensional axial flow. J. Fluids Struct. 17, 225–242 (2003).

[59] Manela, A., Howe, M.S.: The forced motion of a flag. J. Fluid Mech. 635, 439–454

(2009).

[60] Michelin, S., Smith, S.G.L., Glover, B.J.: Vortex shedding model of a flapping flag. J. Fluid Mech. 617, 1–10 (2008).

[61] Tang, D., Gibbs, S.C., Dowell, E.H.: Nonlinear aeroelastic analysis with inextensible plate theory including correlation with experiment. AIAA J. 53, 1299–1308 (2015).

[62] Connell, B.S.H., Yue, D.K.P.: Flapping dynamics of a flag in a uniform stream. J. Fluid Mech, 581, 33-67, (2007).

[63] Païdoussis, M.P.: Fluid-Structure Interactions: Slender structure and axial flow (Vol. 1), (1998).

[64] Watanabe, Y., Suzuki, S., Sugihara, M., Sueoka, Y.: An experimental study of paper flutter. J. Fluids Struct., 16, 529–542 (2002).

[65] Lin, S.: Flutter of a Cantilevered Plate. HKU Thesis online (2010).

[66] Bryant, M., Garcia, E.: Modeling and testing of a novel aeroelastic flutter energy harvester. J. Vib. Acoust. Trans. ASME. 133(1), (2011).

[67] Bryant, M., Wolff, E., Garcia, E.: Aeroelastic flutter energy harvester design: The sensitivity of the driving instability to system parameters. Smart Mater. Struct. 20(12), (2011).

[68] Hafezi, M., Mirdamadi, H.R.: A novel design for an adaptive aeroelastic energy harvesting system: flutter and power analysis. J. Brazilian Soc. Mech. Sci. Eng. 41, 1–20 (2019).

[69] McCarthy, J.M., Deivasigamani, A., John, S.J., Watkins, S., Coman, F., Petersen, P.: Downstream flow structures of a fluttering piezoelectric energy harvester. Exp. Therm. Fluid Sci. 51, 279–290 (2013).

[70] Liu, J., Zuo, H., Xia, W., Luo, Y., Yao, D., Chen, Y., Wang, K., Li, Q.: Wind energy harvesting using piezoelectric macro fiber composites based on flutter mode. Microelectron. Eng. 231, 111333 (2020).

[71] R. Dickson: New concept in Renewable Energy. LuLu Enterp. (2008).

[72] Abdehvand, M.Z., Roknizadeh, S.A.S., Sedighi, H.M.: Modeling and analysis of a coupled novel nonlinear magnetoelectro-aeroelastic lumped model for a flutter based energy harvesting system. Phys. Scr. 96, (2021).

[73] Yun, G., Oh, D., Kim, Y., Kim, J., Kim, T.: Mechanical feasibility of airfoil shaped energy harvesting device based on aerodynamic instability phenomena. Conf. Inf. Storage Process. Syst. San Fr. California, USA, ASME. 11–12 (2017).

[74] Park, J., Morgenthal, G., Kim, K., Kwon, S.D., Law, K.H.: Power evaluation of flutter-

based electromagnetic energy harvesters using computational fluid dynamics simulations. J. Intell. Mater. Syst. Struct. 25, 1800–1812 (2014).

[75] Olivieri, S., Boccalero, G., Mazzino, A., Boragno, C.: Fluttering energy harvester for autonomous powering: aeroelastic characterisation and preliminary performance evaluation. Procedia Eng. 199, 3474–3479 (2017).

[76] Atrah, A.B., Ab-Rahman, M.S., Salleh, H., Nuawi, M.Z., Nor, M.J.M., Jamaludin, N. Bin: Karman vortex creation using cylinder for flutter energy harvester device. Micromachines. 8(7), (2017).

[77] Chawdhury, S., Morgenthal, G.: Numerical simulations of aeroelastic instabilities to optimize the performance of flutter-based electromagnetic energy harvesters. J. Intell. Mater. Syst. Struct. 29, 479–495 (2018).

[78] Orchini, A., Mazzino, A., Guerrero, J., Festa, R., Boragno, C.: Flapping states of an elastically anchored plate in a uniform flow with applications to energy harvesting by fluid-structure interaction. Phys. Fluids. 25(9), (2013).

[79] Xiao, Q., Zhu, Q.: A review on flow energy harvesters based on flapping foils. J. Fluids Struct. 46, 174–191 (2014).

[80] Zhu, Q.: Energy harvesting by a purely passive flapping foil from shear flows. J. Fluids Struct. 34, 157–169 (2012).

[81] Tang, L., Païdoussis, M.P.: On the instability and the post-critical behaviour of two-dimensional cantilevered flexible plates in axial flow. J. Sound Vib. 305, 97–115 (2007).

[82] Tang, L., Païdoussis, M.P., Jiang, J.: Cantilevered flexible plates in axial flow: energy transfer and the concept of flutter-mill. J. Sound Vib. 326, 263–276 (2009).

[83] Dunnmon, J.A., Stanton, S.C., Mann, B.P., Dowell, E.H.: Power extraction from aeroelastic limit cycle oscillations. J. Fluids Struct. 27, 1182–1198 (2011).

[84] Eugeni, M., Elahi, H., Fune, F., Lampani, L., Mastroddi, F., Romano, G.P., Gaudenzi, P.: Numerical and experimental investigation of piezoelectric energy harvester based on flag-flutter. Aerosp. Sci. Technol. 97, 105634 (2020).

[85] Doaré, O., Michelin, S.: Piezoelectric coupling in energy-harvesting fluttering flexible plates: linear stability analysis and conversion efficiency. J. Fluids Struct. 27, 1357–1375 (2011).

[86] Michelin, S., Doaré, D.: Energy harvesting efficiency of piezoelectric flags in axial flows. J. Fluid Mech. 714, 489–504 (2013).

[87] Zakaria, M.Y., Al-Haik, M.Y., Hajj, M.R.: Experimental analysis of energy harvesting from self-induced flutter of a composite beam. Appl. Phys. Lett. 107(2), (2015).

[88] Hobeck, J.D., Inman, D.J.: Dual cantilever flutter: Experimentally validated lumped parameter modeling and numerical characterization. J. Fluids Struct. 61, 324–338 (2016).

[89] AkaydIn, H.D., Elvin, N., Andreopoulos, Y.: Wake of a cylinder: a paradigm for energy harvesting with piezoelectric materials. Exp. Fluids. 49, 291–304 (2010).

[90] Pobering, S., Ebermeyer, S., Schwesinger, N.: Generation of electrical energy using short piezoelectric cantilevers in flowing media. Act. Passiv. Smart Struct. Integr. Syst. 728807, 109-116 (2009).

[91] Bischur, E., Pobering, S., Menacher, M., Schwesinger, N.: Piezoelectric energy harvester operating in flowing water. Act. Passiv. Smart Struct. Integr. Syst. Vol. 7643, 862-869 (2010).

[92] Xie, J., Yang, J., Hu, H., Hu, Y., Chen, X.: A piezoelectric energy harvester based on flow-induced flexural vibration of a circular cylinder. J. Intell. Mater. Syst. Struct. 23(2), 135–139 (2012).

[93] Song, R., Shan, X., Lv, F., Xie, T.: A study of vortex-induced energy harvesting from water using PZT piezoelectric cantilever with cylindrical extension. Ceram. Int. 41, S768–S773 (2015).

[94] Yan, Z., Wang, L., Hajj, M.R., Yan, Z., Sun, Y., Tan, T.: Energy harvesting from iced-conductor inspired wake galloping. Extrem. Mech. Lett. 35, 100633 (2020).

[95] Zhao, L., Tang, L., Yang, Y.. Synchronized charge extraction in galloping piezoelectric energy harvesting. J. Intell. Mater. Syst. Struct., 27(4), 453-468 (2016).

[96] Binyet, E., Huang, C.Y., Chang, J.Y.: Polymeric flexible plate in the wake of a bluff body for energy harvesting. Procedia Eng. 199, 1296–1301 (2017).

[97] Jia, J., Shan, X., Upadrashta, D., Xie, T., Yang, Y., Song, R.: An asymmetric bending-torsional piezoelectric energy harvester at low wind speed. Energy. 198, 117287 (2020).

[98] Yu, Y., Liu, Y.: Flapping dynamics of a piezoelectric membrane behind a circular cylinder. J. Fluids Struct. 55, 347–363 (2015).

[99] Tian, H., Shan, X., Cao, H., Xie, T.: Enhanced performance of airfoil-based piezoaeroelastic energy harvester: numerical simulation and experimental verification. Mech. Syst. Signal Process. 162, 108065 (2022).

[100] Anderson, J. D.: Computational fluid dynamics: the basics with applications. McGraw Hill, New York, Mechanical Engineering Series (1995).

[101] ANSYS CFX-Solver modeling guide, Release 15.0, 15317 (November), 724–746.

[102] Moaveni, S.: Finite element analysis theory and application with ANSYS, 3/e. Pearson

Education India, (2011).

[103] Tian, X., Liu, J., Lin, J., Li, S., Wang, Z., Hou, J., Zhang, S., Yang, Z., Zhu, J.: Study of the effect of the segmentation method on the power generation performance of rectangular piezoelectric energy harvester. J. of Sens, vol. 2022, 1-7 (2022).

[104] Obeid, S., Jha, R., & Ahmadi, G.. RANS simulations of aerodynamic performance of NACA 0015 flapped airfoil. Fluids, 2(1), 2 (2017).

[105] Sharma, K., Shukla, M.: Experimental study of mechanical properties of multiscale carbon fiber-epoxy-CNT composites. Advance Material Research, 383, 2723–2727 (2012).

[106] Das, P., Singh, I. V., Jayaganthan, R.: An experimental evaluation of material properties and fracture simulation of cryorolled 7075 Al alloy. Journal of materials engineering and performance, 21(7), 1167-1181 (2012).

[107] Mohanty, A. R. Machinery condition monitoring: principles and practices. CRC Press (2014).

[108] Rao, S. S., Yap, F. F. Mechanical vibrations, New York, Addison-wesley, Vol. 4, pp. 75-848, (1995).

[109] Lewis-Beck, Michael S; Bryman, Alan; Futing Liao, T.: The sage encyclopedia of social science research methods. Sage 2, 387–392 (2004).

[110] Nabavi, S., Zhang, L. Portable wind energy harvesters for low-power applications: a survey. Sensors, 16(7), 1101 (2016).

[111] Zhu, X. Piezoelectric ceramic materials: processing, properties, characterization, and applications (pp. 1-34). Nova Science Publishers (2010).

[112] Eddy, B.: PZT – the most commonly used piezoelectric material. https://www.betase.nl/advancedceramics/pzt-the-most-commonly-used-piezoelectric-material/?lang=en, (accessed on 22/03/2021).

[113] Mishra, R., Burela, R., Pathak, H.: A state-of-the art review on fracture analysis of piezoelectric materials. Proceedings of 61st Congress of ISTAM, VITU - Vellore, India, Dec. 11-14, (2016).

[114] Jena, J., Singh, S.K., Gaur, V., Singh, I. V., Natarajan, S.: A new framework based on XFEM for cracked semipermeable piezoelectric material. Eng. Fract. Mech. 253, 107874 (2021).

[115] Kumar, A., Sharma, A., Kumar, R., Vaish, R., Chauhan, V.S.: Finite element analysis of vibration energy harvesting using lead-free piezoelectric materials: a comparative study. J. Asian Ceram. Soc. 2, 138–143 (2014).

[116] Daue, Th. P., Kunzmann J., Na.G.: Macro fiber composite as low cost strain and vibration sensor.
https://www.smart-material.com/media/Presentations/MFC-strain-sensor-ISPA-2009 (accessed on 05/08/2021).

[117] Bhalla, S., Moharana, S., Talakokula, V., Kaur, N.: Piezoelectric materials: applications in SHM, energy harvesting and biomechanics. Chichester, UK: Wiley (2017).

[118] Irwin, J. David: Basic engineering circuit analysis., John Wiley Sons. 7, (2020).

[119] Priya, S.: Modeling of electric energy harvesting using piezoelectric windmill. Applied physics letters, 87(18), 184101 (2005).

LIST OF PUBLICATIONS

SCI Journals:

1. **Agarwal Ankit**, Purohit Ashish. "Study of vibration modes and strain distribution of a flow energy harvester in the wake region of different bluff bodies". *Proceedings of the Institution of Mechanical Engineers, Part C: Journal of Mechanical Engineering Science (2021).*

   Status: ***Online Published***
   Publisher: Sage
   Impact factor: 1.758.

2. **Agarwal Ankit**, Purohit Ashish "On the performance improvement of a flutter based energy harvester by introducing additional wake field". *Energy Sources, Part A: Recovery, Utilization and Environmental Effects (2021).*

   Status: ***Online Published***
   Publisher: Taylor and Francis
   Impact factor: 2.902.

3. **Agarwal Ankit**, Purohit Ashish. "Performance evaluation of Flutter-based energy harvester under different vortex flow regimes: An experimental study". *Arabian Journal for Science and Engineering (2022).*

   Status: ***Online Published***
   Publisher: Springer
   Impact factor: 2.807.

4. **Agarwal Ankit**, Purohit Ashish "Analysis of the impact of vortex disturbance on the flutter instability of a plane structure of an energy harvesting mechanism". *Journal of Vibration Engineering and Technology.*

   Status: ***Under Review***
   Publisher: Springer
   Impact factor: 2.333

International Conference:

1. **Agarwal Ankit**, Purohit Ashish "Effect of bluff body on the performance of flutter based energy harvester" *Proceedings of the XVI Vibration Engineering & Technology of Machinery Conference VETOMAC 2021.*